COMENIUS UNIVERSITY IN BRATISLAVA
FACULTY OF MATHEMATICS, PHYSICS AND INFORMATICS
DEPARTMENT OF APPLIED MATHEMATICS AND STATISTICS

Phase change and flow in multiphase systems

Dissertation thesis

2020

Mgr. Martin Chudjak

Univerzita Komenského v Bratislave
Fakulta matematiky, fyziky a informatiky
Katedra aplikovanej matematiky a štatistiky

Fázová premena a prúdenie vo viacfázových systémoch

Dizertačná práca

Študijný program:	Aplikovaná matematika
Študijný odbor:	1114 Aplikovaná matematika
Školiace pracovisko:	Katedra aplikovanej matematiky a štatistiky
Vedúci práce:	doc. Mgr. Peter Guba, PhD.

2020

Mgr. Martin Chudjak

34517323

Comenius University in Bratislava
Faculty of Mathematics, Physics and Informatics

THESIS ASSIGNMENT

Name and Surname: Mgr. Martin Chudjak
Study programme: Applied Mathematics (Single degree study, Ph.D. III. deg., full time form)
Field of Study: Mathematics
Type of Thesis: Dissertation thesis
Language of Thesis: English
Secondary language: Slovak

Title: Phase change and flow in multiphase systems

Annotation: The thesis consists of three parts: (i) Performing laboratory experiments on Taylor bubbles in downward pipe flow and reconstruction of the shape of bubbles, (ii) modelling diffusion-driven solidification of alloys with a sharp solid/liquid interface and (iii) modelling solidification of supercooled fluids in a finite domain. In the first part we report on laboratory experiments on Taylor bubbles rising in a vertical pipe against the downward fluid flow and the subsequent reconstruction of the shape of the bubbles using laser technique. The second part involves the solution of convection-diffusion equations governing the solidification and the phase-change flow of a ternary melt. The third part is focused on the solidification of an undercooled melt in a finite domain. Heat transport is governed by the diffusion equations and the model also contains kinetic disequilibrium effects.

Tutor: doc. RNDr. Peter Guba, PhD.
Department: FMFI.KAMŠ - Department of Applied Mathematics and Statistics
Head of department: prof. RNDr. Marek Fila, DrSc.

Assigned: 27.01.2016

Approved: 11.04.2016 prof. RNDr. Daniel Ševčovič, DrSc.
Guarantor of Study Programme

....
Student Tutor

34517323

Univerzita Komenského v Bratislave
Fakulta matematiky, fyziky a informatiky

ZADANIE ZÁVEREČNEJ PRÁCE

Meno a priezvisko študenta: Mgr. Martin Chudjak
Študijný program: aplikovaná matematika (Jednoodborové štúdium, doktorandské III. st., denná forma)
Študijný odbor: matematika
Typ záverečnej práce: dizertačná
Jazyk záverečnej práce: anglický
Sekundárny jazyk: slovenský

Názov: Phase change and flow in multiphase systems
Fázová premena a prúdenie vo viacfázových systémoch

Anotácia: V dizertačnej práci sa venujeme trom nasledujúcim problémom: (i) prevedenie laboratórnych experimentov s Taylorovými bublinami a analýza experimentálnych výsledkov s cieľom rekonštrukcie tvaru asymetrických podlhovastých bublín, (ii) modelovanie tuhnutia trojzložkového systému z pevného rozhrania v polonekonečnej oblasti a (iii) modelovanie tuhnutia jednozložkového systému tuhnúceho z podchladenej kvapaliny v konečnej oblasti. V prvom probléme sa pomocou laseru skúma tvar podlhovastej asymetrickej bubliny stúpajúcej vo vertikálnej trubici za prítomnosti toku kvapaliny smerujúceho nadol. Druhý problém zahŕňa riešenie konvektívno-difúznych rovníc popisujúcich tuhnutie ternárnej zmesi a tok, ktorý vzniká v dôsledku fázovej premeny. Tretí problém sa venuje riešeniu tuhnutia podchladenej zmesi v konečnej oblasti, pričom transport tepla je riadený difúznymi rovnicami a model zahŕňa kinetické nerovnovážne efekty.

Školiteľ: doc. RNDr. Peter Guba, PhD.
Katedra: FMFI.KAMŠ - Katedra aplikovanej matematiky a štatistiky
Vedúci katedry: prof. RNDr. Marek Fila, DrSc.

Spôsob sprístupnenia elektronickej verzie práce:
bez obmedzenia

Dátum zadania: 27.01.2016

Dátum schválenia: 11.04.2016

prof. RNDr. Daniel Ševčovič, DrSc.
garant študijného programu

....
študent

....
školiteľ

I would like to thank my supervisor doc. Mgr. Peter Guba PhD., for the help he has provided during the work on this dissertation. I am also grateful to my family and friends for the support and patience they showed during my PhD. study.

Abstract

This thesis consists of three parts. In the first part, we report on laboratory experiments on Taylor bubbles in downward pipe flow and subsequent reconstruction of a three dimensional shape of bubbles. The pipe is enlightened by a laser sheet perpendicular to the vertical pipe axis. The bubble crossing the laser sheet is filmed by a high-speed camera. Our laser measurements reveal that the bubble shapes in the horizontal plane perpendicular to the pipe axis are not concave, but exhibit a depression in their centres. Unlike the velocity of asymmetric bubbles, we find that the shape of the bubbles projected onto the axial plane depends on a mean velocity of the downward flow, with asymmetric bubbles becoming more tapered at larger flow rates. We address a simple inviscid model to explain this dependence.

In the second part, we model the solidification and phase-change-driven flow in a ternary alloy cooled from a planar boundary. The liquid and solid phases are separated by a sharp interface. The model incorporates a fluid flow in the liquid region due to shrinkage/expansion during the phase change. We derive self-similar solutions for the temperature field, composition fields and the interface location, and perform an asymptotic analysis in the limit of the large Lewis numbers. In the case of binary systems, the two asymptotic regimes are known in the limit of large Lewis number. One controlled by the thermal diffusivity and one controlled by the solutal diffusivity. In the case of ternary systems studied here, we find that the presence of the second solute leads to eight asymptotic regimes. We identify the material and experimental parameters for which these regimes occur. The results indicate that a sufficient difference in the two solutal diffusivities accounts for the difference in the segregation of the two solutes in the solid phase. We find that a shrinkage upon freezing enhances the solidification rate if the system solidifies in the regime controlled by the thermal diffusivity, but it slows down the solidification rate if the system solidifies in the regime controlled by one or two solutal diffusivities. The expansion has the opposite effect on the rate of solidification in the regimes controlled by either thermal or solutal diffusivities. We also examine the onset of the marginal constitutional supercooling (MCS) in the liquid region above the solid/liquid interface. With the requirements of the MCS not to occur, we identify two novel regimes of solidification in which the system solidifies at a very slow rate. We also provide numerical results which show different effects of the segregation coefficients and the double-solutal diffusive effects on the onset of the MCS.

Finally, in the third part, we propose a one-dimensional model for solidification of supercooled liquids in a finite domain. The classical Stefan-type two-phase model of freezing is extended to account for the kinetic effects at the front separating the solid and liquid phases.

A direct numerical simulation of the model reveals different stages of freezing dynamics: the initial stage dominated by the interfacial attachment kinetics, the intermediate quasi–equilibrium stage, and the late stage dominated by the finite-domain effects. Asymptotic solutions in the limit of small initial supercooling are derived and compared with numerical calculations for the full model.

Key words: Taylor bubbles, asymmetric bubbles, solidification of ternary alloys, supercooled solidification, self-similar solutions, asymptotic approximations

AMS classification: 80A22, 76M45, 35C20

Abstrakt

Dizertačná práca pozostáva z troch častí. V prvej časti prezentujeme výsledky našich laboratórnych experimentov s Taylorovými bublinami pohybujúcimi sa vo vertikálnej trubici za prítomnosti laminárneho toku v smere nadol. Zo získaných experimentálnych snímok následne rekonštruujeme trojrozmerný tvar pozorovaných bublín. Trubica je osvetlená laserovou rovinou kolmou na vertikálnu os trubice. Bubliny prechádzajúce cez laserovú rovinu sú nafilmované vysokorýchlostnou kamerou. Naše laserové merania odhalili, že tvar bubliny v horizontálnej rovine nie je konkávny, ale vykazuje depresiu v okolí stredu bubliny. Zistili sme, že na rozdiel od rýchlosti asymetrických bublín, tvar bublín projektovaný na rovinu rovnobežnú s osou trubice závisí na strednej rýchlosti toku smerujúceho nadol, v ktorom sa bubliny pohybujú. Asymetrické bubliny majú väčšiu krivosť pri vyšších rýchlostiach toku. Prezentujeme aj jednoduchý neviskózny model, ktorý vysvetľuje túto závislosť.

V druhej časti modelujeme proces tuhnutia a tok hnaný expanziou a kontrakciou v ternárnom systéme tuhnúcom z pevného rozhrania. Kvapalná a tuhá fáza sú oddelené rovinným rozhraním. Model zahŕňa tok v kvapalnej oblasti, ktorý vzniká v dôsledku expanzie alebo kontrakcie pri fázovej premene. Odvádzame sebepodobné riešenia pre teplotné pole, koncentračné polia a polohu rozhrania. Následne prevádzame asymptotickú analýzu v limite veľkých Lewisových čísel. V prípade binárnych systémov sú známe dva asymptotické režimy v limite veľkého Lewisovho čísla. Jeden kontrolovaný tepelnou difuzivitou a jeden kontrolovaný difuzivitou prímesi. V prípade ternárnych systémov študovaných v tejto práci sme zistili, že prítomnosť druhej prímesi prináša osem asymptotických režimov. Určujeme materiálové a experimentálne parametre, pre ktoré sa tieto režimy objavujú. Výsledky ukazujú, že dostatočne veľký rozdiel v difuzivitách prímesí má za následok rozdielnu segregáciu týchto prímesí v tuhej fáze. Zistili sme, že kontrakcia pri tuhnutí urýchľuje jeho rýchlosť, ak systém tuhne v jednom z režimov kontrolovaných tepelnou difuzivitou a naopak spomaľuje tuhnutie, ak systém tuhne v jednom z režimov kontrolovaných jednou alebo oboma difuzivitami prímesí. Expanzia pri fázovej premene má opačný efekt na rýchlosť tuhnutia pri režimoch kontrolovaných teplotnou difuzivitou alebo difuzivitou prímesi. Tiež preskúmame objavenie sa marginálneho konštitučného podchladenia (z angl. MCS) v kvapalnej oblasti nad rozhraním tuhej a kvapalnej fázy. Pri požiadavke, aby sa MCS neobjavilo, identifikujeme dva nové režimy tuhnutia, v ktorých systém tuhne veľmi pomaly. Poskytneme tiež numerické výsledky, ktoré ilustrujú rozdielny efekt segregačných koeficientov a rôznej difuzivity prímesí na objavenie sa MCS.

Na záver, v tretej kapitole navrhujeme jednorozmerný model pre tuhnutie podchladenej kvapaliny v konečnej oblasti. Klasický Stefanov problém tuhnutia s dvoma fázami je rozšírený tak, že zahŕňa kinetické efekty na rozhraní oddeľujúcom tuhú a kvapalnú fázu. Priama numerická simulácia modelu vykazuje rôzne fázy dynamiky tuhnutia: počiatočnú fázu v ktorej dominujú kinetické efekty na fázovom rozhraní, strednú kvázi-rovnovážnu fázu a záverečnú fázu, v ktorej dominujú efekty spojené s ohraničenosťou oblasti. Odvodíme asymptotické riešenia v limite malých počiatočných podchladení a porovnáme ich s numerickými výpočtami pre plný model.

Kľúčové slová: Taylorove bubliny, asymetrické bubliny, tuhnutie ternárnych zmesí, tuhnutie za prítomnosti podchladenia, sebe-podobné riešenia, asymptotické aproximácie

AMS classification: 80A22, 76M45, 35C20

Contents

1 Reconstruction of fast Taylor bubble shapes

This section is based on our work presented as a poster at the 17th Multiphase Flow Conference & Short Course, Dresden, 2019 [8].

1.1 Introduction

Flows of aerated liquid in the vertical pipe attract wide interest of researchers in both scientific and technical applications. A common pattern occurring in such flows are the Taylor bubbles – elongated bullet-shaped bubbles. Pioneering work on Taylor bubbles rising in the stagnant liquid was done by Dumitrescue in [16] and by Davies and Taylor [13]. Both studies involved theoretical prediction on the shape of the bubble tip, based on the inviscid theory. In [13] an attempt was made to predict the bubble velocity in the stagnant liquid by the formula $v_D = k\sqrt{gD}$, where g is the gravitational acceleration, D is the pipe diameter. Later experiments ([36], [39], [9]) specified the value of k to be 0.33–0.36.

The Taylor bubble velocity v_b in the liquid flowing with the velocity v_L was determined in the study of Nicklin et al. [36] to be:

$$v_b = C_0 v_L + v_D, \tag{1.1}$$

where C_0 is the constant typically considered 1.2 for laminar and 2 for the turbulent flow [17]. In the upward fluid flow a bubble posses symmetrical shape. The movement of the symmetrical bubble is described by the Nicklin equation (1.1). In the downward flow, the bubble do not always posses the symmetrical shape. As reported in the early experimental studies [22] and [35], for downward fluid flow velocity below the certain critical value, fast elongated asymmetric bubbles occur.

In [34] Mao and Duckler built the numerical model for a symmetric bubble rising in the vertical pipe with the upward fluid flow. The model incorporated the effect of the surface tension. As pointed out it has negligible effect on the bubble shape, but is crucial for determining the bubble velocity. For zero surface tension there exist multiple solutions for the bubble velocity, each corresponding to the different shape. The requirement of the non-zero surface tension implies that the bubbles nose has a spherical shape and ensures one solution for the bubble velocity. Later, the study of Fabre and Figueroa-Espinoza [20] was dedicated to a planar bubble rising in the channel with flowing liquid. Both downward and upward flows were allowed in their model. For the sufficiently large flow velocity, the transition of the bubble from the symmetric to the steady asymmetric mode was observed. Even thought the bubble transits to the asymmetric mode, it is not attached to the channel wall. There is always a liquid film present between the bubble and the channel wall. The bubble shape becomes more pointed as the downward flow increases. In the numerical study of Lu and Prosperetti [33] the axisymmetric elongated bubble rising in the vertical water-filled channel was modelled. Predicted fluid flow velocities around the bubble nose showed very good agreement with the particle image velocimetry (PIV) measurements of Bugg and Saad [3].

Lu and Prosperetti [32] performed a linear stability analysis of the elongated bubble shape in the downward fluid flow. For the base flow, they used the same approximation as addopted by Collins et al. in [10], in which the viscosity effects are accounted only through the non-zero vorticity of the base flow. The linear perturbation is considered to be irrotational. The main result presented in [32] is that the symmetrical shape becomes unstable for the downward flow velocity lower than $-0.13\sqrt{gD}$.

Recently two experimental studies [17] and [19] systematically investigated the fast asymmetric elongated bubbles present in the downward fluid flow. In [17], Fabre and Figueroa-Espinoza used three different fluids and provided results on the bubble shape and velocity for different mean flow velocities and surface tension parameters. For small surface tensions and the mean flow velocity below a critical value specified in [32], they observed the fast asymmetric bubbles rising with the velocity $0.4\sqrt{gD}$ for a wide range of the downward mean flow velocities. This independence of the bubble velocity of the flow velocity is in strong contradiction to the linear relation (1.1) valid for the symmetric bubble moving in the vertical fluid flow, where the bubble velocity decreases with decreasing fluid flow velocity. More recently, Fershtman et al. [19] studied the shapes and velocity of the elongated bubble in the downward fluid flow also confirming the critical velocity of the downward fluid flow predicted in [32]. The stable asymmetric mode they observed exists only for the limited time after the flow is initiated. They also provided a theoretical prediction for the time of the onset and duration of the asymmetric mode, which was found to be in agreement with their measurements.

The aim of the present study is to experimentally investigate the shape of the asymmetric elongated bubble observed in [19]. The paper is organised as follows: in §1.2 we describe the experimental facility and experimental technique used to obtain the bubble shape. Before we proceed to investigate the asymmetric mode we apply the laser method to the well-known symmetric case. In §1.4 we present a simple inviscid model for the prediction of the bubble shape for the given bubble velocity and downward fluid flow velocity. In §1.5 we present the results for the measurement of the bubble shape in the asymmetric mode. Finally in §1.6 we give the conclusions.

1.2 Experimental facility and procedure

1.2.1 Experimental facility

Measurements conducted in [19] showed that axisymmetric Taylor bubbles, under the presence of the sufficiently large downward flow, transit to the steady asymmetric mode. In the presented work we experimentally examine the shapes of these elongated asymmetric bubbles. Schematic diagram of our experimental facility is depicted in Figure 1. Water is pumped from the bottom reservoir to the upper reservoir and flows down through the vertical Perspex pipe against the rising bubble. The internal radius of the pipe is $R_p = 22\,\mathrm{mm}$ and the length of the pipe is 6 m. To ensure a symmetric and smooth entrance of the water into the pipe, the upper reservoir consists of a large settling chamber, a honeycomb and a converging nozzle. The flow rate is determined by three Fischer-Porter rotameters with the maximum flow rates 3.80 l/min ($0.228\,\mathrm{m}^3$/h), 22.9 l/min ($1.376\,\mathrm{m}^3$/h), and 66 l/min ($4\,\mathrm{m}^3$/h) and an accuracy 1.6% of their full scale. Mean downward flow rates in the conducted experiments were below $0.5\,\mathrm{m\,s}^{-1}$. To avoid the deformation of an image due to the cylindrical shape of the pipe, part of the pipe in the measurement section is enclosed in a transparent plastic box. The space between the box walls and the pipe is filled with the water.

Individual bubbles were injected from the air chamber, where the air is pressurised. Injection is controlled by the computer connected to the injection valve. The length of the investigated bubbles is up to 30 cm.

To reconstruct the bubble shape, we use the laser beam transformed to the laser sheet using the line generator. The tube is crossed by the laser sheet as shown in Figure 3. We also take snapshots of the bubble from the side (see Figure 2). Such method is simple, however it does not provide the possibility to reconstruct the shape of the bubble. The frame rate of the video camera used is 180 fps.

1.3 Procedure

Initially, a symmetric Taylor bubble is injected into the vertical pipe. The downward flow is introduced only after the bubble is in the steady position in the middle of the pipe. After the time experimentally determined in [19] the bubble transits to the asymmetric mode.

Series of snapshots is taken when the asymmetric bubble is crossing the laser sheet. To test our laser measurement technique of the bubble shape, we first analysed axisymmetric Taylor bubble. The sample image is shown in Figure 4(a).

Processing of the image was performed in the following four steps 1. snapshots were taken with the camera (Figure 4(a)), 2.perspective transformation was made (Figure 4(b)), 3. the

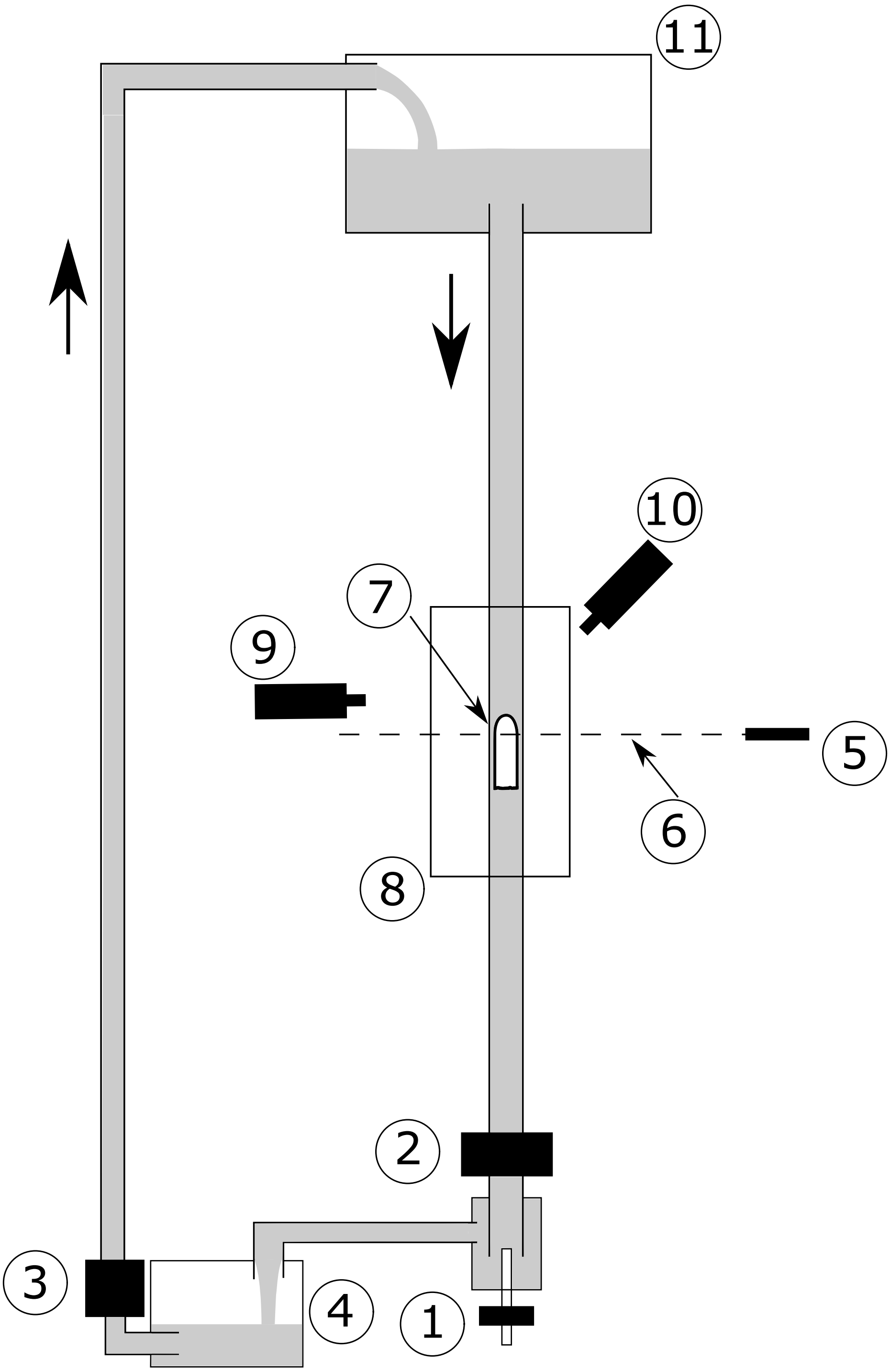

Figure 1: The experimental facility: 1, bubble injection valve; 2, flowmeter, 3, pump; 4, bottom water reservoir; 5, laser source; 6, laser sheet; 7, bubble crossing the laser sheet; 8, box encapsulating the pipe; 9, side view camera perpendicular to the pipe; 10, perspective camera; 11, upper water reservoir with honeycomb and converging nozzle.

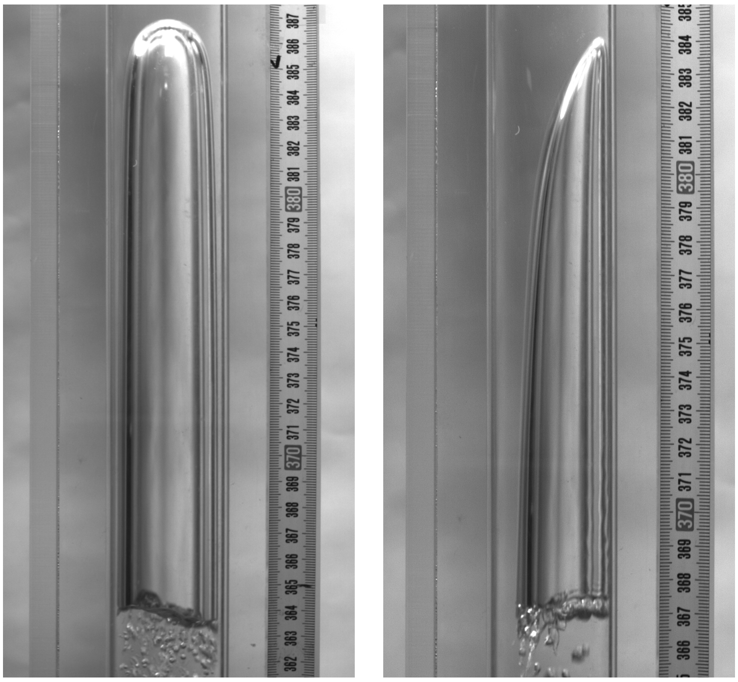

(a) (b)

Figure 2: Sample images of the bubble in (a) the symmetric and (b) the asymmetric modes.

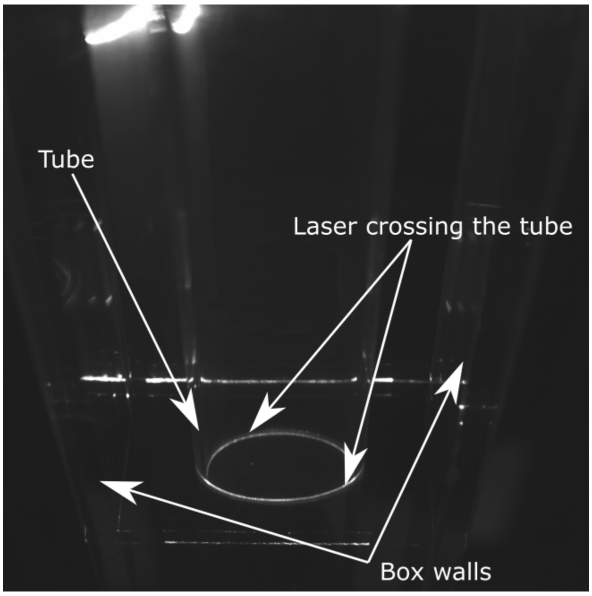

Figure 3: Sample image of the empty tube crossed by the laser sheet

bubble edge was detected (Figure 4(c)), 4. the detected bubble edge was extracted (Figure 4(d)). We note that to make the bubble edge easier to distinguish we transformed all the grey pixels bellow a specific threshold to black and all the pixels with the larger value to white on the raw image. To detect the bubble edge on the obtained images we used Canny edge detection algorithm developed by J. Canny [4] and implemented in `Python` library `OpenCV` by the command `Canny()`. On some images, there are many reflections as can be seen e.g. in Figure 7(a). In such cases we marked the bubble edge manually on the transformed image and consequently extracted the edge.

We see that in the final Figure 4(d) the distance of the bubble edge from the pipe wall corresponds to the thickness of the gap between the bubble and the pipe in Figure 2(a). The apparent discontinuity in the pipe wall in the Figures 4(a–c) is caused by the non-zero thickness of the pipe wall.

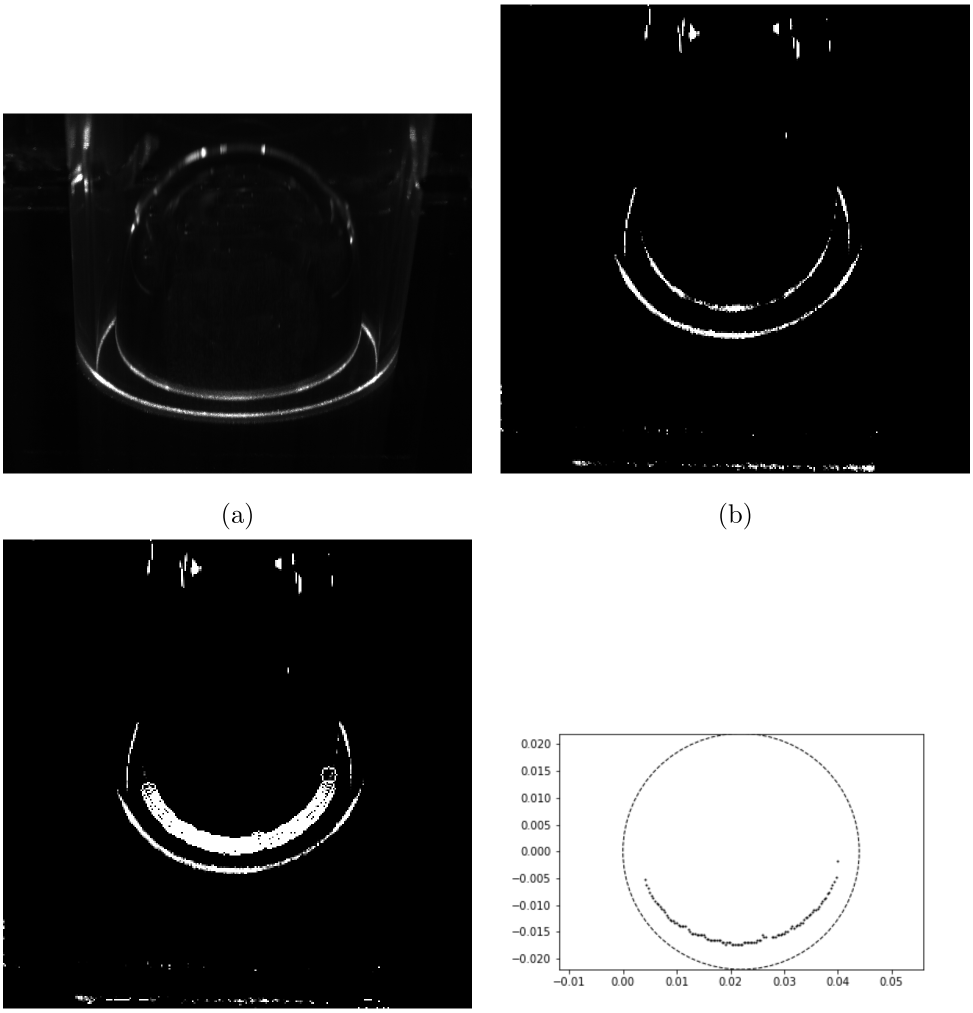

(a) (b)

(c) (d)

Figure 4: Steps of the image processing in the laser method. Axisymmetric bubble is shown on the images. (a) Raw image (b) image modified by the perspective transformation, (c) detected bubble edge marked with the circles and (d) obtained bubble edge is plotted to the final figure.

1.4 Inviscid model

Here we formulate a simple inviscid model from which we can deduce the bubble shape as viewed from the side. Schematic of an asymmetric elongated air bubble rising in the downward flow is depicted in Figure 5.

We formulate the global model in the frame of reference, in which the bubble is stagnant. The average cross–sectional fluid velocities at heights A and B are

$$v_{A,B} = v_b + v_{dA,B}, \tag{1.2}$$

where v_b is the bubble velocity in the laboratory frame of reference and $v_{dA,B}$ are the down-

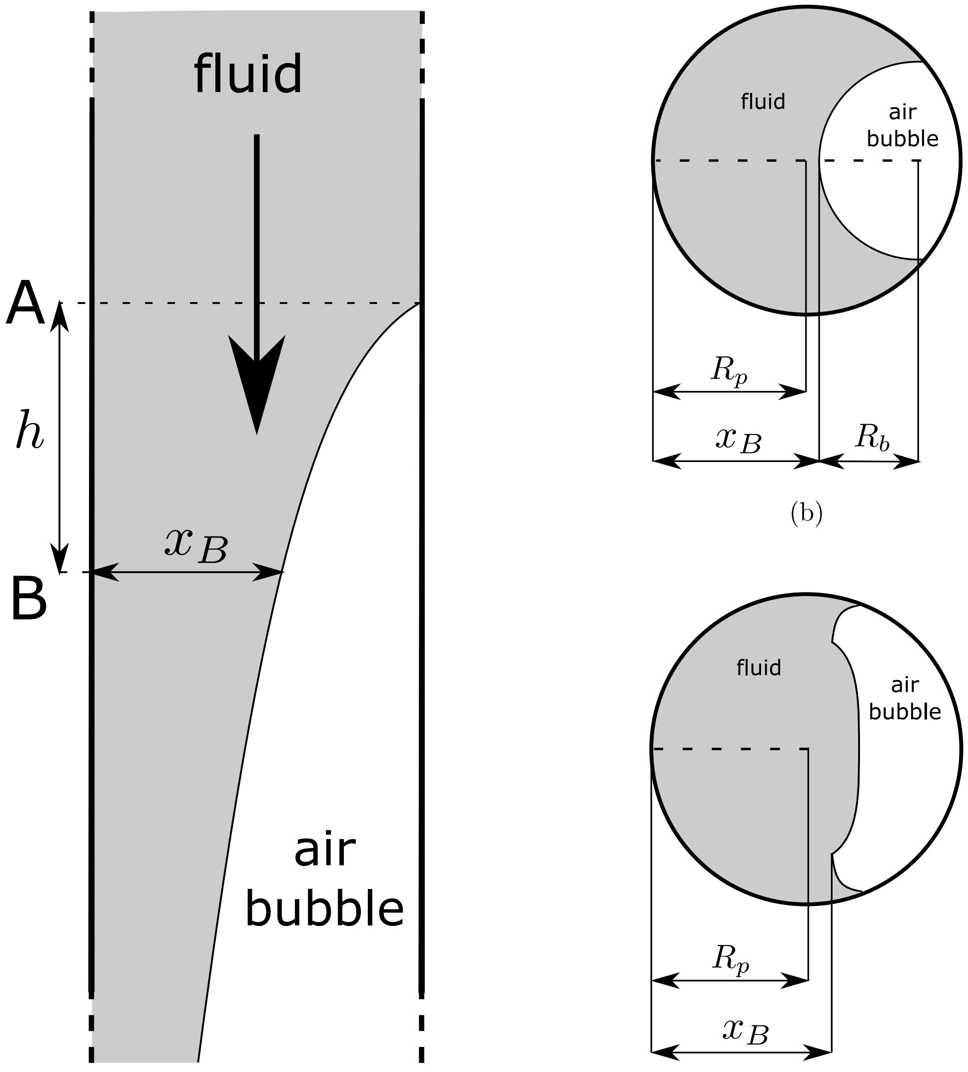

(a) (b) (c)

Figure 5: Schematic of the elongated air bubble rising in the pipe against the downward fluid flow. (a) The bubble as viewed from the side. Sample bubble horizontal cross-section at height h below the bubble top under the assumption of the (b) circular and (c) non-circular bubble edge.

ward fluid velocities at heights A and B in the laboratory frame of reference.

The model is described by the following equations:

Zero pressure drop: $$p_A = p_B \tag{1.3}$$

Continuity equation: $$v_A A_A = v_B A_B \tag{1.4}$$

Bernoulli's equation: $$\frac{1}{2}\rho v_A^2 + \rho g h_A + p_A = \frac{1}{2}\rho v_B^2 + \rho g h_B + p_B, \tag{1.5}$$

where ρ is density of the fluid, p is the fluid pressure, h is the vertical distance measured from the bubble top, A is the cross sectional area occupied by the fluid and g is the gravity acceleration. Lower index A indicates the upper position and index B lower position. Combining equations (1.3)–(1.5) yields

$$h\left(x_B\right)=\frac{1}{2g}v_A^2\left(\left(\frac{\pi D^2}{4A_B}\right)^2-1\right), \tag{1.6}$$

where A_B is the bubble cross-section corresponding to the distance x_B (see Figure 5). We computed A_B numerically for the shape of the bubble obtained from the experiment. For the side view of the bubble, the shape of the cross-section is unknown. Therefore the circular shape of the bubble was assumed (see Figure 5(b)), with the bubble cross-sectional radius R_b being an additional input parameter. If the cross-sectional shape of the bubble is known, which is the case for the experiments with the laser sheet enlightening the bubble from the front side, we might calculate the cross–section directly from the experimental data. In that case x_B is considered to be the leftmost point of the given cross–section (see Figure 5(c)). We note that the bubble velocity is not determined by the model. We use the experimentally measured bubble velocity as one of the input parameters to the model.

In the section 1.5 we compare the shape given by the equation (1.6) with the experimentally obtained bubble shape.

1.5 Results

In [37] was showed that bubble shape and motion is only affected by the fluid flow ahead of the bubble. Our measurement of the edge of the bubble in the asymmetric mode from the side view confirms this fact. Edges of the bubbles with different volumes as seen from the side overlap, as can be seen in Figure 6(a). Furthermore, bubble is more pointed for the larger values of the downward fluid flow (see Figure 6(b)). We note that the bubble shape is constant in time and remind unchanged also for the different height at which the bubble image is obtained.

Same as in the case of the symmetric bubble, we have processed the images obtained when the bubble was in the asymmetric mode. Time laps for the bubble in the asymmetric mode crossing the laser sheet is showed in the 7. So far, we had not been capable of reconstructing the bubble top. At the time when bubble tip is crossing the laser sheet, there are a lot of reflections in the images and is hard to determine the bubble edge position precisely. On the other hand the bubble interface is clear in the middle and the bottom part of the bubble. Our laser measurements revealed that the cross–section of the bubble in the asymmetric mode is not circular, but there is an unexpected change in the bubble shape (see Figure 7). Possibly this reflects the profile of the downward fluid flow, which is strongest on the pipe central axis.

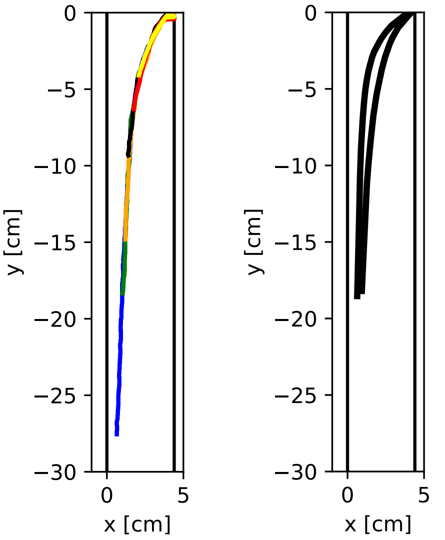

Figure 6: Bubble edge detected from the side view images. a) Overlapping bubble edges extracted from the side view images. Different colours denote different bubble lengths. Flow rate is $v_d = 0.30\,\mathrm{m\,s^{-1}}$. b) Edges of the two bubbles with the same length for the two different flow rates: $v_d = 0.13\,\mathrm{m\,s^{-1}}$ and $v_d = 0.30\,\mathrm{m\,s^{-1}}$. Bubble is more pointed for the larger flow rate.

Here we compare the data of the bubble shape obtained by laser measurements and the side view images with the theoretical prediction for the bubble shape given by the equation (1.6). The experimental data obtained from the side view images are plotted in Figure 8(a) (dots). To calculate the cross-section A_B in (1.6) we supposed that $R_b = 10R_p$, which corresponds to the flat bubble. The assumption of the flat cross-section of the bubble is in the agreement with the laser measurements showed in Figure 7.

The single points in Figure 8(b) represent the lowest points of the corresponding bubble cross–section (see Figure 7). We calculated $A_B(x_B)$ directly from the laser measurement data, for each frame. The equation (1.6) is than used to plot the solid curve in Figure 8(b).

To show that data obtained independently by the laser measurements and the bubble images coincide, we displayed them in one plot in Figure 8(c).

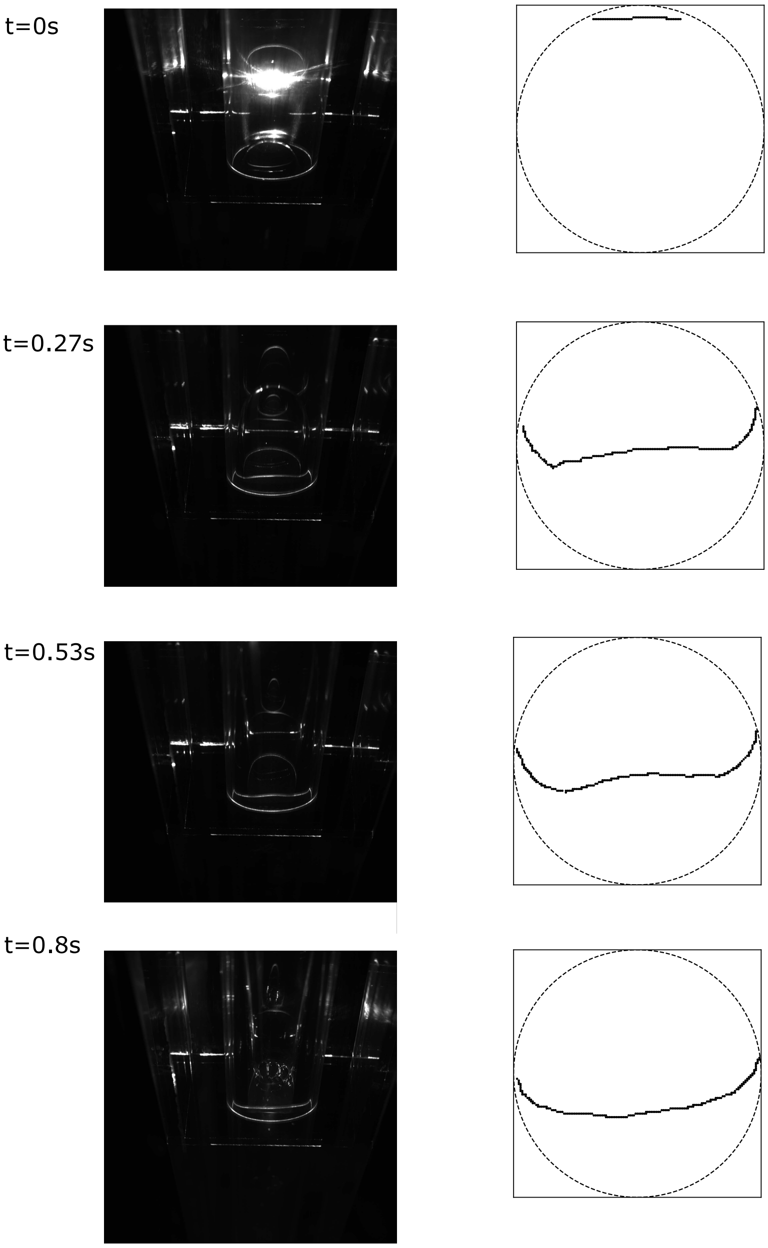

Figure 7: Bubble crossing the laser sheet in four consecutive frames. In the left column are depicted the raw images from the high-speed camera. In the right column are depicted the bubble edges, detected from the images. At the first image, bubble tip is crossing the laser sheet. At the second and third image we see the depression in the bubble centre. At the last image, corresponding to the bottom of the bubble, the depression is not present.

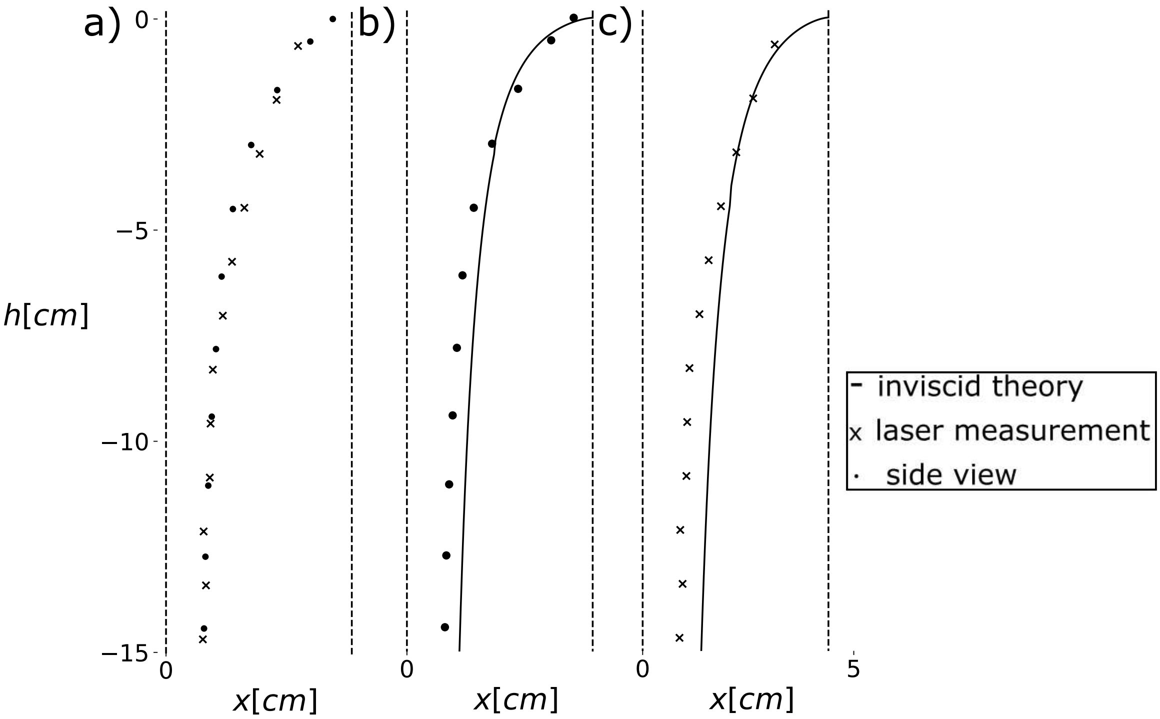

Figure 8: Comparison of the bubble shape obtained from: (a) the side view and laser measurements, (b) the side view experiments and the theory, and (c) the side laser measurements and from the theory. The theoretical curves are plotted based on equation (1.6).

Figure 8(c) indicates that the laser measurements give the same results for the bubble edge as viewed from the side as the side view images. Another way to justify the reconstruction of the bubble shape by the laser method, is to verify that the volume of the bubble in the symmetric and the asymmetric mode is the same. We made the photo of the bubble in the symmetric and in the asymmetric mode. Under the assumption of the cylindrical symmetry of the bubble we calculated the bubble volume numerically. For the bubble in the asymmetric mode, we measured the bubble edge as the bubble moved thought the laser sheet. Sample bubble edge is depicted in Figure 7. We calculated the volume of the bubble V_b using the formula $V_b = \sum_i A_i v_b/f$, where A_i is the cross-sectional area of the bubble, v_b is the bubble velocity and f is the frame rate of the camera. For the 17 cm long bubble, we calculated the volume 0.108 l for the symmetric bubble and 0.110 l for the asymmetric bubble. We see that the values are in very good agreement.

1.6 Discussion

We have reconstructed the shape of the fast asymmetric elongated air bubbles in the vertical pipe under the presence of the downward fluid flow. To produce the fast asymmetric elongated bubbles we used the same procedure as in [19] – downward flow was initiated after the bubble was rising in the stagnant water in the steady position in the middle of the pipe.

To justify the precision of our laser method, we have reconstructed the shape which would be observed if viewed from the side based on the laser measurements. Consequently we have compared it to the side view image, obtaining good agreement. We have also calculated the volume of the bubbles in the symmetric and asymmetric mode for the given injection time. Calculated volumes of the bubbles in the asymmetric mode have showed good agreement with the volumes of the bubbles in the symmetric mode, produced during the same injection time.

Laser measurements have revealed that the bubble cross-section in the plane perpendicular to the pipe axis is not concave, but there is a depression in the bubble shape reflecting the strongest flow in the middle of the pipe. Despite the fact that the velocity of the asymmetric bubble does not depend on the downward fluid flow, we found change in the shape of the bubble with the flow velocity. For the larger flow rate, asymmetric bubble is more tapered.

We have presented the simple inviscid model, from which we were able to deduce the bubble shape. Predicted bubble shape is in agreement with our experimental method.

2 Solidification of a ternary alloy with density change effects

2.1 Introduction

In recent decades, a lot of research was dedicated to investigate the solidification processes of binary (see e.g. [14], [2]) and multicomponent mixtures. This research is motivated by a wide spectrum of natural and industrial processes. In nature, such processes include solidification in the Earth's core, ice shelf formation and sedimentation in magma lakes. Examples of similar processes in the industry include casting of multicomponent metal alloys [12], phase-change proceses at the nanoscale ([25], [26]), and ice-templating [15]. The technologies are extensively studied due to their importance in producing novel materials.

Worster [40] investigated self-similar model of diffusion-controlled solidification from the cooled boundary. He presented two models for the solidification of the binary system. One with the planar solid/liquid interface and second with the mushy zone. Results of the model were in agreement with the experimental data for the aqueous solution of H_2O–$NaNO_3$ obtained by Huppert and Worster [27]. Chiareli and Worster [7] included a partial solute rejection and a flow due to contraction/expansion during phase change to the model. The flow alter macrosegregation and has an effect on the morphological stability of the system.

Different self-similar model is the one investigated by Kyselica and Guba [30]. The work studies solidification of the binary alloy with a non–plannar interface over the horizontally moving substrate. They found a self-similar solution involving strong two-dimensional fluid flow in the limit of small Prandtl number, which is the typical case for the metal alloys. Asymptotic regime of a small ratio of the square root of the far-field velocity and the moving substrate velocity was investigated. They showed that the height of the solid is of the order of this ratio. The thermal and the compositional boundary layers are both stretched by the factor inversly proportional to the velocity ratio. Kyselica, Guba and Hurban [31], included mushy zone to the model and found out that the thickness of both solid and the mushy regions were of the unit order. In this section we address the problem of solidification of the ternary alloy with the planar interface from a cooled boundary. We focus on the solidification controlled by diffusion of solute(s) with a different diffusion coefficient of each solute. We have been able to predict novel regimes of solidification, unique for the ternary alloys solidification. Our model includes the liquid flux due to contraction/expansion during the phase change. The model is a natural extension of the model for binary alloys, by Worster and Chiareli [7] to the ternary case.

This section is organized as follows. In §2.2 we formulate the problem. We find the solutions underlying the model in a self-similar form. This approach enables us to transform the set of the governing differential equations to the set of algebraic equations. In §2.4 we use asymptotic methods to determine the material and experimental parameters for which the solidification process is controlled by the specific diffusivity of solute(s) or heat diffusivity. In each of this regimes we determine asymptotic expression for amount of solutes segregated at the interface if possible. We compare asymptotic and numerical results to show, they are in agreement.

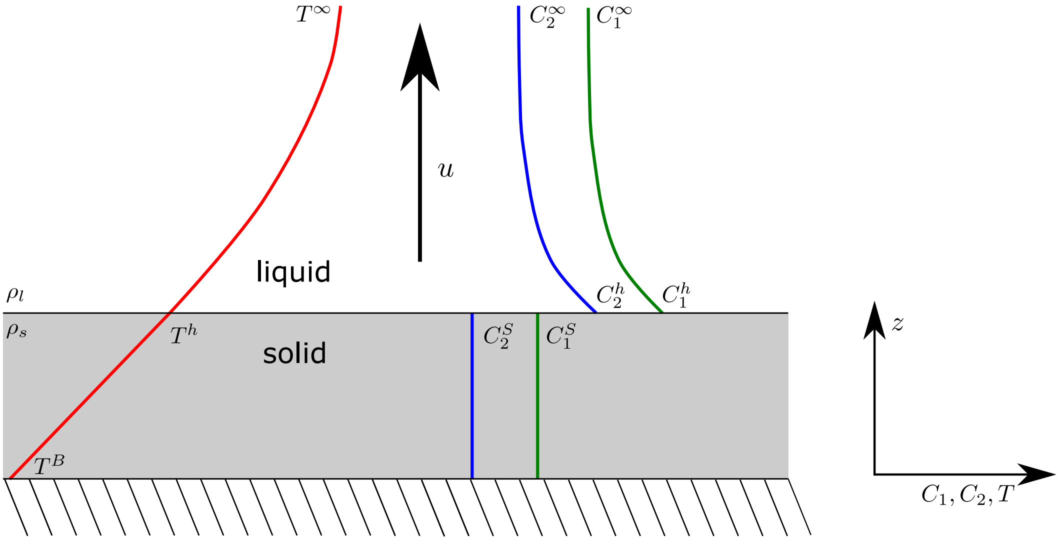

Figure 9: Schematic diagram of the ternary system solidifying from a cooled boundary with a flat solid/liquid interface. The flux in the melt, given by the velocity field u, is determined by the density ratio ρ_s/ρ_l. In the case of $\rho_s < \rho_l$, which is the usual case for the aqueous solutions, the flux is from the interface. However our model is general and includes also the cases $\rho_s > \rho_l$ and $\rho_s = \rho_l$.

We show that for the specific material and experimental parameters the flow due to shrinkage/expansion upon the phase change can both enhance and slows down the solidification rate. In §2.4.5 we analyze conditions for the onset of the supercooling. Finally in §1.6 we provide some conclusions.

2.2 Formulation

We consider the solidification of a ternary alloy in the semi-infinite region from the planar boundary (see Figure 9). The mathematical model is one-dimensional and time-dependent. Solutes can diffuse in the liquid, but we neglect any mass transfer in the solid phase. Solid and liquid are separated by the planar interface $h = h(t)$. The temperature of the bottom boundary, T^B and the temperature of the melt T^∞, at $z \to \infty$ are held constant. The concentrations in the melt at $z \to \infty$, $C_{1,2}^\infty$ are held at constant values as well. Along with the authors of the studies [23] and [24] we consider same values of the thermal conductivity and thermal diffusivity for both the solid and liquid phases.

2.2.1 Phase diagram

Solid and liquid phases are in the thermodynamic equilibrium when the phase change takes place. Temperature at which the melt is in thermodynamic equilibrium with the solid phase at given solute concentrations is determined by the ternary phase diagram. Cooling path of the liquid element is located in the one corner of the ternary phase diagram, as depicted in Figure 10.

Evolution of the liquid element during the solidification process is following. Liquid begins to cool at temperature T^{∞} and concentrations of the solutes C_1^{∞} and C_2^{∞}. It reaches the solid/liquid interface at T^h, C_1^h and C_2^h. Concentration of the solutes frozen into the solid, C_1^S and C_2^S remain constant once solidified in and are given by the segregation coefficients. We note that the liquid element touches the liquidus surface only in one point.

2.2.2 Conservation equations

We formulate the model in terms of differential equations. In the region of the solid phase, $z < h(t)$, the temperature field is governed by the diffusion equation:

$$\frac{\partial T}{\partial t} = \kappa \frac{\partial^2 T}{\partial z^2}. \tag{2.1}$$

In the liquid region, $z > h(t)$, we have mass transfer due to Brownian diffusion and phase change driven convection. Hence the solutal and the temperature fields are governed by the set of the convection–diffusion equations:

$$\frac{\partial T}{\partial t} + u\frac{\partial T}{\partial z} = \kappa \frac{\partial^2 T}{\partial z^2}, \tag{2.2}$$

$$\frac{\partial C_i}{\partial t} + u\frac{\partial C_i}{\partial z} = D_i \frac{\partial^2 C_i}{\partial z^2}, \qquad \text{for } i = 1, 2, \tag{2.3}$$

where $T = T(z,t)$ and $C_i = C_i(z,t)$ are the temperature and concentration fields respectively and $\kappa = k/(\rho_s C_{ps}) = k/(\rho_l C_{pl})$ is thermal diffusivity. The parameters $\rho_{s,l}$ are densities of the solid and the liquid, $C_{ps,l}$ are specific heat of solid and liquid, k is thermal conductivity and D_i are the diffusivities of the dilute solutes. In this model, we assume that all material parameters are independent on solute concentrations.

The field $u(t)$ in the liquid phase represents a fluid flux from/towards the interface in the case of expansion/contraction respectively. As a consequence of the mass conservation at the

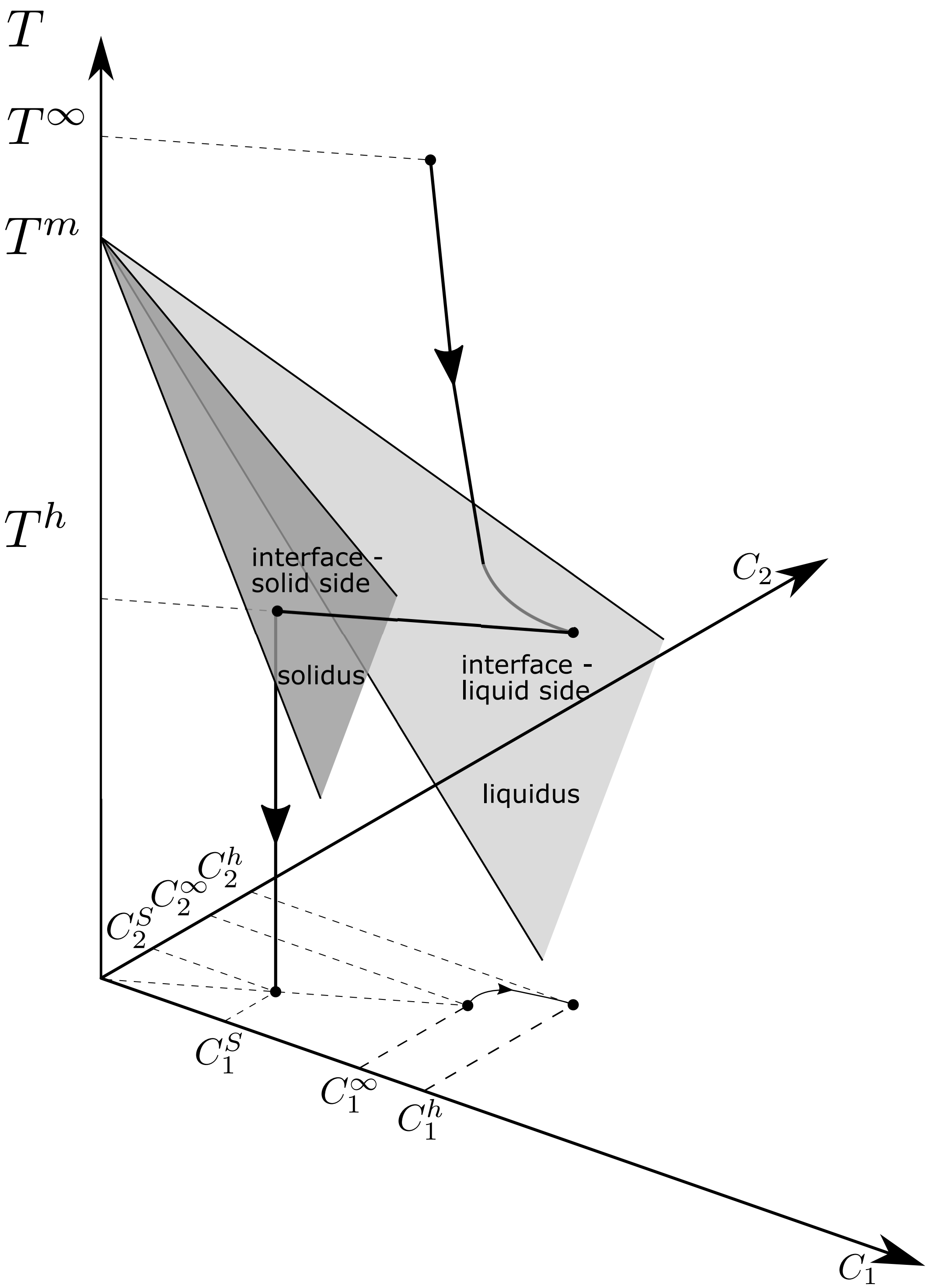

Figure 10: Part of the phase diagram for a ternary alloy in the space C_1, C_2, T. Since temperature is monotonically increasing function of height vertical axis can be understood as the temperature as well as the z coordinate. Thick line represents the evolution of the liquid element during the solidification process. Projection of the cooling path to the space of solute concentration is the straight line only when diffusivities of solutes are the same.

interface, $u(t)$ is given by:

$$u = (1 - r)\frac{\partial h}{\partial t}, \tag{2.4}$$

where $r = \rho_s/\rho_l$ is a density ratio.

Equations (2.1)–(2.3) are subject to the set of boundary conditions prescribed at the bottom boundary, solid/liquid interface and in the far-liquid region. At the bottom boundary ($z = 0$):

$$T(z, t) = T^B. \tag{2.5}$$

At the solid/liquid interface ($z = h(t)$):

$$\text{liquidus constraint:} \quad T(h, t) \equiv T^h, \quad C_i(h^+, t) \equiv C_i^h, \tag{2.6}$$

for $i = 1, 2$, with

$$T^h = T^M - \mathit{\Gamma}_1 C_1^h - \mathit{\Gamma}_2 C_2^h, \tag{2.7}$$

$$\text{energy conservation:} \quad \rho_s L \dot{h} = k\frac{\partial T}{\partial z}\Big|_{z=h^-} - k\frac{\partial T}{\partial z}\Big|_{z=h^+}, \tag{2.8}$$

where L is the latent heat of solidification and $\mathit{\Gamma}_1, \mathit{\Gamma}_2 > 0$ are the liquidus slopes of the liquidus surface in the ternary phase diagram (fig. 10) and T^M is the melting temperature of the pure system.

$$\text{solute conservation:} \quad r(1 - k_i)C_i(h^+, t)\dot{h} = -D_i\frac{\partial C_i}{\partial z}\Big|_{z=h^+}, \tag{2.9}$$

for $i = 1, 2$ and k_i are the segregation coefficients defined as

$$C_i^S = k_i C_i^h, \quad \text{for } i = 1, 2. \tag{2.10}$$

As $z \to \infty$:

$$T(z, t) \to T^\infty, \tag{2.11}$$

$$C_i(z, t) \to C_i^\infty \quad \text{for } i = 1, 2. \tag{2.12}$$

2.3 Self-similar transformation

We use the self-similar transformation

$$\eta = \frac{z}{2\left(D_1 D_2\right)^{1/4} t^{1/2}}, \tag{2.13}$$

to transform the eqn. (2.1)–(2.3) to the form

$$T'' + 2\varepsilon^2 \eta T' = 0, \tag{2.14}$$

$$T'' + 2\varepsilon^2 \left[\eta + \lambda(r-1)\right] T' = 0, \tag{2.15}$$

$$C_1'' + \frac{2}{\mu^2} \left[\eta + \lambda(r-1)\right] C_1' = 0, \tag{2.16}$$

$$C_2'' + 2\mu^2 \left[\eta + \lambda(r-1)\right] C_2' = 0, \tag{2.17}$$

where we have introduced dimensionless solidification rate λ and ε and μ defined as follows:

$$\varepsilon = \frac{(D_1 D_2)^{1/4}}{\kappa^{1/2}}, \quad \mu = \left(\frac{D_1}{D_2}\right)^{1/4}. \tag{2.18}$$

Boundary conditions (2.5)–(2.12) transform to the following equations.

At $\eta = 0$

$$T = T^B \tag{2.19}$$

At $\eta = \lambda$

$$T^h = T^M - \Gamma_1 C_1^h - \Gamma_2 C_2^h, \tag{2.20}$$

$$\frac{L}{C_{ps}} = \frac{1}{2\lambda\varepsilon^2} T' \bigg|_{\eta=\lambda^+} - \frac{1}{2\lambda\varepsilon^2} T' \bigg|_{\eta=\lambda^+} \tag{2.21}$$

$$2r(1-k_1)C_1^h \lambda = -\frac{1}{\mu} C_1' \bigg|_{\eta=\lambda^+}, \tag{2.22}$$

$$2r(1-k_2)C_2^h \lambda = -\mu C_2' \bigg|_{\eta=\lambda^+}, \tag{2.23}$$

$$C_i^S = k_i C_i^h, \quad \text{for } i = 1, 2. \tag{2.24}$$

At $\eta \to \infty$:

$$T \to T^\infty, \tag{2.25}$$

$$C_i \to C_i^\infty \quad \text{for } i = 1, 2. \tag{2.26}$$

Solution of the system of equations (2.14)–(2.17), satisfying the boundary conditions (2.19)–(2.26), can be sought in the form:

$$h = 2\lambda \left(D_1 D_2\right)^{1/4} t^{1/2}, \tag{2.27}$$

$$T(\eta) = T^B + (T^h - T^B) \frac{\operatorname{erf}(\varepsilon\eta)}{\operatorname{erf}(\varepsilon\lambda)}, \quad (\eta < \lambda), \tag{2.28}$$

$$T(\eta) = T^\infty + (T^h - T^\infty) \frac{\operatorname{erfc}(\varepsilon\gamma)}{\operatorname{erfc}(\varepsilon r\lambda)}, \quad (\eta > \lambda), \tag{2.29}$$

$$C_1(\eta) = C_1^{\infty} + (C_1^h - C_1^{\infty})\frac{\operatorname{erfc}(\gamma/\mu)}{\operatorname{erfc}(r\lambda/\mu)}, \quad (\eta > \lambda), \tag{2.30}$$

$$C_2(\eta) = C_2^{\infty} + (C_2^h - C_2^{\infty})\frac{\operatorname{erfc}(\mu\gamma)}{\operatorname{erfc}(\mu r\lambda)}, \quad (\eta > \lambda), \tag{2.31}$$

$$u = (1-r)\lambda\frac{(D_1D_2)^{1/4}}{t^{1/2}}, \quad (\eta > \lambda), \tag{2.32}$$

where we have introduced the variable $\gamma = (r-1)\lambda + \eta$.

We substitute solutions (2.27)–(2.32) into the boundary conditions (2.19)–(2.26), which yields a set of nonlinear algebraic equations for the unknown constants λ, C_i^h:

$$C_1^h = C_1^{\infty}\frac{1}{1-(1-k_1)F(r\lambda/\mu)}, \tag{2.33}$$

$$C_2^h = C_2^{\infty}\frac{1}{1-(1-k_2)F(\mu r\lambda)}, \tag{2.34}$$

$$\frac{L}{C_{ps}} = \frac{T^h - T^B}{G(\varepsilon\lambda)} + \frac{T^h - T^{\infty}}{F(\varepsilon r\lambda)}, \tag{2.35}$$

where

$$F(x) = \sqrt{\pi}x\exp(x^2)\operatorname{erfc}(x), \quad G(x) = \sqrt{\pi}x\exp(x^2)\operatorname{erf}(x). \tag{2.36}$$

Equations (2.33)–(2.35) can be combined into the single equation for λ

$$\left(\mathit{\Gamma}_1C_1^{\infty}\frac{(1-k_1)F(r\lambda/\mu)}{1-(1-k_1)F(r\lambda/\mu)} + \mathit{\Gamma}_2C_2^{\infty}\frac{(1-k_2)F(\mu r\lambda)}{1-(1-k_2)F(\mu r\lambda)}\right)\times$$
$$\left(\frac{1}{G(\varepsilon\lambda)} + \frac{1}{F(\varepsilon r\lambda)}\right) = \frac{\Delta T_L^B}{G(\varepsilon\lambda)} - \frac{\Delta T_L^{\infty}}{F(\varepsilon r\lambda)} - \frac{L}{C_{ps}}, \tag{2.37}$$

where we have introduced

$$\Delta T_L^B \equiv T^M - T^B - \mathit{\Gamma}_1C_1^{\infty} - \mathit{\Gamma}_2C_2^{\infty}, \tag{2.38}$$

$$\Delta T_L^{\infty} \equiv T^{\infty} - T^M + \mathit{\Gamma}_1C_1^{\infty} + \mathit{\Gamma}_2C_2^{\infty}. \tag{2.39}$$

2.4 Results

2.4.1 Regimes of solidification

To complete solutions (2.27)–(2.32), we need to solve the set of transcendental equations (2.33)–(2.35) together with the liquidus constraint (2.20) for constants C_1^h, C_2^h, T^h and λ. For fixed control parameters and material parameters, these constants must be obtained

Quantity	Ni–Al(1)	H_2O–KNO_3(2)	Model ternary systems	
	–Ta(2)	–$NaNO_3$(1)	Single-solutal diffusive	Double-solutal diffusive
T^M[K]	1754	273	273	273
$\mathit{\Gamma}_1$[K %$^{-1}$]	5.17	0.43	0.4	0.4
$\mathit{\Gamma}_2$[K %$^{-1}$]	2.55	0.53	0.4	0.4
$\kappa/10^{-7}$ [m^2 s^{-1}]	164	1.1	100	1
$D_1/10^{-9}$ [m^2 s^{-1}]	5	1.34	1	0.0001
$D_2/10^{-9}$ [m^2 s^{-1}]	5	1.93	1	1
$L/10^5$ [J kg^{-1}]	2.9	3.4	3.4	3.4
$\rho_l/10^3$ [kg m^{-3}]	7.365	1.25	1.0	1.0
$\rho_s/10^3$ [kg m^{-3}]	7.365	9.2	1.0	1.0
$k_1[-]$	0.54	0	0.4	0.4
$k_2[-]$	0.48	0	0.4	0.4
$\varepsilon[-]$	0.02	0.11	0.01	0.01
$\mu[-]$	1	0.69	1.0	0.1
$r[-]$	1	1.36	1.0	1.0

Table 1: List of the material parameter values for the H_2O–$NaNO_3$–KNO_3 ternary system (taken from [40] (heat capacity and latent heat) and [24] (rest of the parameters)) and for the Ni–Al(1)–Ta(2) ternary alloy (taken from [18]). Indices l, s stand for the solid and liquid phases.

numerically. We present numerical values of the physical parameters of our model in Table 1 for the aqueous solution of KNO_3 and $NaNO_3$ and for the Ni–Al–Ta ternary alloy. Material parameters for the two model ternary systems are used to compare numerical and asymptotic results. For the model ternary double-solutal diffusive system, we choose to reduce the value of D_2. This material has unique behavior which cannot be observed in binary systems, as will be shown in what follows. We note that qualitatively similar behaviour would be observed also for the materials with the smaller ratio of solutal diffusivities.

Qualitative insight into the solidification process can be obtained using the following asymptotic expansions for the functions $F(x)$ and $G(x)$:

$$\text{for } x \to 0: \qquad F(x) \sim \sqrt{\pi}x, \qquad G(x) \sim 2x^2 \tag{2.40}$$

$$\text{for } x \to \infty: \qquad F(x) \sim 1. \tag{2.41}$$

According to the values of the thermal and solutal diffusivities in Table 1, it is reasonable to investigate equations (2.33)–(2.35) and eqn. (2.20) in the limit $\varepsilon \to 0$. Eight possible scalings of λ with ε can be identified, under the following assumptions

$$\frac{\varGamma_1 C_1^\infty}{L/C_{ps}} = O(1) \qquad \frac{\varGamma_2 C_2^\infty}{L/C_{ps}} = O(1) \qquad \frac{\Delta T_L^B}{L/C_{ps}} = O(1) \qquad \frac{\Delta T_L^\infty}{L/C_{ps}} = O(1). \tag{2.42}$$

By inspecting the eqn. (2.27) for the position of the solid/liquid interface $h(t)$, limiting cases can be organized in the following four groups.

(I) κ–controlled growth regimes, in which:

  (i) $\lambda = O\left(1/\varepsilon\right)$ provided $\mu = O\left(1\right)$

  (ii) $\lambda = O\left(1/\varepsilon\right)$ provided $\mu = O\left(\varepsilon^{1/2}\right)$

  (iii) $\lambda = O\left(1/\varepsilon\right)$ provided $\mu = O\left(\varepsilon^{-1/2}\right)$

(II) D_1 and D_2–controlled growth regime, in which: $\lambda = O\left(1\right)$ provided $\mu = O\left(1\right)$

(III) D_1–controlled growth regime, in which:

  (i) $\lambda = O\left(\varepsilon^{-1/2}\right)$ provided $\mu = O\left(\varepsilon^{-1/2}\right)$

  (ii) $\lambda = O\left(\varepsilon^{1/2}\right)$ provided $\mu = O\left(\varepsilon^{1/2}\right)$

(IV) D_2–controlled growth regime, in which:

  (i) $\lambda = O\left(\varepsilon^{-1/2}\right)$ provided $\mu = O\left(\varepsilon^{1/2}\right)$

  (ii) $\lambda = O\left(\varepsilon^{1/2}\right)$ provided $\mu = O\left(\varepsilon^{-1/2}\right)$

In the effective binary case ($D_1 = D_2$, $k_1 = k_2$, $C_1^\infty = C_2^\infty$), regimes (I.i) and (II) are analogous to their binary equvivalents presented in [40] and [7]. For further discussion on the effective binary case see [23].

For regimes (I.ii), (III.ii) and (IV.i), where the growth is controlled by the single solutal diffusivity, the binary-equivalent regimes can be obtained in the limit of the nearly binary case ($C_2^\infty \to 0$). To see this, λ must be redefined to $\lambda_{new} = \lambda\mu$ and $\varepsilon_{new} = \varepsilon\mu$ which leads to the desired scaling. Regimes (I.iii), (III.i) (IV.ii) are symmetrical to the regimes (I.ii), (III.ii) and (IV.i) by exchanging indexes 1 and 2.

For small concentration of both solutes the ternary system with $\mu = O\left(1\right)$ is expected to solidify in the same way as a pure melt which corresponds to the regime (I.i). By increasing far-field solute concentrations C_i^∞ (for $i = 1, 2$), the growth becomes to be controlled by solutal diffusivities (regime II). We now derive a criterion for the associated concentrations which mark this transitions.

We take the limit $\varepsilon \to 0$ in the eqn. (2.37) under the assumptions $\lambda = O(1)$ and $\mu = O(1)$ and rearrange the resulting equation in the form

$$\mathit{\Gamma}_1 C_1^\infty \frac{(1-k_1)F\left(r\lambda/\mu\right)}{1-(1-k_1)F\left(r\lambda/\mu\right)} + \mathit{\Gamma}_2 C_2^\infty \frac{(1-k_2)F(r\lambda\mu)}{1-(1-k_2)F\left(r\lambda\mu\right)} = \Delta T_L^B. \tag{2.43}$$

Left-hand side of the eqn. (2.43) is at fixed k_i and C_i^∞ (for $i = 1, 2$) bounded from above. We obtain this upper bound by replacing expression $F(r\lambda\mu)$ by 1. Canceling the same terms on both sides of the resulting equation yields

$$\mathit{\Gamma}_1 C_1^\infty \frac{1}{k_1} + \mathit{\Gamma}_2 C_2^\infty \frac{1}{k_2} = T^M - T^B. \tag{2.44}$$

If $T^M - T^B$ exceeds a transition value given by eqn. (2.44), there is no solution for λ of eqn. (2.43). In that case neglecting the terms in order to obtain eqn. (2.43) from eqn. (2.37) was an inappropriate step and assumption $\lambda = O(1)$ can not be satisfied.

Similar reasoning can be used for the regimes with $\mu = O\left(\varepsilon^{1/2}\right)$ (and $\mu = O\left(\varepsilon^{-1/2}\right)$). We obtain the transition criteria between the regimes (I.ii) $\mapsto$ (IV.i) and (IV.i) $\mapsto$ (III.ii). At first, one obtains the equation analogous to eqn. (2.43) and consequently replace all the remaining functions $F(\mu r\lambda)$ and $F(r\lambda/\mu)$ with 1. Applying such procedure yields the following criteria:

$$\text{(I.ii)} \mapsto \text{(IV.i)} \qquad \mathit{\Gamma}_1 C_1^\infty \frac{1}{k_1} + \mathit{\Gamma}_2 C_2^\infty \frac{1}{k_2} = T^M - T^B. \tag{2.45}$$

$$\text{(IV.i)} \mapsto \text{(III.ii)} \qquad \mathit{\Gamma}_1 C_1^\infty \frac{1}{k_1} + \mathit{\Gamma}_2 C_2^\infty = T^M - T^B. \tag{2.46}$$

$$\text{(I.iii)} \mapsto \text{(III.i)} \qquad \mathit{\Gamma}_1 C_1^\infty \frac{1}{k_1} + \mathit{\Gamma}_2 C_2^\infty \frac{1}{k_2} = T^M - T^B. \tag{2.47}$$

$$\text{(III.i)} \mapsto \text{(IV.ii)} \qquad \mathit{\Gamma}_1 C_1^\infty + \mathit{\Gamma}_2 C_2^\infty \frac{1}{k_2} = T^M - T^B. \tag{2.48}$$

In Figure 11(a-b) we plot lines representing a transition boundaries in the space of far-field concentrations C_1^∞ and C_2^∞ for the given bottom temperature T^B. Due to the symmetry between the regimes (I.iii), (III.i) (IV.ii) and (I.ii), (III.ii) and (IV.i)we did not plot the diagram for the second group of these regimes. We note that expressions (2.44)–(2.48) are independent of ε to the leading order.

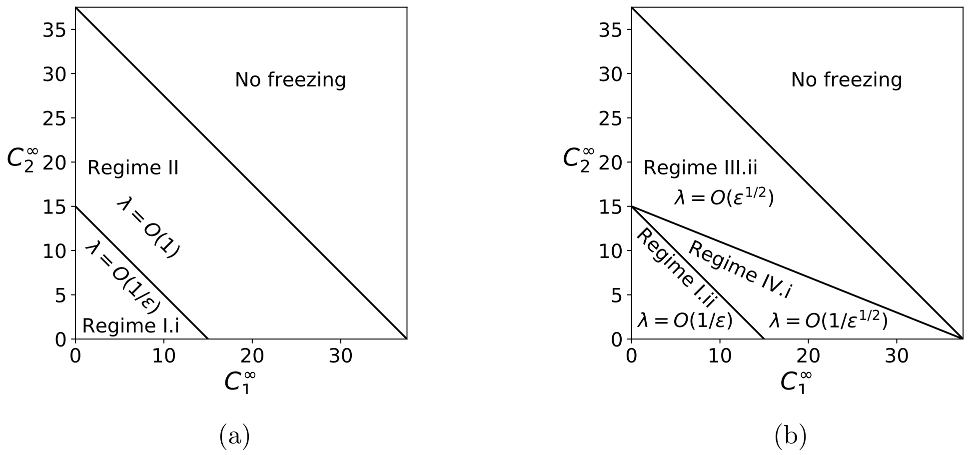

Figure 11: Space of far-field concentrations (C_1^∞, C_2^∞) is divided into distinct regimes of solidification in the limit $\varepsilon \to 0$. In (a) $\mu = 1$, (b) $\mu \sim \varepsilon^{1/2}$. The transition lines are plotted according to (2.44)–(2.48). Values of $k_{1,2}$ and $\Gamma_{1,2}$ are stated in Table 1 for the model single-solutal diffusive (a) and double-solutal diffusive (b) systems. In all plots $T^B = -15$°C.

Area of the regions corresponding to regimes (I.i-ii) in Figure 11 diminishes for k_1 small or k_2 small. Regime (III.i) diminishes for $k_2 = 1$ and regime (IV.i) diminishes for $k_1 = 1$.

2.4.2 Segregation

Important question when dealing with solidification is how much of solute freezes inside of the final solid. In our model ratios of the solute concentrations on both sides of the solid/liquid interface are given by the segregation coefficient (2.10). Solute concentrations on the liquid side of the interface are given by relations (2.33) and (2.34).

When the solidification process is in one of the regimes (I.i-iii), we can obtain the following asymptotic expression for the solute concentrations C_i^h (for $i = 1, 2$)

$$C_i^h \sim \frac{C_i^\infty}{k_i}. \tag{2.49}$$

Important consequence of the simple eqn. (2.49) is that in regimes (I.i-iii) concentration of both solutes freezed in the solid are independent of each other. Asymptotic expression (2.49) is used to plot all non-vertical dotted curves in Figure 12(a–d).

When solidification is controlled by both solutes diffusivities (regime II), in the limit $\varepsilon \to 0$, we obtain the relation

$$\Gamma_1 C_1^h + \Gamma_2 C_2^h \sim T^M - T^B. \tag{2.50}$$

Since the temperature field is increasing function of η, liquidus temperature at the liquid side of the interface can not be lower than the bottom temperature T^B. In this context eqn. (2.50) states that in the regime (II) this upper bound for the solute concentration is reached.

In the regimes (III.i) and (IV.i) the solidification is controlled by the faster diffusing solute. In the regime (IV.i) the faster diffusing solute segregated at the interface is still reaching its maximum value:

$$C_1^h \sim C_1^\infty / k_1, \tag{2.51}$$

while the slower diffusing solute has separated from the asymptotic line $C_2^h \sim C_2^\infty / k_2$. Value of C_2^h is obtained in the following form:

$$C_2^h \sim \frac{1}{\Gamma_2}\left(T^M - T^B - \Gamma_1 \frac{C_1^\infty}{k_1}\right). \tag{2.52}$$

Finally, in regimes (III.ii) and (IV.ii) the solidification rate is controlled by the diffusivity of the slower diffusing solute. In regime (III.ii) for the concentration of faster diffusing solute holds

$$C_2^h \sim C_2^\infty. \tag{2.53}$$

We note that the solute segregation given by the equations (2.52) and (2.53) is unique for the ternary system with large difference in the diffusivities of the single solutes. Agreement of the asymptotic formula (2.52)–(2.53) with numerical results can be seen in Figure 12(d).

Using eqn. (2.53), eq. (2.35) can be rearranged in the form

$$S = \frac{T^M - \Gamma_2 C_2^\infty - \Gamma_1 C_1^h - T^B}{G(\varepsilon\lambda)} + \frac{T^h - T^\infty}{F(\varepsilon r \lambda)}. \tag{2.54}$$

Since $\lambda = O\left(\varepsilon^{1/2}\right)$, in the limit $\varepsilon \to 0$ eqn. (2.54) reduces to the following form

$$\Gamma_1 C_1^h + \Gamma_2 C_2^\infty \sim T^M - T^B. \tag{2.55}$$

In this regime faster diffusing solute shifts the melting temperature of the pure melt T^M by $-\Gamma_2 C_2^\infty$. It plays the same role in the transition criterion (2.46). Amount of faster diffusive solute freezed into the solid is given only by the $\Gamma_2 C_2^\infty$ and k_2, while amount of the slower diffusive solute frozen in the solid is influenced by the far-field concentration of both solutes as well as by both segregation coefficients. In regime (IV.ii) the roles of solutes one and two are interchanged in comparison with regime (III.ii).

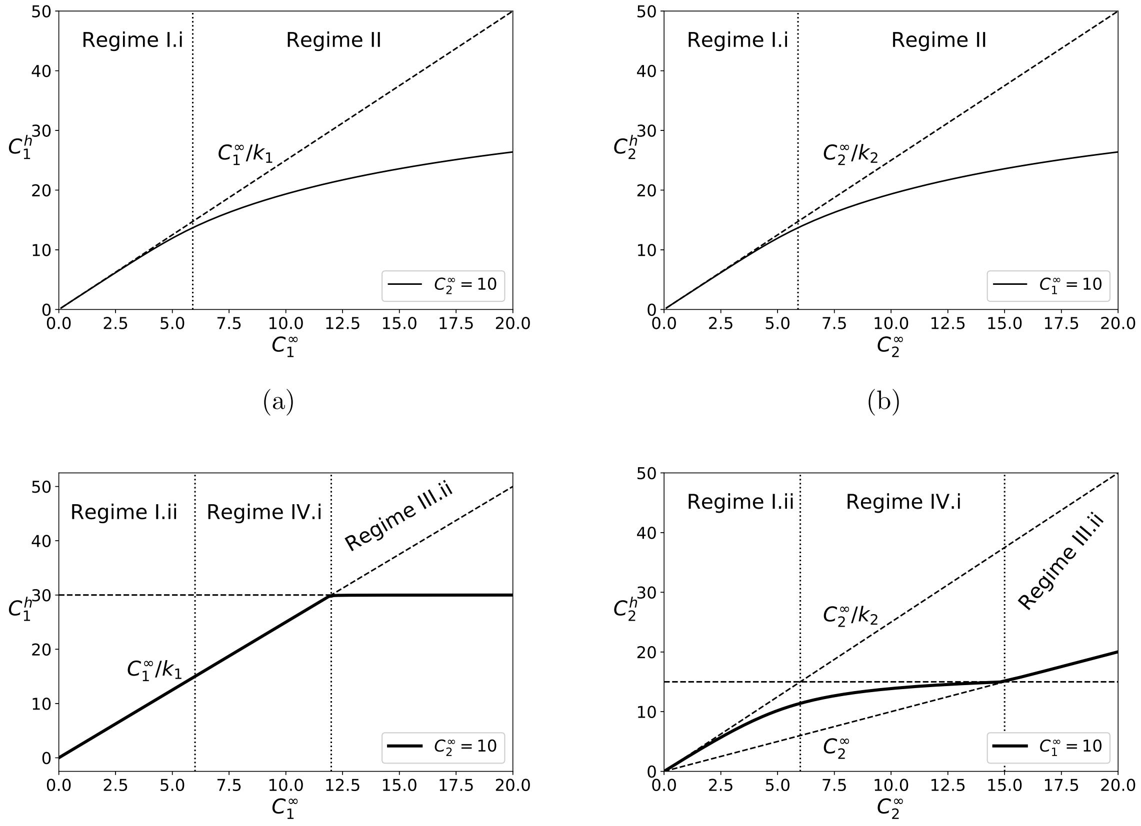

(a) (b)

(c) (d)

Figure 12: Concentrations of the solutes segregated at the liquid side of the solid/liquid interface. Material parameters used to obtain numerical (solid curves) and asymptotic (dashed curves) solutions are listed in Table 1. Dotted vertical lines marks the transitional concentrations given by (2.44)–(2.48). Plots (a) and (b) correspond to single-solutal diffusive model system while plots (c) and (d) to double-solutal diffusive. For the specific meaning of dashed curves see the text in §2.4.2. Temperature of bottom boundary is $T^B = -16\,°\mathrm{C}$ and initial temperature is $T^\infty = 15\,°\mathrm{C}$.

By rearranging asymptotic expression (2.55) to the form

$$C_1^h \sim \frac{T^M - \mathit{\Gamma}_2 C_2^\infty - T^B}{\mathit{\Gamma}_1}, \tag{2.56}$$

we obtain expression for the C_1^h. In Figure 12(c) we see that eqn. (2.56) agrees with numerical results. Dependence of C_2^h on C_2^∞ is depicted in Figure 12(d).

Transition between the regimes is depicted by the vertical dotted lines in Figure 12(a–d). For the single-solutal diffusive case (Figure 12(a-b)) transition concentrations between the regime (I.i) and (II) are computed based on the eqn. (2.44). For the double-solutal diffusive case (Figure 12(c–d)) dotted vertical line marks the transition between the regime (I.ii) and

(III.ii) and dotted vertical line marks the transition between the regime (III.ii) and (IV.i).

2.4.3 Effect of phase-change flow

Our model incorporates flow caused by volume change during the phase change. The flow is induced in the systems solidifying in the gravitational field as well as in the environment without gravity. Fluid flow in the melt region is coupled with the temperature and solutal fields. Heat and solutes are advected from the solid/liquid interface when $r \leq 1$ and towards the interface when $r > 1$.

In §2.4.2 we showed (see eqn. (2.49)–(2.55)) that in the limit $\varepsilon \to 0$ the flow does not influence the solute concentrations segregated at the interface C_1^h and C_2^h. On the other hand, for the specific set of the experimental and material parameters, the expansion or contraction of the solid phase upon solidification has effect on the dimensionless solidification rate λ and on the rate of accretion of the mass to the solid phase $r\lambda$ as depicted in Figure 13 (a) and (c) – single-solutal diffusive cases and 13 (b) and (d) – double-solutal diffusive cases. In the regimes (I.i) and (I.ii) shrinkage ($r > 1$) accelerate the solidification (corresponds to larger λ). On the other hand in the regime (II), (IV.i) and (III.ii) shrinkage decreases the solidification rate. In all cases expansion has the opposite effect. The rate of accretion of the mass to the solid phase proportional to $r\lambda$ is always larger in case of srinkage as depicted in Figure 13(c) single-solutal diffusive case and 13(d) double-solutal diffusive case.

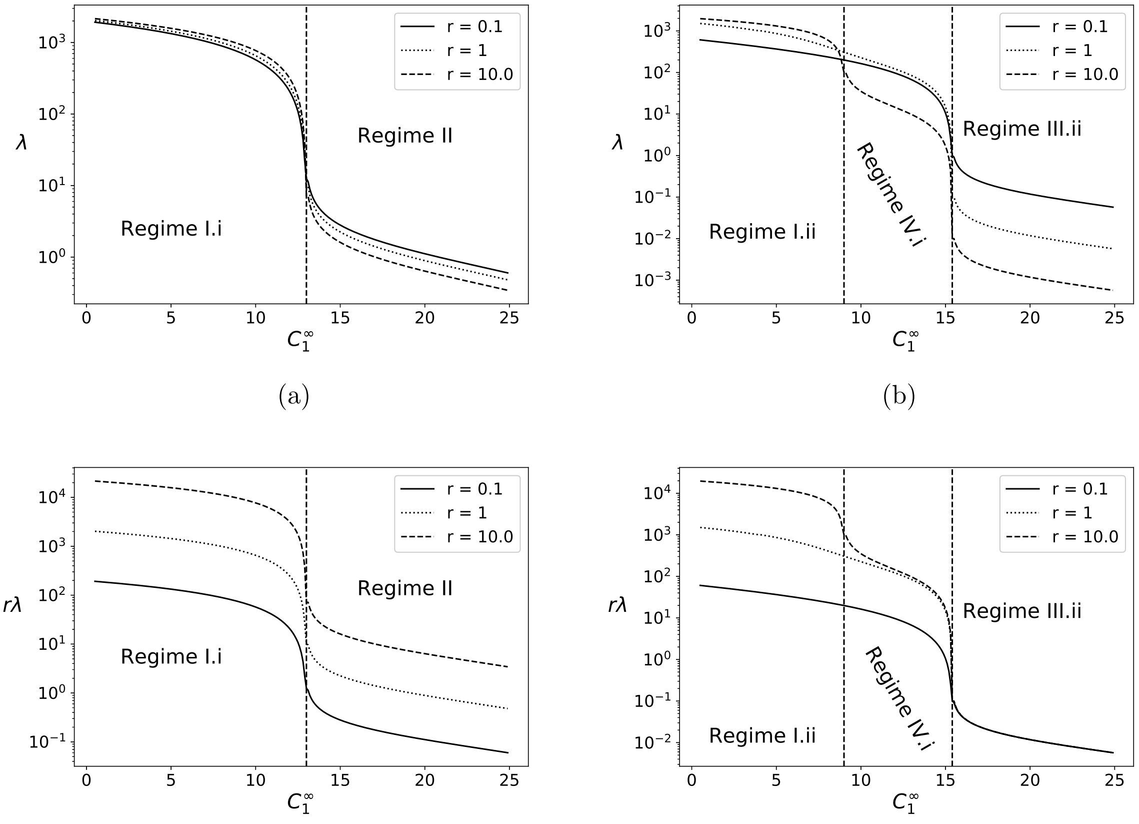

(a) (b)

(c) (d)

Figure 13: Effect of the phase-change driven convection on the dimensionless solidification rate λ and rate of accretion of the mass to the solid phase $r\lambda$. In all Figures $\varepsilon = 10^{-4}$. In the single-solutal diffusive cases (a) and (c) $\mu = 1$ and in the double-solutal diffusive cases (b) and (d) $\mu = \varepsilon^{1/2}$. In all plots $C_2^\infty = 4\,\mathrm{wt}\%$, $T^B = -17\,^\circ\mathrm{C}$ and $T^\infty = 15\,^\circ\mathrm{C}$. Material parameters used to obtain numerical results are stated in Table 1 for the corresponding model cases. Vertical dashed lines represents the regimes boundary based on the (2.44)–(2.48).

2.4.4 Singular behavior of approximate solutions of λ

Full numerical solutions for λ are depicted by the solid lines in Figure 14a) for the single-solutal diffusive case and in Figure 14b) for the double-solutal diffusive case. Superimposed in the same Figures are the approximate solutions for λ (dashed lines) obtained by substituting the approximate expressions (2.49)–(2.56) for C_1^h, C_2^h into the equation (2.37).

To derived the approximate expressions (2.49)–(2.56) we assumed different scaling of λ with ε in the limit $\varepsilon \to 0$, corresponding to the regimes listed §2.4.1. As can be seen in Figures 14(a-b) approximate solutions of λ have singular behaviour near the transition boundaries between the regimes, reflecting the different scaling of λ with ε in each of the regimes.

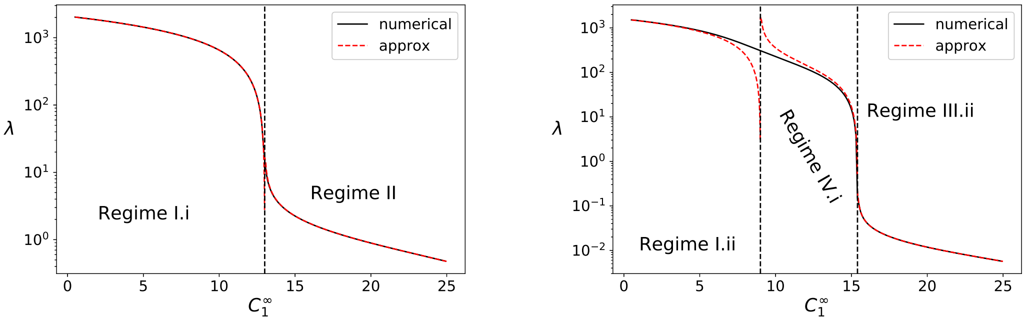

Figure 14: Full numerical solutions of λ obtained as a solution of (2.37) (solid lines) and approximate solutions (dashed lines) obtained by substituting the approximate expressions (2.49)–(2.56) for C_1^h, C_2^h into the equation (2.37) in the corresponding regimes. In Figure (a) solid and dashed lines overlap. Material parameters used to obtain numerical results are stated in Table 1 for the corresponding model cases and $C_2^\infty = 4\,\mathrm{wt}\%$.

2.4.5 Marginal constitutional supercooling

When the ternary melt is cooled from the sufficiently low bottom temperature T^B, undercooled liquid occurs above the interface. In what follows, we investigate what is the bottom temperature, at which the supercooling of the melt in the liquid region occurs. To stress that the bottom temperature is part of our solution, now on we denote it T^B_{crit}.

In the approximation of the same thermal conductivities of the solid and liquid phase supercooling criterion reeds

$$\frac{\partial T}{\partial z}\bigg|_{z=h^+} = -\mathit{\Gamma}_1 \frac{\partial C_1}{\partial z}\bigg|_{z=h^+} - \mathit{\Gamma}_2 \frac{\partial C_2}{\partial z}\bigg|_{z=h^+}. \tag{2.57}$$

Equation (2.57) is a natural generalization of the criterion for supercooling in binary system presented in [40] and [7]. By substituing solutions (2.29)–(2.31) into equation (2.57) we get

$$\Delta T_L^\infty F\left(\frac{r\lambda}{\mu}\right) F(\mu r\lambda)\varepsilon^2 = \mathit{\Gamma}_1 \left(C_1^h - C_1^\infty\right) F(\mu r\lambda) \left[F(\varepsilon r\lambda)\frac{1}{\mu^2} - F\left(\frac{r\lambda}{\mu}\right)\varepsilon^2\right] +$$
$$\mathit{\Gamma}_2 \left(C_2^h - C_2^\infty\right) F\left(\frac{r\lambda}{\mu}\right) \left[F(\varepsilon r\lambda)\mu^2 - F(\mu r\lambda)\varepsilon^2\right]. \tag{2.58}$$

In the limit $C_2^\infty \to 0$ and $\mu \to 1$ the above condition for the marginal constitutional supercooling (MCS) transforms to its binary equivalent

$$\Delta T_L^\infty F(r\lambda)\varepsilon^2 = \mathit{\Gamma}_1 F(r\lambda)(C_1^h - C_1^\infty)\left[F(\varepsilon r\lambda) - F(r\lambda)\,\varepsilon^2\right]. \tag{2.59}$$

Regime	λ	μ	$\Gamma_1 C_1^\infty(1-k_1)/L/C_{ps}$	$\Gamma_2 C_2^\infty(1-k_2)/L/C_{ps}$	$\Delta T^B_{L,\mathrm{crit}}/L/C_{ps}$
(S-I.i)	$1/\varepsilon$	1	ε^2	ε^2	1
(S-II)	1	1	ε	ε	ε
(S-I.ii)	$1/\varepsilon$	$\varepsilon^{1/2}$	ε^3	ε	1
(S-III.i)	$\varepsilon^{-1/2}$	$\varepsilon^{-1/2}$	$\varepsilon^{1/2}$	$\varepsilon^{5/2}$	$\varepsilon^{1/2}$
(S-III.ii)	$\varepsilon^{1/2}$	$\varepsilon^{1/2}$	$\varepsilon^{3/2}$	1	ε
(S-IV.i)	$\varepsilon^{-1/2}$	$\varepsilon^{1/2}$	$\varepsilon^{5/2}$	$\varepsilon^{1/2}$	ε
(S-IV.ii)	$\varepsilon^{1/2}$	$\varepsilon^{-1/2}$	1	$\varepsilon^{3/2}$	ε
(S-V)	ε	1	1	1	ε
(S-VI)	ε^2	$\varepsilon^{1/2}$	1	1	$\varepsilon^{3/2}$

Table 2: Table of important asymptotic scalings of λ and μ with ε and the corresponding order of the dimensionless parameters controlling the solidification. Regimes (S-I.i–S-III.ii) posses the same scaling of λ and μ with ε as the corresponding regimes found in §2.4.1. Regimes (S-V) and (S-VI) represents the only possible cases when the order of the finite far-field concentrations reminds finite for $\varepsilon \to 0$ without occurrence of the supercooling.

To investigate the effect of double-solutal diffusion and difference in segregation coefficients of single solutes on the onset of supercooling, we investigate the ratio of the thermal and liquidus curve gradients at the liquid side of the interface.

$$\frac{-\Gamma_1 \frac{\partial C_1}{\partial z}\Big|_{z=h^+} - \Gamma_2 \frac{\partial C_2}{\partial z}\Big|_{z=h^+}}{\frac{\partial T}{\partial z}\Big|_{z=h^+}} =$$

$$= \frac{\Gamma_1}{\Delta T_L^\infty \varepsilon^2} \frac{C_1^\infty(1-k_1)\left[F(\varepsilon r\lambda)\frac{1}{\mu^2} - F\left(\frac{r\lambda}{\mu}\right)\varepsilon^2\right]}{1-(1-k_1)F\left(\frac{r\lambda}{\mu}\right)} +$$

$$+ \frac{\Gamma_2}{\Delta T_L^\infty \varepsilon^2} \frac{C_2^\infty(1-k_2)\left[F(\varepsilon r\lambda)\mu^2 - F(\mu r\lambda)\varepsilon^2\right]}{1-(1-k_2)F(\mu r\lambda)}. \qquad (2.60)$$

If the gradient ratio (2.60) is of the order $O(1/\varepsilon)$, the liquid above the interface is undercooled. On the other hand if the gradient ratio (2.60) is of the unit order, supercooling tends to diminish. In §2.4.1 we have identified eight regimes of solidification. Each regime corresponds to the specific scaling of λ with ε. As depicted in Figure 11, space of far-field concentrations is for the given T^B divided into the distinct regions corresponding to the regimes. Now, after we have introduced the condition for the onset of the undercooling (2.57), we are not free to choose the order of $\Delta T^B_{L,\mathrm{crit}}/L/C_{ps}$, but this order is determined by eqn. (2.37). Order of $T^B_{\mathrm{crit}}/L/C_{ps}$ consequently follows from eqn. (2.38), under the additional assumption

$(1-k_i) = O(1)$ for $i = 1,2$. For the given scaling of λ with ε, order of the expressions $\mathit{\Gamma}_1 C_1^\infty(1-k_1)/L/C_{ps}$ and $\mathit{\Gamma}_2 C_2^\infty(1-k_2)/L/C_{ps}$ is determined from the requirement of the gradient ratio (2.60) being of the unit order. Natural question to ask is what is the order of $\mathit{\Gamma}_1 C_1^\infty(1-k_1)/L/C_{ps}$, $\mathit{\Gamma}_2 C_2^\infty(1-k_2)/L/C_{ps}$ and $\Delta T_{L,\mathrm{crit}}^B/L/C_{ps}$ for which the scaling of λ and μ with ε is the same as in the regimes found in §2.4.1. We found these orders for each of scaling of λ and μ with ε found in §2.4.1. Results are shown in Table 2. We see that if we demand the same scaling of λ and μ with ε as in the regimes found in §2.4.1, at least one of the far-field concentration needs to be very small. To stress that these regimes are not derived under the assumptions (2.42), but with the supercooling condition (2.60) we denote them with S.

The only possible scaling of λ with ε, which corresponds to the $\mathit{\Gamma}_i C_i^\infty(1-k_i)/L/C_{ps} = O(1)$ (for $i = 1,2$), is $\lambda = O(\varepsilon)$ (single-solutal diffusive case) and $\lambda = O\left(\varepsilon^{3/2}\right)$ (double-solutal diffusive case). We denote these regimes (S-V) and (S-VI).Corresponding order of $\Delta T_{L,\mathrm{crit}}^B/L/C_{ps}$ is stated in Table 2 for each of these regimes. Regimes (V-S) and (VI-S) illustrate that the freezing of the ternary melt with finite values of the far-field concentrations and without occurrence of the supercooling is possible only if the melt is cooled very slowly. We note that in contrast to the regimes found in §2.4, regimes (S-V) and (S-VI) are not controlled by the specific diffusivity. Since λ is small in the regimes (S-V) and (S-VI), we are able to derive the following asymptotic expressions from eqn. (2.37).

$$\text{S-V:} \qquad \lambda \sim \frac{1}{\sqrt{\pi}r}\frac{\Delta T_{L,\mathrm{crit}}^B}{L/C_{ps}}\frac{L/C_{ps}}{\Gamma_1 C_1^\infty(1-k_1)\frac{1}{\mu}+\Gamma_2 C_2^\infty(1-k_2)\mu} \tag{2.61}$$

$$\text{S-VI:} \qquad \lambda \sim \frac{\mu}{\sqrt{\pi}r}\frac{\Delta T_{L,\mathrm{crit}}^B}{L/C_{ps}}\frac{L/C_{ps}}{\Gamma_1 C_1^\infty(1-k_1)} \tag{2.62}$$

In both regimes (S-V) and (S-VI) equations (2.33) and (2.34) implies $C_i^h \sim C_i^\infty$ (for $i = 1,2$) in the leading order.

Now we solve equations (2.6), (2.33)–(2.35) and (2.58) numerically to see how the behavior of water-like model system reflects the properties of the asymptotic cases stated in Table 2. We plot $\Delta T_{L,\mathrm{crit}}^B$ in the space of C_1^∞ and C_2^∞. Quantity $\Delta T_{L,\mathrm{crit}}^B$ quantifies how fast we can cool the ternary melt without occurrence of the supercooling. If $\Delta T_{L,\mathrm{crit}}^B$ is small it means that T_{crit}^B needs to be very close to the far-field temperature, for the supercooling not to occur. The opposite is true for the large $\Delta T_{L,\mathrm{crit}}^B$.

Figure 15(a) illustrates the onset of the supercooling for the water-like single diffusive case. We see, that if k_1 and k_2 are far from 1, melt needs to be cooled very slowly to avoid supercooling, except of the very small far-field concentrations. Disappearance of the supercooling for the large segregation coefficients is manifested in Figure 15(b). We see that

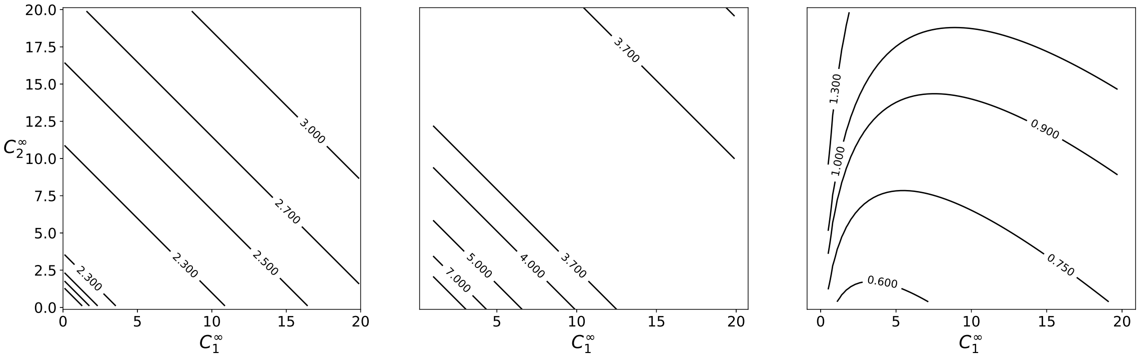

(a) (b) (c)

Figure 15: Difference between the far-field liquidus temperature and the critical bottom boundary temperature for which the undercooling occurs in the liquid region $\Delta T^B_{L,\mathrm{crit}}$ depicted in the space of the far-field solute concentrations. We see that in the single-solutal diffusive cases (a-b) $\varepsilon = 0.1$ and $\mu = 1$, we are able to cool the ternary melt from the temperature of the bottom boundary only 2–3 degrees lower than the far-field liquidus temperature if $k_1 = k_2 = 0$ (a). In case of the large segregation coefficients (b) $k_1 = k_2 = 0.7$ supercooling diminishes in agreement with the results stated in Table 2. The contour lines are strongly curved in the double-solutal diffusive case (c) $\varepsilon = 0.1$ and $\mu = \sqrt{\varepsilon}$ for wide ranges of C_1^∞ and C_2^∞. The rest of the material parameters are stated in Table 1 for the single and double-solutal diffusive model system, $T^\infty = 15°C$

supercooling tends to diminishes for $k_1 = 0.7$ and $k_2 = 0.7$, in agreement with the results stated in Table 2. Finally presence of the double-solutal diffusive effects is depicted in Figure 15(c). Difference in the solute diffusivities causes curvature of the contour lines of $\Delta T^B_{L,\mathrm{crit}}$ in the space of C_1^∞ and C_2^∞. Such behaviour is analogous to the undercooling analysed in [11] for the multicomponent system in the setup of directional solidification.

2.5 Discussion

We have investigated the solidification of a ternary system cooled from a fixed boundary. The model formulated in §2.2 is the extension of the model for the solidification of the binary alloy presented in [7]. Transport of heat and solutes in the model is governed by diffusion and fluid flow caused by the volume change during the phase change.

The asymptotic approach have revealed eight asymptotic regimes corresponding to the four different scalings of the dimensionless solidification rate with the inverse Lewis number, in the limit of large Lewis number. Regimes are divided into four groups according to the diffusivity, which controls the interface growth rate. Two regimes require order-one solutal diffusivities ratio and are similar to the regimes present in the binary model analyzed in [40] and [7]. Presence of the third solute leads to the novel regimes, not present in the binary case. These regimes requires solutal diffusivities ratio to be small or large for the very large Lewis numbers. It follows that if the difference between the value of the solutal diffusivities is large enough, there is regime in which smaller diffusivity is rate controlling as well as the regime where the larger diffusivity is rate controlling. Space of the far-field concentrations is divided into distinct regions, in which the solidification proceeds in one of these regimes. We have derived criteria for the transitional far-field solute concentrations, which marks transitions between the regimes.

In all regimes we have found the asymptotic expressions for the solute concentrations segregated at the interface, if possible. Of particular importance are the results for the segregation of ternary system with large (or small) solutal diffusivities ratio. We have found that segregation of the solute which diffusivity is rate controlling is qualitatively the same as it is in the binary system, while segregation of the other solute differs significantly. We have shown that in the regime controlled by larger diffusivity, concentration of the slower diffusing solute segregated at the interface is reaching its maximal value (given by the far-field concentration and segregation coefficient). In the regime controlled by the smaller diffusivity concentration of the faster diffusing solute segregated at the interface is close to its far-field value.

We have found that the shrinkage during the phase change enhances the solidification rate if the system solidifies in the regime controlled by the thermal diffusivity, but it slows down the solidification rate if the system solidifies in the regime controlled by one or two solutal diffusivities. The opposite have been shown to be true for the effect of the expansion.

In §2.4.5 we have analysed the effects of the non-zero segregation coefficients and the double-solutal diffusive effects on the onset of the supercooling in the liquid melt region. We have shown that for an order-one far-field solute concentrations, the dimensionless solidification rate is very small under the assumption of the undercooling not to occur.

3 Supercooled solidification

This section is based on our work Kyselica, Guba, Chudjak: Recalescence dynamics and solidification of a supercooled melt in a finite domain (under review). See Appendix C.

3.1 Dimensional formulation

We consider the solidification of a supercooled melt in a finite domain $0 < z < H$. Initially the whole domain is occupied by the liquid, uniformly supercooled to the temperature $T_i < T_m$ (see Fig. 16a)), where T_m is the equilibrium melting temperature. We assume that the solidification is initiated at $t = 0$. At later times the solid and liquid region are separated by the planar moving boundary $h = h(t)$ (see Fig. 16b)). We denote $T_s(z,t)$ and $T_l(z,t)$ the temperature fields in the solid and liquid phases, respectively. We consider fixed boundary conditions so that $T_s(0,t) = T_l(H,t) = T_i$. The temperature at the interface is $T_h(t) \equiv T(h(t),t)$. Since there is no solid at $t = 0$, we set $h(0) = 0$.

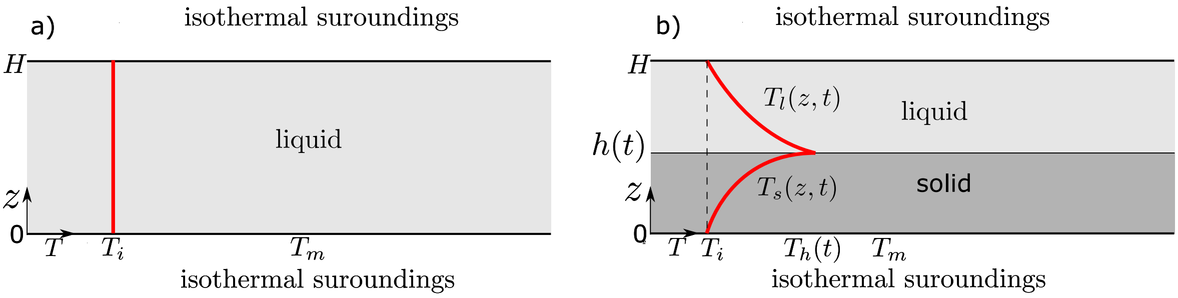

Figure 16: Schematic diagram of the supercooled solidifying system in the finite domain surrounded by the isothermal surroundings at a) initial time $t = 0$ and b) later time $t > 0$. Initially whole system is occupied by the supercooled liquid. At later times solid and liquid phases are separated by the planar boundary.

Transport of heat is governed by the heat diffusion only in both solid and liquid phases.

$$\frac{\partial T_s}{\partial t} = \kappa_s \frac{\partial^2 T_s}{\partial z^2} \qquad \text{and} \qquad \frac{\partial T_l}{\partial t} = \kappa_l \frac{\partial^2 T_l}{\partial z^2}, \tag{3.1}$$

where $\kappa_{s,l}$ are the heat diffusivities in the solid and liquid phases, respectively. The heat conservation at the interface is expressed by the Stefan condition

$$\rho L_{\text{eff}} \dot{h} = k_s \frac{\partial T}{\partial z}\bigg|_{h^-} - k_l \frac{\partial T}{\partial z}\bigg|_{h^+}, \tag{3.2}$$

where ρ is the density, $k_{s,l}$ are the thermal conductivities in the solid and liquid phases, respectively, and

$$L_{eff}(t) \equiv L_m - (C_{pl} - C_{ps})\,[T_m - T_h(t)] \tag{3.3}$$

is the effective latent heat, dependent on the local degree of supercooling. Here L_m is the latent heat of equilibrium solidification and $C_{ps,l}$ are the heat capacities of the respective phases. The effective latent heat represents an approximation of the latent heat of non-equilibrium solidification (see [29], [5], [6]).

As we are not interested in the volume-change effects upon solidification, we set the densities in both phases to be the same. We note that in case of $C_{ps} = C_{pl}$ effective latent heat reduces to the latent heat ($L_{\text{eff}} = L_m$). Since the supercooled solidification is an exothermic process, the rate of release of the effective latent heat must always be nonnegative, i.e. $L_{\text{eff}} \geq 0$ for all times. Consequently, since in real systems $C_{pl} > C_{ps}$, there is a maximum allowed value of the initial supercooling

$$\Delta T \equiv T_m - T_i \leq \Delta T_{max} \equiv \frac{L_m}{C_{pl} - C_{ps}}. \tag{3.4}$$

In deriving the inequality (3.4) we used that ΔT is the maximum value of $T_m - T_h(t)$. The solidification rate is determined by the attachment kinetics. For small supercoolings, such that $\Delta T/T_m \ll 1$, it is given by the following linear kinetic law

$$\dot{h} = G(T_m - T_h), \tag{3.5}$$

where G is the kinetic coefficient, calculated as in [28]

$$G = \frac{d}{6\hbar T_m}\frac{L_m w}{N_A}\exp(-q/k_B T_m), \tag{3.6}$$

where d is the molecular diameter, $\hbar$ the Planck constant, q the activation energy, k_B the Boltzmann constant, w the molecular weight and N_A the Avogadro constant. The values of material parameters for water, copper and salol are given in Table 3.

Since we have fixed-temperature boundary conditions with $T_i < T_m$, the only possible temperature distribution as $t \to \infty$, which would not be consistent with the finite extent of the liquid. Therefore we can define t_f, the time at which the system solidifies completely, as

$$h(t_f) = H. \tag{3.7}$$

The value of t_f is part of the solution.

Parameter	Water	Copper	Salol
$d/(\mathrm{m} \times 10^{-9})$	0.29	0.23	1
$q/(\mathrm{J} \times 10^{-20})$	3	6.71	6.61
$k_s/(\mathrm{W\ m^{-1}K^{-1}})$	2.25	401	0.34
$k_l/(\mathrm{W\ m^{-1}K^{-1}})$	0.56	157	0.18
$\rho/(\mathrm{kg\ m^{-3}} \times 10^3)$	1	8.02	1.18
$C_{ps}/(\mathrm{J\ kg^{-1}K^{-1}} \times 10^3)$	2.09	0.385	1.16
$C_{pl}/(\mathrm{J\ kg^{-1}K^{-1}} \times 10^3)$	4.22	0.53	1.58
$L_m/(\mathrm{J\ kg^{-1}} \times 10^5)$	3.34	2.09	0.9
T_m/K	273.15	1360	316
$\Delta T/\mathrm{K}$	5	50	5
$G/(\mathrm{m\ K^{-1}s^{-1}})$	9.3×10^{-4}	2.6×10^{-2}	6.6×10^{-6}

Table 3: Parameter values for water, copper and salol.

3.2 Dimensionless formulation

The present problem involves two independent set of scales. The length and time scales determined by the attachment kinetics, respectively, are

$$\ell_G = \frac{\kappa_l}{G^2 \Delta T^2} \qquad \text{and} \qquad \tau_G = \frac{\kappa_l}{G \Delta T}, \tag{3.8}$$

The second scaling is the thermal one, given by the finite extent of the region and the characteristic thermal diffusion time:

$$\ell_H = H \qquad \text{and} \qquad \tau_H = \frac{H^2}{\kappa_l} \tag{3.9}$$

Values of the scaling factors are given in Table 4 for water, cooper and salol. We see that kinetics scaling factors differs by a few orders from the thermal ones. Ratio of the thermal and the kinetic scaling factors is the following

$$\mathcal{G} \equiv \frac{\ell_H}{\ell_G} = \sqrt{\frac{\tau_H}{\tau_G}} = \frac{G \Delta T H}{\kappa_l}. \tag{3.10}$$

We call $\mathcal{G}$ the dimensionless kinetic coefficient.

Parameter	Water	Copper	Salol
τ_H/s	7.5×10^4	2.7×10^2	1.0×10^5
τ_G/s	6.1×10^{-3}	2.1×10^{-5}	87
k_{sl}	4.0	2.6	1.9
κ_{sl}	8.1	4.2	2.6
$\mathcal{G}$	3.5×10^3	3.6×10^3	34
$\mathscr{S}$	16	8	11
$\mathscr{S}_{\min}$	0.5	0.3	0.3

Table 4: Values of temporal scaling coefficients and the dimensionless material parameters for water, copper and salol. In order to calculate τ_H, $\mathcal{G}$ we set $H = 0.1$ m for all three materials. The values of the activation energy, q, for copper and salol are taken from [21] and that for water from [1]

Dimensionless temperature is defined as follows:

$$\theta = \frac{T - T_m}{\Delta T}. \tag{3.11}$$

Stefan number is defined as follows:

$$\mathscr{S} = \frac{L_m}{C_{pl}\Delta T}. \tag{3.12}$$

The inequality 3.4 gives the minimum physical value of Stefan number, $\mathscr{S}_{\min}$ such that

$$\mathscr{S}_{\min} \equiv \frac{L_m}{C_{pl}\Delta T_{\max}} = 1 - C_{\text{psl}}. \tag{3.13}$$

Since in this thesis we focus on the times of freezing when the finite domain effects are needed to be taken into account, we rewrite the equations (3.1) into the thermal scaling. Resulting equations are following

$$\frac{\partial \theta_s}{\partial t} = \kappa_s \frac{\partial^2 \theta_s}{\partial z^2} \qquad \text{and} \qquad \frac{\partial \theta_l}{\partial t} = \kappa_l \frac{\partial^2 \theta_l}{\partial z^2} \tag{3.14}$$

and the dimensionless boundary condition (3.2) transforms to

$$\left(\mathscr{S} + \mathscr{S}_{\min}\theta_h\right)\dot{h} = k_{s,l} \left.\frac{\partial \theta_s}{\partial z}\right|_{h^-} - \left.\frac{\partial \theta_l}{\partial z}\right|_{h^+}, \tag{3.15}$$

Linear kinetic law (3.5) expressed in the thermal scaling is

$$\mathcal{G}^{-1}\dot{h} = -\theta_h \tag{3.16}$$

Dimensionless initial and boundary condition conditions at the bottom and upper boundary are

$$t = 0: \qquad h = 0, \qquad \theta_l \equiv -1, \tag{3.17}$$

$$z = 0: \qquad \theta_s = -1, \tag{3.18}$$

$$z = 1: \qquad \theta_l = -1. \tag{3.19}$$

3.3 Front fixing transformation

Problem given by the equations (3.14)–(3.19) include moving boundary, which makes it troublesome for the numerical approach. In order to get rid of the moving boundary we apply the following front fixing transformation:

$$\xi \equiv \begin{cases} \frac{z}{h}, & \text{for} \quad 0 \le z \le h, \\ \frac{1-z}{1-h}, & \text{for} \quad h \le z \le 1, \end{cases}$$

Equations (3.14)–(3.19) then transform to the following form.

Solid: $\theta_s(\xi, t)$, $\xi = z/h(t)$

$$h^2 \frac{\partial \theta_s}{\partial t} = \xi h \dot{h} \frac{\partial \theta_s}{\partial \xi} + \kappa_{sl} \frac{\partial^2 \theta_s}{\partial \xi^2} \tag{3.20}$$

Liquid: $\theta_l(\xi, t)$, $\xi = (1 - z)/(1 - h(t))$

$$(1-h)^2 \frac{\partial \theta_l}{\partial t} = -\xi (1-h) \dot{h} \frac{\partial \theta_l}{\partial \xi} + \frac{\partial^2 \theta_l}{\partial \xi^2} \tag{3.21}$$

Equations (3.20) and (3.21) are subject to the following set of boundary conditions:

$$\dot{h} = -\mathcal{G}\theta_I, \quad \text{where} \quad \theta_I \equiv \theta_s(\xi = 1, t) \quad \text{or} \quad \theta_l(\xi = 1, t) \tag{3.22}$$

$$\theta_s(\xi = 0, t) = -1 \tag{3.23}$$

$$\theta_l(\xi = 0, t) = -1 \tag{3.24}$$

$$\theta_s(\xi = 1, t) = \theta_l(\zeta_l = 1, t) \tag{3.25}$$

$$(\mathscr{S} + \mathscr{S}_{\min}\theta_I)\dot{h} = \frac{k_{sl}}{h} \frac{\partial \theta_s}{\partial \xi}\bigg|_1 + \frac{1}{1-h} \frac{\partial \theta_l}{\partial \xi}\bigg|_1 \tag{3.26}$$

3.4 Numerical scheme

To solve system of equation (3.20) and (3.21) together with the boundary conditions (3.23)–(3.26) we implement the MacCormack's method (see [38]). We note that the MacCormack's method is second order accurate in space and time. Since MacCormack's method is a two step method, we present at first the equations for the evolution of the physical quantities to the auxiliary time denoted by asterisk.

At first $(\theta_s)^n_I$ is obtained as a larger root of the following quadratic equation

$$A\left(\theta_I^n\right)^2 + B\theta_I^n + C = 0, \tag{3.27}$$

with

$$\begin{aligned} A =& GS_{min} && (3.28)\\ B =& \frac{k_{sl}}{h^n}\frac{1}{\Delta\zeta_s} + \frac{1}{1-h^n}\frac{1}{\Delta\zeta_l} + GS && (3.29)\\ C =& -\left(\theta_s\right)^n_{I-1}\frac{k_{sl}}{h^n}\frac{1}{\Delta\zeta_s} - \left(\theta_l\right)^n_{I-1}\frac{1}{1-h^n}\frac{1}{\Delta\zeta_l} && (3.30) \end{aligned}$$

$$\left(\theta_s\right)^*_i = \left(\theta_s\right)^n_i + \overline{U}^n_{s,i}\left[\left(\theta_s\right)^n_{i+1} - \left(\theta_s\right)^n_i\right]\frac{\Delta t}{\delta\zeta_s} + \frac{K_{sl}\Delta t}{\Delta\zeta_s^2(h^n)^2}\left[\left(\theta_s\right)^n_{i+1} - 2\left(\theta_s\right)^n_i + \left(\theta_s\right)^n_{i-1}\right] \tag{3.31}$$

where $\overline{U}^n_{s,i}$ is defined as

$$\overline{U}^n_{s,i} = -\frac{G\theta^n_{s,I}}{2h^n}\left[\left(\zeta_s\right)_{i+1} + \left(\zeta_s\right)_i\right]. \tag{3.32}$$

$$\left(\theta_l\right)^*_i = \left(\theta_l\right)^n_i + \overline{U}^n_{l,i}\frac{\left(\theta_l\right)^n_{i+1} - \theta^n_i}{\Delta\zeta_l}\Delta t + \frac{\left(\theta_l\right)^n_{i+1} - 2\left(\theta_l\right)^n_i + \left(\theta_l\right)^n_{i-1}}{\Delta\zeta_l^2(1-h^n)^2}\Delta t \tag{3.33}$$

where $\overline{U}^n_{l,i}$ is defined as

$$\overline{U}^n_{l,i} = -\frac{G\theta^n_{s,I}}{1-h^n}\left[\left(\zeta_l\right)_{i+1} + \left(\zeta_s\right)_i\right]. \tag{3.34}$$

$$h^* = h^n - G\theta_I\Delta t. \tag{3.35}$$

Equations for the evolution of the quantities to the new time step $n+1$ are as follows. First $(\theta_s)^*_I$ is obtained as a larger root of the quadratic equation

$$A\left(\theta_I^*\right)^2 + B\theta_I^* + C = 0, \tag{3.36}$$

with

$$\begin{aligned} A =& GS_{min} && (3.37)\\ B =& \frac{k_{sl}}{h^*}\frac{1}{\Delta\zeta_s} + \frac{1}{1-h^*}\frac{1}{\Delta\zeta_l} + GS && (3.38)\\ C =& -\left(\theta_s\right)^*_{I-1}\frac{k_{sl}}{h^*}\frac{1}{\Delta\zeta_s} - \left(\theta_l\right)^*_{I-1}\frac{1}{1-h^*}\frac{1}{\Delta\zeta_l} && (3.39) \end{aligned}$$

$$(\theta_s)_i^{n+1} = (\theta_s)_i^n + \frac{1}{2}\Delta t \overline{U}^*_{s,i}\left[\frac{(\theta_s)^n_{i+1} - (\theta_s)^n_i}{\Delta\zeta} + \frac{(\theta_s)^*_{i+1} - (\theta_s)^*_i}{\Delta\zeta}\right] + \\ + \frac{K_{sl}}{(h^n)^2}\frac{(\theta_s)^*_{i+1} - (\theta_s)^*_i + (\theta_s)^*_{i-1}}{\Delta\zeta_s^2}\Delta t, \quad (3.40)$$

where $\overline{U}^*_{s,i}$ is defined as

$$\overline{U}^*_{s,i} = -\frac{G\theta^n_{s,I}}{2h^n}\left[(\zeta_s)_{i+1} + (\zeta_s)_i\right]. \quad (3.41)$$

$$(\theta_l)_i^{n+1} = (\theta_l)_i^n + \frac{1}{2}\overline{U}^*_{l,i}\left[\frac{(\theta_l)^n_{i+1} - (\theta_l)^n_i}{\Delta\zeta_l} + \frac{(\theta_l)^*_{i} - (\theta_l)^*_{i-1}}{\Delta\zeta_l}\right]\Delta t + \\ + \frac{(\theta_l)^*_{i+1} - 2\,(\theta_l)^*_i + (\theta_l)^*_{i-1}}{\Delta\zeta_l^2(1-h^n)^2}\Delta t \quad (3.42)$$

where $\overline{U}^*_{l,i}$ is defined as

$$\overline{U}^*_{l,i} = -\frac{G\theta^n_{l,I}}{2(1-h^n)}\left[(\zeta_l)_{i+1} + (\zeta_l)_i\right]. \quad (3.43)$$

We note that since the time denoted with asterisk is only auxiliary, interface position is evolved only once. Formally we write

$$h^{n+1} = h^*. \quad (3.44)$$

We implemented the introduced numerical scheme in `Python`. The core of the code is listed in the Appendix B.

3.5 Results

3.5.1 Asymptotic results

By the method of the matching asymptotic expansion, leading-order asymptotic solutions $\mathscr{S} \to \infty$ for θ_h and h can be derived in the following form:

$$\theta_h \sim -\left(\frac{2\mathcal{G}^2\mathscr{S}t}{k_{\mathrm{sl}}} + 1\right)^{-1/2}, \quad (3.45)$$

$$h \sim \frac{k_{\mathrm{sl}}}{\mathcal{G}\mathscr{S}}\left[\left(\frac{2\mathcal{G}^2\mathscr{S}t}{k_{\mathrm{sl}}} + 1\right)^{1/2} - 1\right]. \quad (3.46)$$

At the times $t = \mathscr{S}\bar{t}$, with $\bar{t} = O(1)$ as $\mathscr{S} \to \infty$, Stefan condition at the leading order yields

$$\frac{dh}{d\bar{t}} = \frac{k_{\mathrm{sl}}}{h} + \frac{1}{1-h}. \quad (3.47)$$

By integrating the equation (3.47), we get

$$\bar{t} = \frac{k_{\mathrm{sl}}}{(k_{\mathrm{sl}}-1)^3}\ln\left|\left(1 - \frac{1}{k_{\mathrm{sl}}}\right)h - 1\right| + \frac{1}{2}\frac{h^2}{k_{\mathrm{sl}}-1} + \frac{h}{(k_{\mathrm{sl}}-1)^2}, \quad (3.48)$$

for $k_{\text{sl}} \neq 1$ and

$$\frac{1}{2}h^2 - \frac{1}{3}h^3 = \bar{t} \tag{3.49}$$

for $k_{sl} = 1$. We note that h is continuous in $k_{\text{sl}} = 1$. Equation (3.48) ((3.49)) needs to be solved numerically for $h\left(\bar{t}\right)$. On the other hand, it is possible to obtain the explicit formula for the time of complete freezing $\bar{t}_f$. Since $h\left(\bar{t}_f\right) = 1$

$$\bar{t}_f = \frac{k_{\text{sl}}^2 - 2k_{\text{sl}}\ln k_{\text{sl}} - 1}{2(k_{\text{sl}} - 1)^3}. \tag{3.50}$$

Relation (3.50) is continuous in $k_{\text{sl}} = 1$, $\bar{t}_f(k_{\text{sl}} = 1) = 1/6$.

Since $t = \mathscr{S}\bar{t}$,

$$t_f = \mathscr{S}\bar{t}_f \quad \text{as} \quad \mathscr{S} \to \infty. \tag{3.51}$$

By substituting (3.47) into (3.16) we get θ_h as a function of h. Requiring $\theta_h' = 0$ we find that θ_h acquires a maximum at h^* given by the equation

$$h^* = k_{\text{sl}}^{1/2} / \left(1 + k_{\text{sl}}^{1/2}\right), \tag{3.52}$$

and the value of the maximal dimensionless temperature is

$$\theta_h^* \sim -(1 + k_{\text{sl}}^{1/2})^2 / \mathcal{G}\mathscr{S} \quad \text{as} \quad \mathscr{S} \to \infty. \tag{3.53}$$

We denote $\bar{t}^*$ the scaled time at which $\theta_h\left(\bar{t}^*\right) = \theta_h^*$. Moreover, since $\dot{\theta}_h\left(\bar{t}^*\right)$, the kinetic law (3.16) implies $\ddot{h}\left(\bar{t}^*\right) = 0$. Hence the Taylor approximation near $\bar{t} = \bar{t}^*$ of the leading-order interface is

$$h\left(\bar{t}\right) \sim h^* + \left(1 + k_{\text{sl}}^{1/2}\right)^2 (\bar{t} - \bar{t}^*) + O\left[(\bar{t} - \bar{t}^*)^3\right] \quad \text{as} \quad \mathscr{S} \to \infty. \tag{3.54}$$

Plugging the Taylor expansion (3.54) into the Stefan condition yields

$$\theta_h\left(\bar{t}\right) \sim -\frac{\left(1 + k_{\text{sl}}^{1/2}\right)^2}{\mathcal{G}\mathscr{S}} \left[1 + \frac{\left(1 + k_{\text{sl}}^{1/2}\right)^6}{3k_{\text{sl}}^{1/2}} (\bar{t} - \bar{t}^*)^2\right] \quad \text{as} \quad \mathscr{S} \to \infty. \tag{3.55}$$

Finally, for the speed of the interface we get

$$\dot{h} \approx (1 + k_{\text{sl}}^{1/2}) / \mathscr{S}. \tag{3.56}$$

3.5.2 Comparison of the asymptotic and numerical results

Evolution of the interface temperature and position is depicted in Figure 17. Numerical results suggest that there are three qualitatively different stages of solidification. During the initial stage, attachment kinetics dominates. Interface temperature rises quickly to the values close to the equilibrium melting temperature and the growth is nonlinear in time. After a transition time system transfer to the quasi-steady stage, where the growth is mostly influenced by the latent heat release. The interface temperature is changing weakly in time and solid grows linearly in time. In the late stage, when interface approaches the upper boundary of the system, the finite-domain effects dominate. The interface temperature decreases quickly and the growth rate increases.

In Figure 18 we plot the solutions for the interface temperature and the interface position zoomed to the time t^*. We see that numerical solutions match the asymptotic expansions (3.54) and (3.55) well. The agreement between the numerical and asymptotic results for θ_h^* is displayed in Figure 19. Numerical results for the time of total freezing were obtained by simulating the freezing process with the interface position initialized at $h(t = 0) = 0.01$. The simulation was stopped when the interface position reached the value $h = 0.99$. We derived the asymptotic results in the limit of large Stefan number, but we see that the asymptotic results match the numerical solutions also for $\mathscr{S} \approx 10$, and therefore describe well the solidification of the substances such as salol, water and cooper. Finally, the comparison between the numerical and the asymptotic results for the interface velocity around the time t^* is shown in Figure 21.

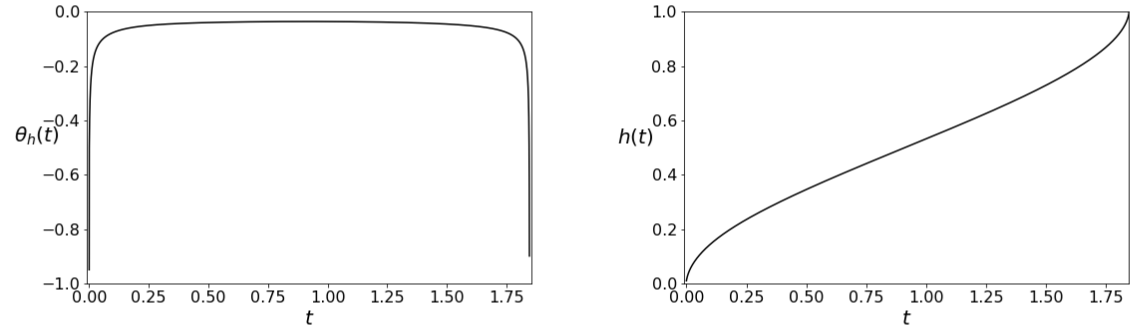

(a) (b)

Figure 17: Evolution of the interface temperature $\theta(t)$ and position $h(t)$ in time. Numerical constants are $\mathscr{S} = 10$, $\mathcal{G} = 10$, $\mathscr{S}_{\min} = 0$, $k_{sl} = 1$ and $K_{sl} = 1$.

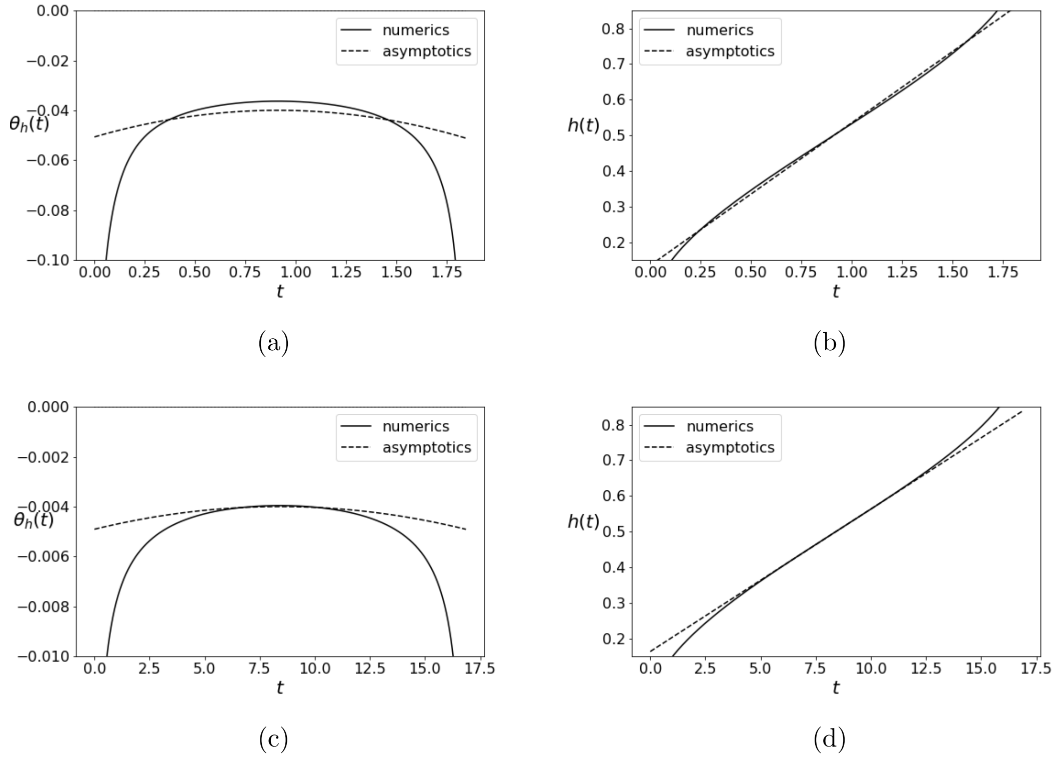

(a) (b)

(c) (d)

Figure 18: A close up view of the evolution of the interface temperature $\theta(t)$ and position $h(t)$ around the time t^*. Solid curve is the numerical solution and dashed curves are asymptotic expansions given by (3.54) and (3.55). Numerical constants are (a-b) $\mathscr{S} = 10$, (c-d) $\mathscr{S} = 100$ and in all plots $\mathcal{G} = 10$, $\mathscr{S}_{\min} = 0$, $k_{sl} = 1$ and $K_{sl} = 1$.

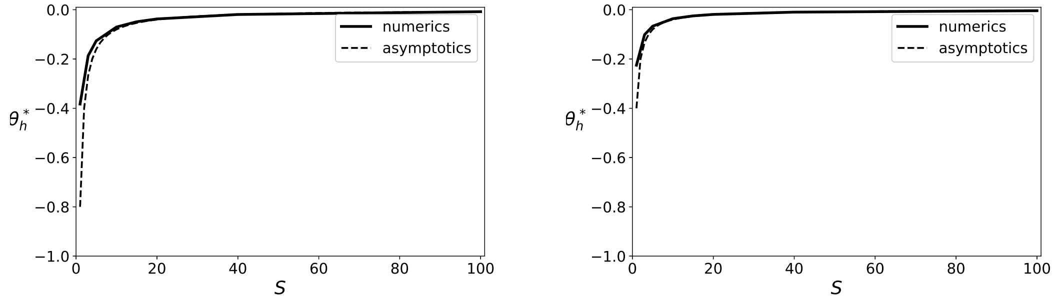

(a) (b)

Figure 19: Maximal interface temperature which system attains during the solidification process as a function of dimensional parameter $\mathscr{S}$. Parameters used to plot numerical results (points) are a) $\mathcal{G} = 5$ and b) $\mathcal{G} = 10$, $\mathscr{S}_{\min} = 0$, $k_{sl} = 1$ and $K_{sl} = 1$ in both plots. Dashed curves are plotted according to the asymptotic formula (3.53).

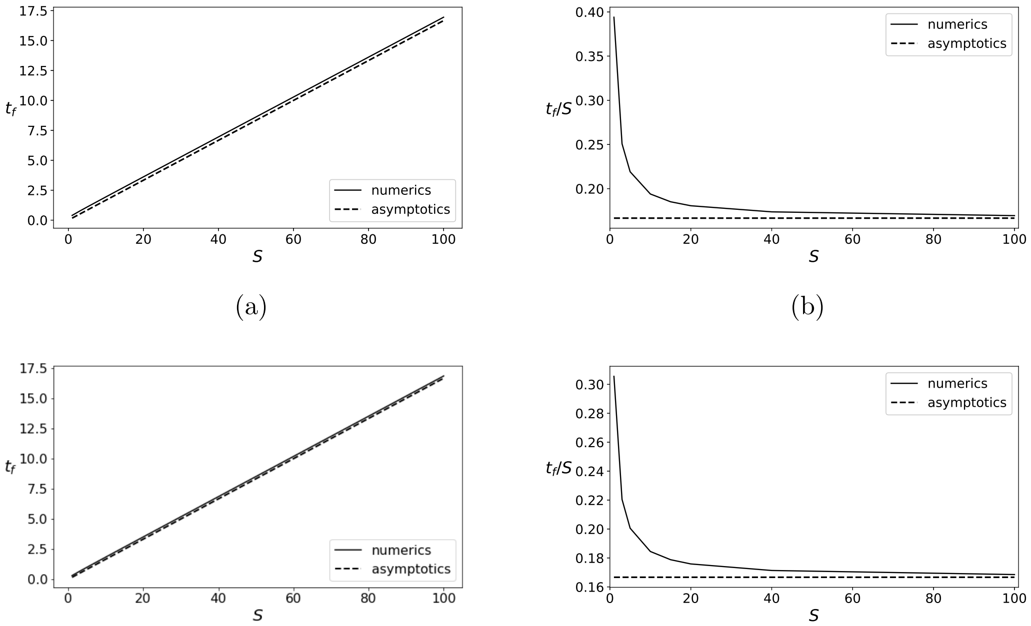

(a) (b)

(c) (d)

Figure 20: Time of freezing t_f as a function of dimensionless parameter $\mathscr{S}$. Parameters used to plot numerical results (solid curve) are (a-b) $\mathcal{G} = 5$ and (c-d) $\mathcal{G} = 10$, $\mathscr{S}_{\min} = 0$, $k_{sl} = 1$ and $K_{sl} = 1$ in both plots. Asymptotic solutions (dashed curves) are plotted according to (3.50).

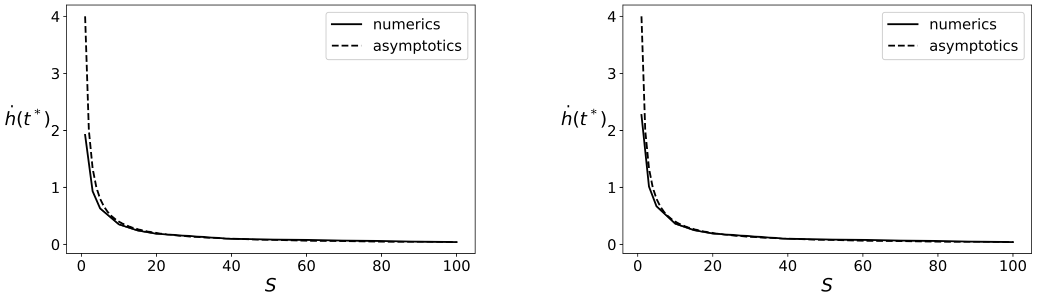

(a) (b)

Figure 21: Interface velocity at the time of maximal interface temperature as a function of dimensionless parameter $\mathscr{S}$. Parameters used to plot numerical results (points) are a) $\mathcal{G} = 5$ and b) $\mathcal{G} = 10$, $\mathscr{S}_{\min} = 0$, $k_{sl} = 1$ and $K_{sl} = 1$ in both plots. Dashed curve is plotted according to the asymptotic formula (3.56).

4 Conclusions

In this thesis, we introduce three problems involving phase change and flow of multiphase systems. First is the asymmetric mode of a Taylor bubble moving in the vertical pipe under against the downward flow, second is a solidification of a ternary alloy in the semi-infinite domain cooled from the bottom boundary and third is a solidification of supercooled liquids in a finite domain.

In §1 we have reconstructed the shape of the fast asymmetric elongated air bubbles in the vertical pipe under the presence of the downward fluid flow. The experiments have been performed using an experimental facility at the School of Mechanical Engineering of the Tel-Aviv University, developed and described by [19] to study the dynamics of Taylor bubbles in external fluid flows. To produce the fast asymmetric elongated bubbles, the downward fluid flow has been triggered after the bubble had reached a steady rise in otherwise stagnant fluid.

To justify the precision of our laser method, we have determined a shape which would be observed if viewed from the side based on the laser measurements. Consequently, we have compared the shape to that obtained from the side-view image, and found a good agreement. We have also calculated volumes of the bubbles in the asymmetric mode. Calculated values have showed good agreement with the volumes of the bubbles in the symmetric mode, produced during the same injection time.

Laser measurements reveal that the bubble cross section through the plane perpendicular to the pipe axis is not concave, but there is a depression in the bubble shape reflecting the strongest flow in the middle of the pipe. Despite the fact that the velocity of the asymmetric bubble does not depend on the velocity of downward fluid flow, we have found a dependence of the bubble shape on the flow velocity. The asymmetric bubble becomes more tapered as the flow rate increases.

A simple inviscid model to predict the bubble shape has been proposed. Predicted bubble shapes are in qualitative agreement with our experimental findings.

In §2 we have modeled the solidification of the ternary system cooled from the rigid boundary in the one dimensional half-space. Flow present in the model is due to the expansion or shrinkage upon the phase change. Transport of heat is governed by the convection-diffusion equation. We have derived analytic form of the solutions for the temperature field, two solutal fields, interface position, and the flow field, up to the four constants, which are determined by the set of the transcendental system of equation. By analyzing the system of transcendental equations in the limit of small Lewis numbers we have identified eight asymptotic regimes. Solidification proceeds in one of these regimes, depending on the material and experimental parameters. We have also identified the material and experimental parameters for which these regimes occur. We have found asymptotic expressions for the amount of each solute segregated at the interface. It has been shown that the effect of the flow has enhancing or reducing the effect on the solidification rate, depending on the asymptotic regime in which the solidification proceeds. In the last part of §2 we have analyzed marginal constitutional supercooling. Our numerical results have shown that undercooling is stronger influenced by the slower diffusing solute, rather than the faster diffusing solute.

In §3 we have modeled solidification of one-dimensional supercooled liquid in a finite domain. Heat transport has been modeled by the diffusion equation in both solid and liquid phases. Direct numerical simulation of the model reveals different stages of freezing dynamics: the initial stage dominated by the interfacial attachment kinetics, the intermediate quasi–equilibrium stage, and the late stage dominated by the finite-domain effects. The case of large latent heat release upon solidification and small undercooling, which corresponds to the large Stefan number and is typical to the large variety of materials, has been studied. We have presented the asymptotic solutions for the total time of freezing, interface position, interface temperature and maximal interface temperature which system attains during the freezing, in the limit of large Stefan number. Comparing asymptotic solutions to the numerical results have shown good agreement with numerical results, even for the realistic values of Stefan number, similar to the Stefan number typical for Salol.

References

[1] D. Barahona. Thermodynamic derivation of the energy of activation for ice nucleation. *Atmos. Chem. Phys.*, 15(13), 2015.

[2] G. K. Batchelor, H. K. Moffatt, and M. G. Worster. *Perspectives in fluid dynamics: a collective introduction to current research.* Cambridge University Press, 2002.

[3] J. D. Bugg and G. A. Saad. The velocity field around a taylor bubble rising in a stagnant viscous fluid: numerical and experimental results. *Int. J. Multiphas. Flow*, 28(5):791–803, 2002.

[4] J. Canny. A computational approach to edge detection. *IEEE Transactions on pattern analysis and machine intelligence*, (6):679–698, 1986.

[5] Ch. Charach and B. Zaltzman. Planar solidification from an undercooled melt: Asymptotic solutions to a continuum model with interfacial kinetics. *Phys. Rev. E*, 47(2):1230, 1993.

[6] Ch. Charach and A. Zemel. Irreversible thermodynamics of phase change heat transfer: basic principles and applications to latent heat storage. *Open Syst. Inf. Dyn.*, 1(3):423–458, 1992.

[7] A. O. P. Chiareli, H. E. Huppert, and M. G. Worster. Segregation and flow during the solidification of alloys. *J. Cryst. Growth*, 139(1-2):134–146, 1994.

[8] M. Chudjak, A. Fershtman, D. Barnea, L. Shemer, and P. Guba. Reconstruction of the shape of asymmetric elongated bubbles moving in downward liquid flows. Poster presentation at 17th Multiphase Flow Conference & Short Course, November 11-15, 2019, Dresden.

[9] R. Clift, J. R. Grace, and M. E. Weber. *Bubbles, drops, and particles.* Courier Corporation, 2005.

[10] R. Collins, F. F. De Moraes, J. F. Davidson, and D. Harrison. The motion of a large gas bubble rising through liquid flowing in a tube. *J. Fluid Mech.*, 89(3):497–514, 1978.

[11] S. R. Coriell, G. B. McFadden, P. W. Voorhees, and R. F. Sekerka. Stability of a planar interface during solidification of a multicomponent system. *J. Cryst. Growth*, 82(3):295–302, 1987.

[12] A. K. Dahle and D. H. StJohn. Rheological behaviour of the mushy zone and its effect on the formation of casting defects during solidification. *Acta. Mater.*, 47(1):31–41, 1998.

[13] R. M. Davies and G. I. Taylor. The mechanics of large bubbles rising through extended liquids and through liquids in tubes. *Proc. R. Soc. London, Ser. A*, 200(1062):375–390, 1950.

[14] S. H. Davis. *Theory of solidification.* Cambridge University Press, 2001.

[15] S. Deville. The lure of ice-templating: recent trends and opportunities for porous materials. *Scripta Mater.*, 2017.

[16] D. T. Dumitrescu. Strömung an einer luftblase im senkrechten rohr. *ZAMM-Journal of Applied Mathematics and Mechanics/Zeitschrift für Angewandte Mathematik und Mechanik*, 23(3):139–149, 1943.

[17] J. Fabre and B. Figueroa-Espinoza. Taylor bubble rising in a vertical pipe against laminar or turbulent downward flow: symmetric to asymmetric shape transition. *J. Fluid Mech.*, 755:485–502, 2014.

[18] S. D. Felicelli, D. R. Poirier, and J. C. Heinrich. Macrosegregation patterns in multicomponent ni-base alloys. *J. Cryst. Growth*, 177(1-2):145–161, 1997.

[19] A. Fershtman, V. Babin, D. Barnea, and L. Shemer. On shapes and motion of an elongated bubble in downward liquid pipe flow. *Phys. Fluids*, 29(11):112103, 2017.

[20] B. Figueroa-Espinoza and J. Fabre. Taylor bubble moving in a flowing liquid in vertical channel: transition from symmetric to asymmetric shape. *J. Fluid Mech.*, 679:432–454, 2011.

[21] F. Font, S. L. Mitchell, and T. G. Myers. One-dimensional solidification of supercooled melts. *Int. J. Heat Mass Transfer*, 62:411–421, 2013.

[22] P. Griffith and G. B. Wallis. Two-phase slug flow. *J. Heat Transf.*, 83(3), 1961.

[23] P. Guba and D. M. Anderson. Diffusive and phase change instabilities in a ternary mushy layer. *J. Fluid Mech.*, 760:634–669, 2014.

[24] P. Guba and D. M. Anderson. Pattern selection in ternary mushy layers. *J. Fluid Mech.*, 825:853–886, 2017.

[25] M. G. Hennessy, M. C. Schwarzwälder, and T. G. Myers. Asymptotic analysis of the guyer–krumhansl–stefan model for nanoscale solidification. *Appl. Math. Modell.*, 61:1–17, 2018.

[26] M. G. Hennessy, M. C. Schwarzwälder, and T. G. Myers. Modelling ultra-fast nanoparticle melting with the maxwell–cattaneo equation. *Appl. Math. Modell.*, 69:201–222, 2019.

[27] H. E. Huppert and M. G. Worster. Dynamic solidification of a binary melt. *Nature*, 314(6013):703, 1985.

[28] D. R. H. Jones and M. F. Ashby. *Engineering materials 2: an introduction to microstructures, processing and design.* Elsevier, 2005.

[29] A. Kostinski and W. Cantrell. Entropic aspects of supercooled droplet freezing. *J. Atmos. Sci.*, 65(9):2961–2971, 2008.

[30] J. Kyselica and P. Guba. Forced flow and solidification over a moving substrate. *Appl. Math. Modell.*, 40(1):31–40, 2016.

[31] J. Kyselica, P. Guba, and M. Hurban. Solidification and flow of a binary alloy over a moving substrate. *Transp. Porous Media*, pages 1–17, 2017.

[32] X. Lu and A. Prosperetti. Axial stability of taylor bubbles. *J. Fluid Mech.*, 568:173–192, 2006.

[33] X. Lu and A. Prosperetti. A numerical study of taylor bubbles. *Ind. Eng. Chem. Res.*, 48(1):242–252, 2008.

[34] Zai-Sha Mao and A. E. Dukler. The motion of taylor bubbles in vertical tubes. i. a numerical simulation for the shape and rise velocity of taylor bubbles in stagnant and flowing liquid. *J. Comput. Phys.*, 91(1):132–160, 1990.

[35] C. S. Martin. Vertically downward two-phase slug flow. *J. Fluid. Eng.*, 98(4):715–722, 1976.

[36] D. Nicklin. Two-phase bubble flow. *Chem. Eng. Sci.*, 17(9):693–702, 1962.

[37] S. Polonsky, L. Shemer, and D. Barnea. The relation between the taylor bubble motion and the velocity field ahead of it. *Int. J. Multiphase Flow*, 25(6-7):957–975, 1999.

[38] C. Pozrikidis. *Introduction to theoretical and computational fluid dynamics.* Oxford university press, 2011.

[39] L. Shemer. Hydrodynamic and statistical parameters of slug flow. *Int. J. Heat Fluid Flow*, 24(3):334–344, 2003.

[40] M. G. Worster. Solidification of an alloy from a cooled boundary. *J. Fluid Mech.*, 167:481—501, 1986.

A Appendix

M. Chudjak, A. Fershtman, D. Barnea, L. Shemer, P. Guba, Reconstruction of the shape of asymmetric elongated bubbles moving in downward liquid flows. Poster presentation at 17th Multiphase Flow Conference & Short Course, November 11-15, 2019, Dresden.

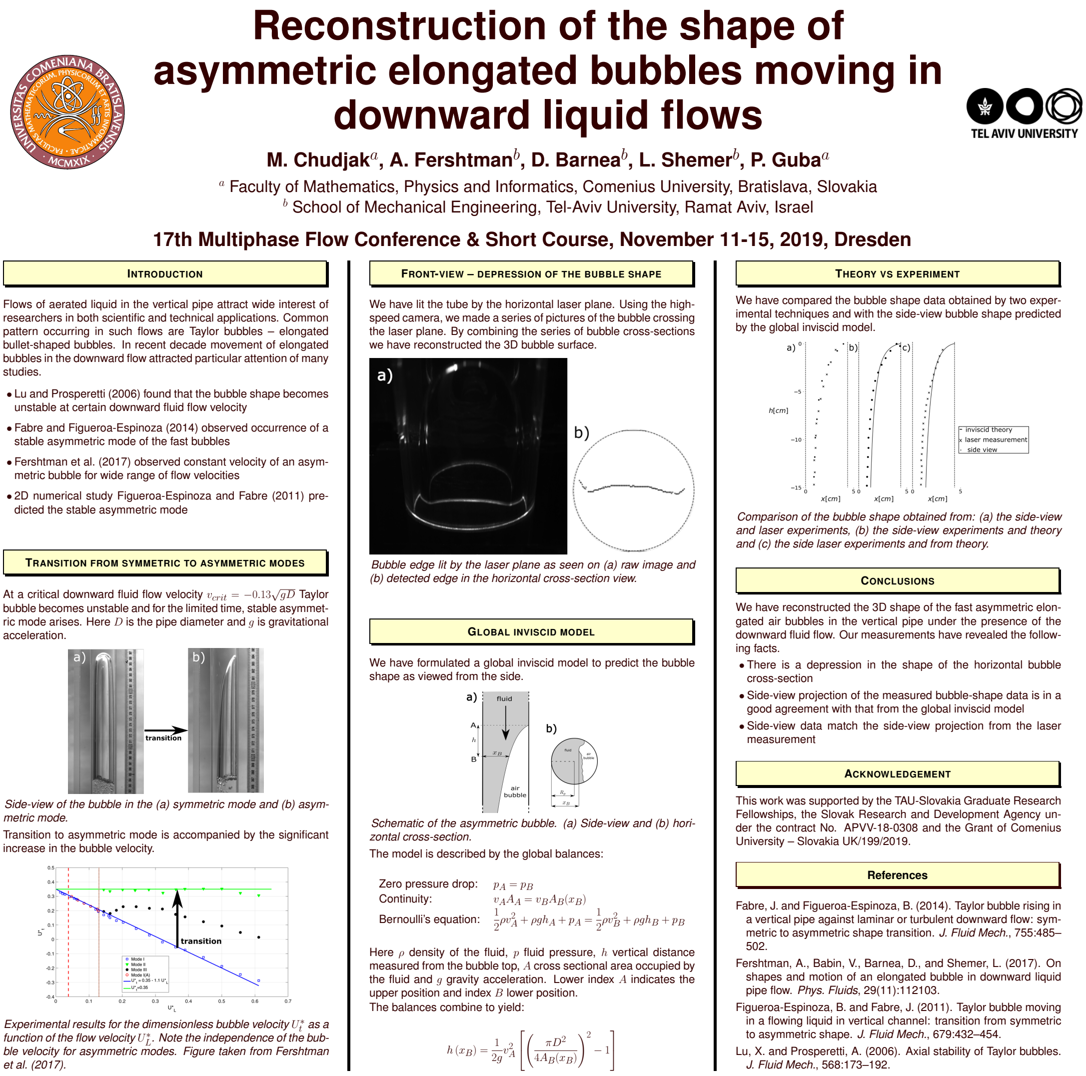

Reconstruction of the shape of asymmetric elongated bubbles moving in downward liquid flows

M. Chudjak[a], **A. Fershtman**[b], **D. Barnea**[b], **L. Shemer**[b], **P. Guba**[a]
[a] Faculty of Mathematics, Physics and Informatics, Comenius University, Bratislava, Slovakia
[b] School of Mechanical Engineering, Tel-Aviv University, Ramat Aviv, Israel

17th Multiphase Flow Conference & Short Course, November 11-15, 2019, Dresden

INTRODUCTION

Flows of aerated liquid in the vertical pipe attract wide interest of researchers in both scientific and technical applications. Common pattern occurring in such flows are Taylor bubbles – elongated bullet-shaped bubbles. In recent decade movement of elongated bubbles in the downward flow attracted particular attention of many studies.

- Lu and Prosperetti (2006) found that the bubble shape becomes unstable at certain downward fluid flow velocity
- Fabre and Figueroa-Espinoza (2014) observed occurrence of a stable asymmetric mode of the fast bubbles
- Fershtman et al. (2017) observed constant velocity of an asymmetric bubble for wide range of flow velocities
- 2D numerical study Figueroa-Espinoza and Fabre (2011) predicted the stable asymmetric mode

TRANSITION FROM SYMMETRIC TO ASYMMETRIC MODES

At a critical downward fluid flow velocity $v_{crit} = -0.13\sqrt{gD}$ Taylor bubble becomes unstable and for the limited time, stable asymmetric mode arises. Here D is the pipe diameter and g is gravitational acceleration.

Side-view of the bubble in the (a) symmetric mode and (b) asymmetric mode.

Transition to asymmetric mode is accompanied by the significant increase in the bubble velocity.

Experimental results for the dimensionless bubble velocity U_t^* as a function of the flow velocity U_L^*. Note the independence of the bubble velocity for asymmetric modes. Figure taken from Fershtman et al. (2017).

FRONT-VIEW – DEPRESSION OF THE BUBBLE SHAPE

We have lit the tube by the horizontal laser plane. Using the high-speed camera, we made a series of pictures of the bubble crossing the laser plane. By combining the series of bubble cross-sections we have reconstructed the 3D bubble surface.

Bubble edge lit by the laser plane as seen on (a) raw image and (b) detected edge in the horizontal cross-section view.

GLOBAL INVISCID MODEL

We have formulated a global inviscid model to predict the bubble shape as viewed from the side.

Schematic of the asymmetric bubble. (a) Side-view and (b) horizontal cross-section.

The model is described by the global balances:

Zero pressure drop: $p_A = p_B$
Continuity: $v_A A_A = v_B A_B(x_B)$
Bernoulli's equation: $\frac{1}{2}\rho v_A^2 + \rho g h_A + p_A = \frac{1}{2}\rho v_B^2 + \rho g h_B + p_B$

Here ρ density of the fluid, p fluid pressure, h vertical distance measured from the bubble top, A cross sectional area occupied by the fluid and g gravity acceleration. Lower index A indicates the upper position and index B lower position.
The balances combine to yield:

$$h\left(x_B\right) = \frac{1}{2g} v_A^2 \left[\left(\frac{\pi D^2}{4A_B(x_B)} \right)^2 - 1 \right]$$

THEORY VS EXPERIMENT

We have compared the bubble shape data obtained by two experimental techniques and with the side-view bubble shape predicted by the global inviscid model.

Comparison of the bubble shape obtained from: (a) the side-view and laser experiments, (b) the side-view experiments and theory and (c) the side laser experiments and from theory.

CONCLUSIONS

We have reconstructed the 3D shape of the fast asymmetric elongated air bubbles in the vertical pipe under the presence of the downward fluid flow. Our measurements have revealed the following facts.

- There is a depression in the shape of the horizontal bubble cross-section
- Side-view projection of the measured bubble-shape data is in a good agreement with that from the global inviscid model
- Side-view data match the side-view projection from the laser measurement

ACKNOWLEDGEMENT

This work was supported by the TAU-Slovakia Graduate Research Fellowships, the Slovak Research and Development Agency under the contract No. APVV-18-0308 and the Grant of Comenius University – Slovakia UK/199/2019.

References

Fabre, J. and Figueroa-Espinoza, B. (2014). Taylor bubble rising in a vertical pipe against laminar or turbulent downward flow: symmetric to asymmetric shape transition. *J. Fluid Mech.*, 755:485–502.

Fershtman, A., Babin, V., Barnea, D., and Shemer, L. (2017). On shapes and motion of an elongated bubble in downward liquid pipe flow. *Phys. Fluids*, 29(11):112103.

Figueroa-Espinoza, B. and Fabre, J. (2011). Taylor bubble moving in a flowing liquid in vertical channel: transition from symmetric to asymmetric shape. *J. Fluid Mech.*, 679:432–454.

Lu, X. and Prosperetti, A. (2006). Axial stability of Taylor bubbles. *J. Fluid Mech.*, 568:173–192.

B Appendix

```
while (t_i < Nt_max) and (h_new < h_max):
    delta_t = get_delta_t(delta_x_l, delta_x_l, h_old, U_s, ip)
    t_range[t_i] = get_new_time(t_range, t_i, delta_t)

    # Evolution to: t_star
    ts_old[i_smax] = get_t_I(h_old, delta_x_s, delta_x_l, \
                        ts_old[i_smax-1], tl_old[i_smax-1], ip)
    tl_old[i_smax] = ts_old[i_smax]
    U_s = -x_s*ip['G']*ts_old[i_smax]/h_old
    U_l = -x_l*ip['G']*tl_old[i_smax]/(1-h_old)
    ts_star = evolve_ts_star(ts_star, ts_old, U_s, delta_t,\
                    delta_x_s, h_old, Nx, ip)
    tl_star = evolve_tl_star(tl_star, tl_old, U_l, delta_t,\
                    delta_x_l, h_old, Nx, ip)
    h_star = h_old - ip['G']*ts_old[i_smax]*delta_t
    ts_star[i_smax] = get_t_I(h_star, delta_x_s, delta_x_l,\
                        ts_star[i_smax-1], tl_star[i_smax-1], ip)
    tl_star[i_smax] = ts_star[i_smax]

    # Evolution to: t_n+1
    U_s_star = -x_s*ip['G']*ts_star[i_smax]/h_star
    U_l_star = -x_l*ip['G']*tl_star[i_smax]/(1-h_star)
    ts_new = evolve_ts(ts_new, ts_old, ts_star, delta_t,\
                   delta_x_s, U_s_star, h_star, Nx)
    tl_new = evolve_tl(tl_new, tl_old, tl_star, delta_t,\
                   delta_x_l, U_l_star, h_star, Nx)
    # Interface is updated only once in a time step
    h_new = h_star
    ts_new[i_smax] = ts_star[i_smax]
    tl_new[i_smax] = ts_star[i_smax]

    ts_plt, tl_plt, h_t, t_i_t, h_plt =\
```

```
        store_data_for_ploting(h_new, h_plt, h_max, h_init,\
                               t_i, ts_star, ts_new, tl_new,\
                               ts_plt, tl_plt, h_t, t_i_t,\
                               i_smax, printing=test_print)

    # Upgrade old variable to the new one
    ts_old, tl_old, h_old = ts_new, tl_new, h_new
    t_i += 1
    chcek_cfl(U_s, t_i, ts_new, h_new, delta_t, delta_x_s, ip)
```

Listing 1: The core part of the `Python` implementation of the numerical scheme given by the equations (3.27)–(3.44).

C Appendix

Recalescence dynamics and solidification of a supercooled melt in a finite domain

Juraj Kyselica[a,*], Peter Guba[b,c], Martin Chudjak[b]

[a] *Institute of Geophysics, The Czech Academy of Sciences, 141 31 Prague 4, Czech Republic*
[b] *Department of Applied Mathematics and Statistics, Faculty of Mathematics, Physics and Informatics, Comenius University, 842 48 Bratislava 4, Slovakia*
[c] *Earth Science Institute of the Slovak Academy of Sciences, 840 05 Bratislava 4, Slovakia*

Abstract

We study the dynamics of supercooled solidification of a pure material in a finite domain subject to isothermal boundary conditions. At early stages when the liquid can effectively be treated as semi-infinite, we derive asymptotic solutions in the limits of both strong and weak latent-heat release, corresponding to large and small effective Stefan numbers, respectively. In particular, the solutions describing a rapid recalescence followed by a gradual change in the interfacial temperature are derived. Once the finite extent becomes effective, the system relaxes to an intermediate stage. For large Stefan numbers, the intermediate stage is quasi-steady, with the linear temperature profiles in the two phases and the interface temperature close to an equilibrium melting temperature. For Stefan numbers less than unity, the intermediate stage has a traveling-wave temperature profile in the liquid, similar to that in the one-sided problem, and a self-similar profile in the solid, where the temperature is close to the interface temperature through the whole solid except for a thermal boundary layer far from the interface.

Keywords: Two-sided Stefan problem, Kinetic supercooling, Recalescence, Latent heat, Matched asymptotic expansions, Finite domain

---

1. Introduction

Many liquids can be cooled below their equilibrium melting temperature without actually solidifying. Such phenomenon is called supercooling. Solidification of a supercooled liquid can be triggered by various mechanisms, e.g. by the presence of some impurity, as in clouds (Hobbs [1]), by the impact of supercooled droplets (Schremb et al. [2]) or just by tapping the supercooled water in a bottle. From a thermodynamic point of view, the supercooled solidification is a process during which the system moves irreversibly from a metastable state

---

[*] Corresponding author
Email address: `kyselica@ig.cas.cz` (Juraj Kyselica)

Preprint submitted to International Journal of Heat and Mass Transfer February 10, 2020

to a stable one (Ashby [3]; Kostinski & Cantrel [4]). The solidification rate is a function of local supercooling and is determined by a difference between the rates of attachment and detachment of molecules of the liquid phase to or from the solid phase (Ashby [3]). The term kinetic supercooling is usually used to describe this situation.

The simplest model of kinetically-supercooled solidification is the one-sided Stefan problem with a semi-infinite liquid (Davis [5]). The term one-sided refers to the fact that only the thermal field in the liquid is evolved, while that in the solid is constant. The one-sided model is widely used in literature, and although it cannot be solved explicitly, its treatment is less challenging than that of the two-sided model. However, as pointed out by Evans & King [6], the standard one-sided model does not conserve energy. They derived a modified, energy conserving one-sided reduction of the two-sided model with thermally insulated solid in the limit when the ratio of the heat conductivities in the solid and liquid is small. Myers et al. [7] derived a consistent one-sided reduction in the limit when the ratio is large, as appropriate to many materials.

During solidification of a kinetically-supercooled liquid, the latent heat released upon solidification results in an increase of the local temperature – the process known as recalescence (Feuillebois et al. [8]). When the latent heat is higher than the initial sensible heat, the local temperature rises rapidly to the values close to the equilibrium melting temperature. In the simple, one-sided model, this can be shown also formally: for large times, the solutions tend to the classical Neumann solutions for equilibrium solidification. On the other hand, when the latent heat is lower than the initial sensible heat, the one-sided problem admits a large-time, travelling-wave solution with interface temperature below the equilibrium melting temperature. The same dependence of the large-time behaviour on the relative magnitude of the latent and sensible heats has been found also in the two-sided problem with a thermally insulated solid (Glicksman & Schaefer [9], Charach & Zaltzman [10]).

The energy conserving, one-sided reductions mentioned above hinged on the assumption that the solid in the underlying two-sided problem was thermally insulated. However, there are situations in practice where the solid is in thermal contact with isothermal surroundings, e.g. solidification of a liquid layer or a drop on an isothermal substrate (Schremb et al. [2]; Tembely & Dolatabadi [11]). In such cases, the appropriate boundary conditions are the fixed-temperature ones. For the planar Stefan problem with kinetic supercooling subject to such boundary conditions, the one-sided reductions of Evans & King [6] and Myers et al. [7] are no longer valid.

In the mathematical modelling of the solidification problems, the systems are typically assumed to occupy an infinite or a semi-infinite domain. The rationale behind this assumptions is that the analysis of the governing equations is simpler and the explicit solutions, if they exist, can be found only on infinite or semi-infinite domains. However, the dynamics on an unbounded domains can be completely different than that on a finite one. A simple example is the appearance of a steady temperature profile on a finite domain. The semi-infinite approximation is useful at the early stages, where the solidification starts at one boundary so that the system does not ‘feel’ the second boundary. However, at later times, the finite extent of the domain has to be taken into account. The implications of the finite domain in the case of binary alloy solidification have been analysed by Gewecke & Schulze [12]. Similarly as in their work, we study the possibility of the formation of quasi-steady temperature profile and its consequences.

In section 2 we formulate the problem of supercooled solidification of a pure material in a finite-size domain with the isothermal boundary conditions, consistently incorporating a solid phase in the two-phase model. In section 3, the full problem is solved numerically. In section 4 we analyse the short-time dynamics in an effectively semi-infinite domain, before the finite extent of the domain becomes effective. We consider the cases of both strong and weak latent-heat release. For weak latent-heat release, large-time solutions are derived that describe the thermal evolution in the growing solid phase, absent from the previous analyses of one-sided supercooled Stefan problem (Umantsev [13], Font at al. [14]). In section 5 we provide asymptotic results for the stages after the finite extent of the system became effective. Discussion of the results and conclusions are provided in section 6.

2. Mathematical model

2.1. Dimensional formulation

We consider a one-dimensional region $0 < z < H$, initially occupied by a uniformly supercooled pure liquid at temperature $T_i < T_m$, where T_m is the equilibrium melting temperature. We assume that the solidification is initiated at time $t = 0$. At later times, the growing solid region, $0 < z < h(t)$, is separated from the liquid region, $h(t) < z < H$, by a moving interface at $z = h(t)$. We denote $T_s(z,t)$ and $T_l(z,t)$ the temperature fields in the solid and liquid phases, respectively. We consider fixed-temperature boundary conditions with $T_s(0,t) = T_l(H,t) = T_i$. The unknown temperature at the interface is $T_h(t) \equiv T(h(t),t)$. Since there is no solid at $t = 0$, we set $h(0) = 0$. The situation is depicted in figure 2.1.

The governing equations for the temperature in the solid and liquid, respectively, are

$$\frac{\partial T_s}{\partial t} = \kappa_s \frac{\partial^2 T_s}{\partial z^2} \quad \text{and} \quad \frac{\partial T_l}{\partial t} = \kappa_l \frac{\partial^2 T_l}{\partial z^2}, \tag{2.1a, b}$$

where $\kappa_{s,l}$ are the heat diffusivities in the solid and liquid phases. The heat conservation at the interface is expressed by the Stefan condition

$$\rho L_{\text{eff}} \dot{h} = k_s \left.\frac{\partial T}{\partial z}\right|_{h^-} - k_l \left.\frac{\partial T}{\partial z}\right|_{h^+}, \tag{2.2}$$

where ρ is the density, $k_{s,l}$ are the thermal conductivities in the solid and liquid phases and

$$L_{\text{eff}}(t) \equiv L_m - (C_{pl} - C_{ps})[T_m - T_h(t)] \tag{2.3}$$

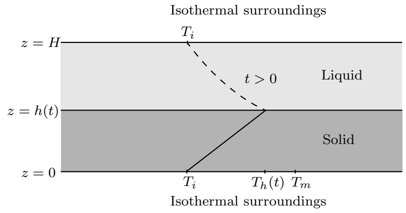

Figure 2.1: A definition sketch. The liquid is initially supercooled by $\Delta T \equiv T_m - T_i$, where T_m is the equilibrium melting temperature and T_i is a constant initial temperature. The solid and dashed curves correspond to representative temperature profiles in the solid and liquid phases at a later instant, respectively.

is the effective latent heat, dependent on the local degree of supercooling. Here, L_m is the latent heat of equilibrium solidification and $C_{ps,l}$ are the heat capacities of the respective phases. The effective latent heat represents an approximation of the latent heat of non-equilibrium solidification (for details, see Charach & Zemel [15]; Charach & Zaltzman [10]; Kostinski & Cantrell [4]).

As we are not interested in the volume-change effects upon solidification, we have set the densities in both phases to be the same. On the other hand, we assume different values of thermal conductivities and heat capacities in the solid and liquid phases. Note that $L_{\text{eff}} = L_m$ when $C_{ps} = C_{pl}$. Since the supercooled solidification is an exothermic process, the rate of release of the effective latent heat must always be non-negative, i.e. $L_{\text{eff}}(t) \geq 0$ for all times. Since in real systems $C_{pl} > C_{ps}$, there is a maximum allowed value of the initial supercooling

$$\Delta T \leq \Delta T_{\max} \equiv L_m/(C_{pl} - C_{ps}), \tag{2.4}$$

where $\Delta T \equiv T_m - T_i$. In deriving the above inequality we used that ΔT is the maximum value of $T_m - T_h(t)$.

The solidification rate is determined by the attachment kinetics. For small supercoolings, $\Delta T/T_m \ll 1$, it is given by the linear kinetic law

$$\dot{h} = G(T_m - T_h), \tag{2.5}$$

where G is the kinetic coefficient, calculated as (Ashby & Jones [3])

$$G = \frac{d}{6\hbar T_m} \frac{L_m w}{N_A} \exp(-q/k_B T_m), \tag{2.6}$$

where d is the molecular diameter, $\hbar$ the Planck constant, q the activation energy, k_B the Boltzmann constant, w the molecular weight and N_A the Avogadro constant.

Since we have fixed-temperature boundary conditions with the same temperatures, $T = T_i$, at both ends, the only possible temperature distribution as

Parameter	Water	Copper	Salol
$d/(10^{-9}\text{ m})$	0.29	0.23	1
$q/(10^{-20}\text{ J})$	3	6.71	6.61
$k_s/(\text{W m}^{-1}\text{K}^{-1})$	2.25	401	0.34
$k_l/(\text{W m}^{-1}\text{K}^{-1})$	0.56	157	0.18
$\rho/(10^3\text{ kg m}^{-3})$	1	8.02	1.18
$C_{ps}/(10^3\text{ J kg}^{-1}\text{K}^{-1})$	2.09	0.385	1.16
$C_{pl}/(10^3\text{ J kg}^{-1}\text{K}^{-1})$	4.22	0.53	1.58
$L_m/(10^5\text{ J kg}^{-1})$	3.34	2.09	0.90
T_m/K	273.15	1360	316
$\Delta T/\text{K}$	5	50	5
$G/(\text{m K}^{-1}\text{s}^{-1})$	9.32×10^{-4}	$2.63{\times}10^{-2}$	$6.65{\times}10^{-6}$
τ_H/s	7.54×10^4	$2.70{\times}10^2$	1.04×10^5
τ_G/s	6.12×10^{-3}	$2.14{\times}10^{-5}$	87
$\mathcal{G}$	3.51×10^3	3.55×10^3	34
$\mathscr{S}$	16	8	11
$\mathscr{S}_{\min}$	0.50	0.27	0.27

Table 1: Values of physical parameters for water, copper and salol. For the definitions of symbols see text. In calculating τ_H and $\mathcal{G}$, we have set $H = 0.1$ m in all three cases. The values of the activation energy, q, for copper and salol are taken from Font et al. [14] and that for water from Barahona [16]. Note that the value of $\mathcal{G}$ of salol is two orders of magnitude smaller than those of water and copper.

$t \to \infty$ is $T \equiv T_i$. Since $T_i < T_m$, it follows that the system must completely freeze in finite time since otherwise (2.5) would imply $h \sim G(T_m - T_i)t$ as $t \to \infty$, which would not be consistent with the finite extent of the system. Therefore we can define t_f, the time of complete freezing, as

$$h(t_f) = H. \tag{2.7}$$

The value of t_f is determined as part of solution.

2.2. Separation of dimensional scales

The present problem involves two independent sets of scales. The length-scales and time-scales determined by the attachment kinetics are

$$\ell_G \equiv \kappa_l / G\Delta T \quad \text{and} \quad \tau_G \equiv \kappa_l / G^2 \Delta T^2, \qquad (2.8a,\ b)$$

respectively. The second scaling is the thermal one, given by the finite extent of the region and the characteristic thermal diffusion time:

$$\ell_H \equiv H \quad \text{and} \quad \tau_H \equiv H^2 / \kappa_l. \qquad (2.9a,\ b)$$

The kinetic scales are the natural choice when the liquid is semi-infinite for they do not involve H. We shall consider situation that occurs typically in practice, when the kinetic and thermal scales are separated, so that $\ell_G \ll \ell_H$ and $\tau_G \ll \tau_H$. The relative magnitude of the two-length scales or the time-scales is measured by the dimensionless number

$$\mathcal{G} \equiv \ell_H/\ell_G = (\tau_H/\tau_G)^{1/2} = G\Delta T H/\kappa_l, \tag{2.10}$$

which can also be interpreted either as the dimensionless kinetic coefficient or the dimensionless extent of the system (see section 2.3). The separation of scales is equivalent to the asymptotic limit of large $\mathcal{G}$. On the other hand, it follows from (2.10) that $\mathcal{G} \to 0$ when $\Delta T \to 0$. Therefore, in order that we keep $\mathcal{G}$ large with small supercooling, we shall consider the following asymptotic range for ΔT:

$$\kappa_l/GH \ll \Delta T \ll T_m. \tag{2.11}$$

Note that the kinetic scales are related to the thermal ones through

$$\ell_G = \ell_H/\mathcal{G} \quad \text{and} \quad \tau_G = \tau_H/\mathcal{G}^2. \tag{2.12a, b}$$

In table 1 we present the representative values of $\mathcal{G}$ for water, copper and salol.

2.3. Dimensionless formulation

In order to highlight the differences between the kinetic and thermal scalings, we formulate the dimensionless equations in both. The dimensionless temperature is the same in both formulations,

$$\theta = (T - T_m)/\Delta T. \tag{2.13}$$

The effective range for θ is $-1 \leq \theta \leq 0$. The spatial and time variables are made dimensionless by

$$\hat{z} = z/\ell_i \quad \text{and} \quad \hat{t} = t/\tau_i, \tag{2.14a, b}$$

with $i = G$ or H for kinetic or thermal scalings, respectively. The hats denote the dimensionless variables and the scales ℓ_i and τ_i, $i = G, H$ are defined by (2.8*a, b*) and (2.9,*a, b*). The heat equations in the solid and liquid are formally the same in both scalings, as does the Stefan condition. Omitting the hats, the heat equations become

$$\frac{\partial \theta_s}{\partial t} = \kappa_{sl}\frac{\partial^2 \theta_s}{\partial z^2} \quad \text{and} \quad \frac{\partial \theta_l}{\partial t} = \frac{\partial^2 \theta_l}{\partial z^2}, \tag{2.15a, b}$$

with $\kappa_{sl} \equiv \kappa_s/\kappa_l$. The dimensionless Stefan condition reads

$$(\mathscr{S} + \mathscr{S}_{\min}\theta_h)\dot{h} = k_{sl}\left.\frac{\partial \theta_s}{\partial z}\right|_{h^-} - \left.\frac{\partial \theta_l}{\partial z}\right|_{h^+}, \tag{2.16}$$

with $k_{sl} \equiv k_s/k_l$ and the dimensionless Stefan number, $\mathscr{S}$, defined as

$$\mathscr{S} \equiv L_m/C_{pl}\Delta T. \tag{2.17}$$

The inequality (2.4) gives the minimum attainable value of Stefan number, $\mathscr{S}_{\min}$, such that

$$\mathscr{S} \geq \mathscr{S}_{\min} \geq 0, \tag{2.18}$$

where

$$\mathscr{S}_{\min} \equiv L_m / C_{pl} \Delta T_{\max} = 1 - C_{psl}, \tag{2.19}$$

with $\Delta T_{\max}$ defined in (2.4) and $C_{psl} \equiv C_{ps}/C_{pl}$. In both scalings, the initial conditions and the condition at the solid bottom are

$$t = 0: \quad h = 0, \; \theta_l = -1, \qquad (2.20a,\ b)$$

$$z = 0: \quad \theta_s = -1. \qquad (2.20c)$$

The differences between the kinetic and thermal scalings appear in the kinetic law and the condition at the upper boundary. The dimensionless kinetic law is

$$\dot{h} = -\theta_h, \quad \text{(kinetic scaling)} \qquad (2.21a)$$

$$\mathcal{G}^{-1}\dot{h} = -\theta_h \quad \text{(thermal scaling)} \qquad (2.21b)$$

and the condition at the upper boundary becomes

$$z = \mathcal{G}: \quad \theta_l = -1, \quad \text{(kinetic scaling)} \qquad (2.22a)$$

$$z = 1: \quad \theta_l = -1. \quad \text{(thermal scaling)} \qquad (2.22b)$$

The system can effectively be treated semi-infinite at early stages, during which the temperature disturbance, caused by the latent-heat release at the interface, has not got enough time to propagate to the vicinity of the upper boundary. Therefore, at early times, we can set $H = \infty$ so that the kinetic scales are the only natural scales. For times when the finite extent of the liquid becomes relevant, we employ the thermal scaling. Below, we use both dimensionless formulations in order to develop the asymptotic solutions valid at different stages of the system's evolutions. For the purpose of further discussion, we denote by t_∞ the duration of the stage during which the system is effectively semi-infinite.

3. Full model: numerical solutions

For the full model, the finite height of the liquid affects the dynamics so that H and τ_H are the natural length and time scales, respectively. To solve the problem numerically, we first fix the moving boundary by the space coordinate transformations

$$\xi \equiv \begin{cases} \dfrac{z}{h}, & \text{for} \quad 0 \leq z \leq h, \\ \dfrac{1-z}{1-h}, & \text{for} \quad h \leq z \leq 1, \end{cases} \tag{3.1}$$

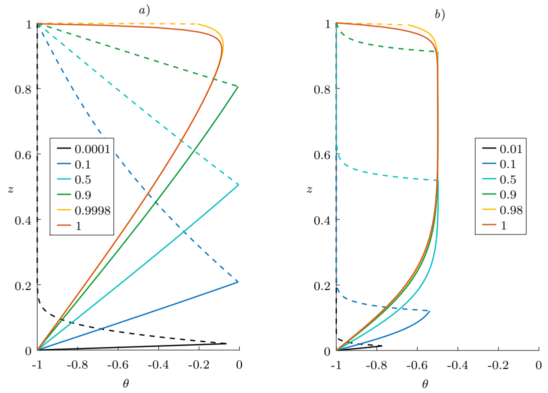

Figure 3.1: *a*) Dimensionless temperature profiles in the solid (solid curves) and liquid (dashed curves) for $\mathscr{S} = 10$ and $\mathcal{G} = 100$, shown at several time instants, $t/t_f = 0.0001, 0.1, 0.5, 0.9, 0.9998$ and 1, where $t_f = 1.64$ is the complete-freezing time. The completely solid curve (red) corresponds to the instant of complete freezing, $t = t_f$. *b*) The same for $\mathscr{S} = 0.5$, $\mathcal{G} = 100$ and $t/t_f = 0.01, 0.1, 0.5, 0.9, 0.98$ and 1, where $t_f = 1.95 \times 10^{-4}$. In both figures, we have set $k_{sl} = 1$ and $\mathscr{S}_{\min} = 0$.

which transforms both the solid and liquid regions onto interval $0 \le \xi \le 1$, with $\xi = 1$ corresponding to the interface in both phases. The heat equations in the solid and liquid phases, respectively, become

$$h^2 \frac{\partial \theta_s}{\partial t} = \xi \dot{h} h \frac{\partial \theta_s}{\partial \xi} + \kappa_{sl} \frac{\partial^2 \theta_s}{\partial \xi^2}, \tag{3.2a}$$

$$(1-h)^2 \frac{\partial \theta_l}{\partial t} = -\xi \dot{h} (1-h) \frac{\partial \theta_l}{\partial \xi} + \frac{\partial^2 \theta_l}{\partial \xi^2}. \tag{3.2b}$$

The Stefan condition transforms as follows

$$(\mathscr{S} + \mathscr{S}_{\min}\theta_h)\dot{h} = \frac{k_{sl}}{h} \left.\frac{\partial \theta_s}{\partial \xi}\right|_{1^-} + \frac{1}{1-h} \left.\frac{\partial \theta_l}{\partial \xi}\right|_{1^-}. \tag{3.3}$$

A fully-implicit finite-difference scheme in time is combined with central differences for space derivatives to produce the tridiagonal algebraic system from (3.2*a*, *b*). Moving boundary condition (3.3), with $\dot{h}$ eliminated using (2.21*b*), is used to estimate θ_h. Moving boundary condition (2.21*b*) with an explicit relationship for $\dot{h}$ is then incorporated into an iterative scheme to update h. The numerical results check satisfactorily with an alternative approach in which only the space derivatives are discretized and the resulting ordinary differential equations are integrated in time using well-established stiff-system algorithms.

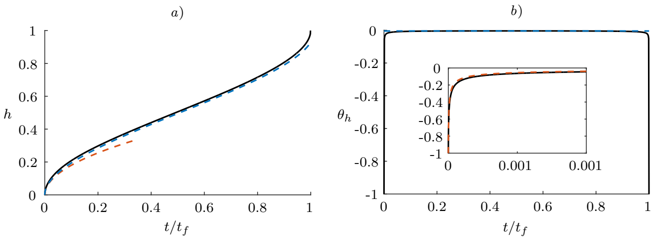

Figure 3.2: *a*) Dimensionless interface position, h, as a function of scaled time, t/t_f, where $t_f = 1.64$ is the complete-freezing time, for $\mathscr{S} = 10$ and $\mathcal{G} = 100$ (black solid curve). The red dashed curve corresponds to the asymptotic solution as $\mathscr{S} \to \infty$, given in (5.3*a*), derived in the semi-infinite domain (for more details, see section 4.2). The blue dashed curve corresponds to the asymptotic solution in the quasi-steady stage as $\mathscr{S} \to \infty$, given in (5.6). *b*) Dimensionless interface temperature, θ_h, as a function of scaled time t/t_f, for the same values of dimensionless parameters as in *a*) (black solid curve). The red dashed curve in the inset corresponds to the asymptotic solution (5.3*b*), plotted at early times. The blue dashed curve corresponds to the asymptotic solution in the quasi-steady stage, given in (5.13). In both figures we have set $\mathscr{S}_{\min} = 0$ and $k_{sl} = 1$.

The values of the Stefan numbers used deserve some comment. In the one-sided Stefan problem with kinetic supercooling on a semi-infinite domain, there are three distinct parametric regimes, yielding qualitatively different solutions as $t \to \infty$ (see also Davis [5]): $\mathscr{S} > 1$, $\mathscr{S} = 1$ and $\mathscr{S} < 1$. In the case with $\mathscr{S} > 1$, the solutions tend to the classical Neumann solutions with the interface temperature equal to the equilibrium melting temperature so that the solidification is dominated by the diffusion. When $\mathscr{S} < 1$, the system is said to be hypercooled. There is not enough latent heat to warm up the interface to the equilibrium temperature and, as a result, the interface temperature tends to a constant as $t \to \infty$, that is below the equilibrium melting temperature so that the solidification is dominated by the kinetic effects. The limiting temperature profile in the liquid has the form of a traveling wave. The case $\mathscr{S} = 1$ corresponds to the transition between the two regimes above. The same classification of the values of $\mathscr{S}$ applies for the two-phase problem on a semi-infinite domain with insulated solid (for more details, see Charach & Zaltzman [10]). In the present paper, we distinguish between the values of $\mathscr{S}$ less and greater than 1. We shall not consider the special case $\mathscr{S} = 1$ as it is more of theoretical than practical interest: in practice, it is unlikely to have a system with the values of physical parameters such that $\mathscr{S}$ is precisely equal to unity. In computing the numerical solutions, we set $\mathscr{S}_{\min} = 0$ as its finite values just move the origin for the parameter $\mathscr{S}$.

The numerical solutions of the full problem for large values of $\mathscr{S}$ are pre-

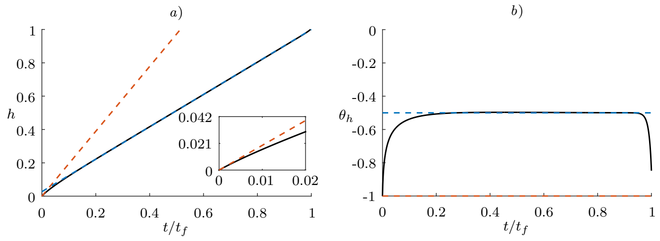

Figure 3.3: *a*) Dimensionless interface position, h, as a function of scaled time, t/t_f, where $t_f = 1.95 \times 10^{-4}$ is the complete-freezing time, for $\mathscr{S} = 0.5$ and $\mathcal{G} = 100$ (black solid curve). The red dashed line, given by $h = \mathcal{G}t$, represents the solution in the limiting case $\mathscr{S} = \mathscr{S}_{\min}$ (see section 4.3). The slope of the blue dashed line is equal to the large-time solidification rate, $\dot{h} = \mathcal{G}V$, with V given in (4.51), computed in the semi-infinite domain (see section 4.3). The inset zooms in the main plot at early times. Note that the red dashed line asymptotes the black curve as $t \to 0$. *b*) The dimensionless interface temperature, θ_h, as a function of scaled time t/t_f, for the same values of dimensionless parameters as in *a*). The red dashed line $\theta_h = -1$ represents the solution when $\mathscr{S} = \mathscr{S}_{\min}$. The blue dashed curve represents the large-time asymptotics in the semi-infinite domain, given by (4.47*b*). In both figures we have set $\mathscr{S}_{\min} = 0$ and $k_{sl} = 1$.

sented in figure 3.1(*a*) for the temperature profiles and in figures 3.2(*a, b*) for the interface position and temperature. A rapid recalescence takes place at early times. As the finite extent of the domain comes into effect, there is a transient period during which the temperature in the liquid relaxes towards a quasi-steady state, in which the temperature is linear and the interface temperature is close to the equilibrium melting temperature. Consequently, the solidification rate is almost constant. The quasi-steady profile in the liquid exists until the system freezes completely. On the other hand, the temperature in the solid remains quasi-steady until the terminal stage of solidification as $t \to t_f$, during which $\theta_h \to -1$ and $\dot{h} \to \mathcal{G}$.

The results for $\mathscr{S} < 1$ are presented in figure 3.1(*b*) for the temperature profiles and in figures 3.3(*a, b*) for the interface position and temperature. In the solid, the temperature is quasi-steady only during a short initial period. This is in contrast with the case when $\mathscr{S} > 1$. At later times, a thermal boundary layer at the bottom of the solid forms and the temperature is almost constant through the rest of the solid. At these later stages, the temperature in the liquid has travelling-wave character until a short terminal stage, when a rapid drop in the interface temperature occurs as the finite extent of the domain becomes effective. Also note that the solidification rate is almost constant most of the time, except from the short periods at the beginning and end of solidification, see figure 3.3(*a*).

The evolution of the system for $t > t_f$, not shown in figures 3.1(a, b), is given by relaxation towards the homogeneous temperature $\theta \equiv -1$. In the next two sections, we derive asymptotic results to gain better insight into the numerical solutions presented above and to understand the differences between the dynamics in the semi-infinite and finite domains.

4. Asymptotics: semi-infinite domain

When the liquid is effectively semi-infinite, the kinetic scaling, defined by (2.14a, b) with $i = G$, is the natural one to be adopted. In such case, the boundary condition (2.22a) is replaced by

$$z \to \infty: \quad \theta_l \to -1. \tag{4.1}$$

In the solid phase, we introduce a scaled spatial variable

$$\xi \equiv z/h. \tag{4.2}$$

The heat equation in the solid transforms as

$$h^2 \frac{\partial \theta_s}{\partial t} - \xi \dot{h} h \frac{\partial \theta_s}{\partial \xi} = \kappa_{sl} \frac{\partial^2 \theta_s}{\partial \xi^2} \tag{4.3}$$

and is subject to

$$\xi = 0: \quad \theta_s = -1, \tag{4.4a}$$
$$\xi = 1: \quad \theta_s = \theta_h. \tag{4.4b}$$

In the liquid, we introduce

$$\eta \equiv z - h, \tag{4.5}$$

so that the heat equation transforms as

$$\frac{\partial \theta_l}{\partial t} - \dot{h} \frac{\partial \theta_l}{\partial \eta} = \frac{\partial^2 \theta_l}{\partial \eta^2} \tag{4.6}$$

and is subject to

$$\eta = 0: \quad \theta_l = \theta_h, \tag{4.7a}$$
$$\eta \to \infty: \quad \theta_l \to -1. \tag{4.7b}$$

Finally, the Stefan condition becomes

$$(\mathscr{S} + \mathscr{S}_{\min}\theta_h)\dot{h} = \frac{k_{sl}}{h} \frac{\partial \theta_s}{\partial \xi}\bigg|_{1^-} - \frac{\partial \theta_l}{\partial \eta}\bigg|_{0^+}. \tag{4.8}$$

We begin with the analysis of the small-time behaviour.

4.1. Small-time solutions with $\mathscr{S} = O(1)$

Since $h \ll \kappa_{sl}$ as $t \to 0$, for fixed value of κ_{sl}, and $\dot{h} \sim 1$ as $t \to 0$, the diffusive term in (4.3) dominates. Hence, the temperature in the solid is linear to leading order in small t, which, together with the boundary conditions, yields

$$\theta_s(\xi, t) \sim -1 + [1 + \theta_h(t)]\xi \quad \text{as} \quad t \to 0, \tag{4.9}$$

with ξ fixed. In the liquid phase, we define a similarity variable

$$\zeta \equiv \eta / t^{1/2}, \tag{4.10}$$

where η is given by (4.5), so that (4.6) becomes

$$t\frac{\partial \theta_l}{\partial t} - t^{1/2}\dot{h}\frac{\partial \theta_l}{\partial \zeta} - \frac{1}{2}\xi\frac{\partial \theta_l}{\partial \zeta} = \frac{\partial^2 \theta_l}{\partial \zeta^2}. \tag{4.11}$$

The small-time limit suggests the temperature field of the form

$$\theta_l(\zeta, t) = -1 + tF(\zeta, t), \tag{4.12}$$

with $F = O(1)$ as $t \to 0$ and $F \to 0$ as $\zeta \to \infty$. The prefactor t in the second term on the right-hand side of (4.12) follows from the Stefan condition, where the dominant balance as $t \to 0$ is between the latent-heat release at the interface and the conduction through the solid. This is in contrast with the small-time solutions of the two-sided Stefan problem with thermally insulated solid (Charach & Zaltzman [10]) and with those of the one-sided Stefan problem, derived by Font et al. [14]. Those solutions had $t^{1/2}$ as a prefactor in (4.12), determined by the leading-order balance between the latent-heat release and the conduction through the liquid. As a result we obtain a finite recalescence rate as $t \to 0$, which is in contrast with the problems mentioned above, where it was $O(t^{-1/2})$ as $t \to 0$. Inserting (4.12) into (4.6), we get

$$\frac{\partial^2 F}{\partial \zeta^2} + \frac{1}{2}\zeta\frac{\partial F}{\partial \zeta} - F = t\frac{\partial F}{\partial t} - t^{1/2}\dot{h}\frac{\partial F}{\partial \zeta}. \tag{4.13}$$

The form of (4.13) implies the expansion

$$F(\zeta, t) = F_0(\zeta) + t^{1/2}F_1(\zeta) + O(t) \quad \text{as} \quad t \to 0. \tag{4.14}$$

Consequently, we obtain

$$h \sim t - \frac{1}{2}F_0(0)t^2 - \frac{2}{5}F_1(0)t^{5/2}, \tag{4.15a}$$

$$\theta_h \sim -1 + F_0(0)t + F_1(0)t^{3/2} \tag{4.15b}$$

as $t \to 0$, where we have used (2.21a) and (4.12), together with (4.14). The values of $F_0(0)$ and $F_1(0)$ are yet unknown. We express the Stefan condition, using (4.9) and (4.14), as

$$(\mathscr{S} + \mathscr{S}_{\min}\theta_h)\dot{h} = k_{sl}\frac{1 + \theta_h}{h} - t^{1/2}F'(0, t). \tag{4.16}$$

Inserting (4.14) into (4.13), we obtain a sequence of ordinary differential equations, together with corresponding boundary conditions. For the purpose of the present study, we will solve only for F_0. At $O(t^0)$ we obtain

$$F_0'' + \tfrac{1}{2}\zeta F_0' - F_0 = 0, \tag{4.17}$$

subject to

$$\zeta = 0: \quad F_0 = F_0(0), \tag{4.18a}$$
$$\zeta \to \infty: \quad F_0 \to 0. \tag{4.18b}$$

Plugging (4.15*a, b*) into (4.16), we obtain at $O(t^0)$ and $O(t^{1/2})$, respectively,

$$F_0(0) = (\mathscr{S} - \mathscr{S}_{\min})/k_{sl} \quad \text{and} \quad F_1(0) = F_0'(0)/k_{sl}. \tag{4.19$a,\ b$}$$

The equation (4.17) can be solved in terms of the repeated integrals of the complementary error function (Boisvert et al. [17], p. 167). The solution reads

$$F_0(\zeta) = k_{sl}^{-1}(\mathscr{S} - \mathscr{S}_{\min}) \left[(1 + \tfrac{1}{2}\zeta^2)\,\mathrm{erfc}(\zeta/2) - \tfrac{1}{\pi^{1/2}}\zeta\,\mathrm{e}^{-\zeta^2/4}\right], \tag{4.20}$$

where we have used (4.19*a*) and erfc is the complementary error function. Using (4.20) and (4.19*b*) we determine $F_1(0)$, so that

$$h \sim t - \frac{\mathscr{S} - \mathscr{S}_{\min}}{k_{sl}} \left(\frac{1}{2}t^2 - \frac{4}{5\pi^{1/2}k_{sl}}t^{5/2}\right), \tag{4.21a}$$
$$\theta_h \sim -1 + \frac{\mathscr{S} - \mathscr{S}_{\min}}{k_{sl}} \left(t - \frac{2}{\pi^{1/2}k_{sl}}t^{3/2}\right). \tag{4.21b}$$

Note that the above approximations apply as long as

$$t \ll k_{sl}/(\mathscr{S} - \mathscr{S}_{\min}), \tag{4.22}$$

which constraints the validity of the small-time solutions considerably when $\mathscr{S}$ is large. However, the small-time solutions provide useful information about the behaviour of the system at the beginning of the solidification, e.g. we obtain the initial recalescence rate as

$$\dot{\theta}_h(0) = (\mathscr{S} - \mathscr{S}_{\min})/k_{sl}, \tag{4.23}$$

which is an exact result, valid for all $\mathscr{S} \geq \mathscr{S}_{\min}$. The unbounded value of $\dot{\theta}_h(0)$ as $\mathscr{S} \to \infty$ indicates that the recalescence occurs infinitely fast. On the other hand, as $\mathscr{S} \to \mathscr{S}_{\min}$, the effective latent heat vanishes so that the system solidifies isothermally at constant rate $\dot{h} = 1$ and with $\theta_s \equiv \theta_l \equiv -1$.

4.2. Asymptotic solutions as $\mathscr{S} \to \infty$

The singularity of the small-time limit as $\mathscr{S} \to \infty$ suggests that the full problem, given by (2.21*a*), (4.3), (4.11) and (4.8), should be treated as a boundary-layer one in the time variable, with the boundary layer of thickness $1/\mathscr{S}$ as

$\mathscr{S} \to \infty$, located at $t = 0$. The existence of the boundary layer can be inferred also from the fact that the formal application of the limit $\mathscr{S} \to \infty$, with t fixed, in (2.21a) and (4.8) results in $\dot{h} = 0$ and $\theta_h = 0$ to leading order. Hence the boundary layer is needed in order to satisfy the initial condition $\theta_h(0) = -1$. To solve the boundary-layer problem systematically, we employ the method of matched asymptotic expansions (Lagerstrom & Casten [18]). The idea of the method lies in seeking for the solutions in two special asymptotic limits as $\mathscr{S} \to \infty$: the inner limit, corresponding to $t \ll 1$, and the outer limit, corresponding to $t = O(1)$. Finally, the asymptotic solutions valid uniformly for all t are constructed by a consistent matching of the inner and outer solutions.

4.2.1. Inner solutions – recalescence stage

We define the inner time variable via the following relation

$$t = \tau/\mathscr{S}, \quad \tau = O(1) \quad \text{as} \quad \mathscr{S} \to \infty, \tag{4.24}$$

together with the condition $\zeta = O(1)$ as $\mathscr{S} \to \infty$. The inner time scale corresponds to the recalescence stage of solidification, during which $\theta_h = O(1)$. Hence, the kinetic law (2.21a) implies the following scaling of the interface position

$$h_{\text{in}}(\tau) \equiv h(\tau/\mathscr{S}) = \mathscr{S}^{-1}\nu(\tau), \tag{4.25}$$

with $\nu = O(1)$ as $\mathscr{S} \to \infty$. The temperature in the liquid and the interface temperature, respectively, in the inner limit are defined as follows

$$\vartheta(\zeta, \tau) \equiv \theta_l(\zeta, \tau/\mathscr{S}) \quad \text{and} \quad \vartheta_h(\tau) \equiv \theta_h(\tau/\mathscr{S}), \tag{4.26a, b}$$

with ϑ and $\vartheta_h = O(1)$ as $\mathscr{S} \to \infty$. With the above scalings the kinetic equation becomes

$$\dot{\nu} = -\vartheta_h, \tag{4.27}$$

where the dot denotes differentiation with respect to τ. In the solid phase, the linear profile (4.9) is a consistent leading-order approximation in the inner limit. The scaling of (4.11) suggests the following expansion

$$\vartheta \sim \vartheta_0 + (1/\mathscr{S})^{1/2}\vartheta_1. \tag{4.28}$$

Consequently,

$$\vartheta_h \sim \vartheta_h^0 + (1/\mathscr{S})^{1/2}\vartheta_h^1, \tag{4.29a}$$

$$\nu \sim \nu_0 + (1/\mathscr{S})^{1/2}\nu_1. \tag{4.29b}$$

At leading order, (4.11), (4.25) and (4.26a, b) imply

$$\tau\frac{\partial\vartheta_0}{\partial\tau} - \frac{1}{2}\zeta\frac{\partial\vartheta_0}{\partial\zeta} = \frac{\partial^2\vartheta_0}{\partial\zeta^2}, \tag{4.30}$$

which is subject to

$$\zeta = 0: \quad \vartheta_0 = \vartheta_h^0, \tag{4.31a}$$

$$\zeta \to \infty: \quad \vartheta_0 \to -1, \tag{4.31b}$$

$$t = 0: \quad \vartheta_0 \equiv -1. \tag{4.31c}$$

In the Stefan condition, the leading-order balance is between the latent-heat release and the heat flow through the solid. Therefore, the Stefan condition and the kinetic equation, respectively, yield

$$\dot{\nu}_0 = k_{sl}\frac{1+\vartheta_h^0}{\nu_0}, \quad \text{and} \quad \dot{\nu}_0 = -\vartheta_h^0, \tag{4.32a, b}$$

subject to the initial conditions $\nu_0(0) = 0$ and $\vartheta_h^0(0) = -1$. The above equations admit the solutions

$$\nu_0(\tau) = k_{sl}\left[\left(\frac{2\tau}{k_{sl}}+1\right)^{1/2} - 1\right], \tag{4.33a}$$

$$\vartheta_h^0(\tau) = -\left(\frac{2\tau}{k_{sl}}+1\right)^{-1/2}. \tag{4.33b}$$

The solution (4.33b) is used to solve for ϑ_0, given by the leading-order problem (4.30) and (4.31), by the application of the Duhamel's theorem (see Appendix A). The solution can be expressed as

$$\vartheta_0(\zeta,\tau) = -\operatorname{erf}(\zeta/2) + \vartheta_h^0(\tau)\,\mathrm{e}^{-\zeta^2/4}\,R[\vartheta_h^0(\tau)\zeta], \tag{4.34}$$

where

$$R(y) \equiv \mathrm{e}^{y^2/4}\operatorname{erfc}(|y|/2)\,. \tag{4.35}$$

Note that $R(0) = 1$ and $R(\infty) = 0$.

4.2.2. *Outer solutions – post-recalescence stage*

In order to derive the outer solutions, we take $t = O(1)$ as $\mathscr{S} \to \infty$, with $\zeta = O(1)$. Physically, the outer solutions correspond to the post-recalescence stage, during which the interface is close to the equilibrium so that $\theta_h \ll 1$, yet the thickness of the solid region is still small. The dominant balance in the Stefan condition is again between the latent-heat release and the heat conduction through the solid. Hence, the leading-order interface temperature scales as

$$\theta_h^{\text{out}} \sim \mathscr{S}^{-1/2}\theta_h^0, \tag{4.36}$$

with $\theta_h^0 = O(1)$ as $\mathscr{S} \to \infty$. The kinetic law (2.21a) implies that

$$h_{\text{out}} \sim \mathscr{S}^{-1/2}h_0, \tag{4.37}$$

with $h_0 = O(1)$ as $\mathscr{S} \to \infty$. Since $h_{\text{out}} \ll 1$, the temperature profile in the solid is quasi-steady to leading order, given by

$$\theta_s^{\text{out}} \sim \xi - 1. \tag{4.38}$$

The heat conduction in the liquid, given by (4.11), together with (4.37), imply

$$\theta_l^{\mathrm{out}} \sim \theta_0 + \mathscr{S}^{-1/2}\theta_1, \tag{4.39}$$

with $\theta_{0,1} = O(1)$ as $\mathscr{S} \to \infty$. Inserting (4.39) and (4.37) into (4.11), we obtain at leading order

$$t\frac{\partial \theta_0}{\partial t} - \frac{1}{2}\zeta\frac{\partial \theta_0}{\partial \zeta} = \frac{\partial^2 \theta_0}{\partial \zeta^2}, \tag{4.40}$$

subject to the following boundary conditions

$$\zeta = 0: \quad \theta_0 = 0, \tag{4.41a}$$

$$\zeta \to \infty: \quad \theta_0 \to -1. \tag{4.41b}$$

The condition (4.41a) has been imposed in order that (4.39), expressed at $\zeta = 0$, be consistent with (4.36), so that $\theta_h^0(t) = \theta_1(0,t)$. At leading order, the Stefan condition yields

$$\dot{h}_0 = k_{sl}/h_0, \tag{4.42}$$

with general solution $h_0 = (2k_{sl}t + a)^{1/2}$, where a is a constant to be determined by asymptotic matching.

4.2.3. Asymptotic matching

The initial condition for θ_0 must be specified so that the outer and inner solutions match to leading order in an overlap region $\mathscr{S}^{-1} \ll t \ll 1$. The matching requires

$$\theta_0(\zeta, 0) = \vartheta_0(\zeta, \infty) = -\operatorname{erf}(\zeta/2) \tag{4.43}$$

and $a = 0$. However, since the function $-\operatorname{erf}(\zeta/2)$ is already a time-independent solution of (4.40) satisfying (4.41a, b), the outer solutions are simply

$$h_{\mathrm{out}}(t) \sim (2k_{sl}t/\mathscr{S})^{1/2} \quad \text{and} \quad \theta_h^{\mathrm{out}}(t) \sim -(2\mathscr{S}t/k_{sl})^{-1/2}. \tag{4.44a, b}$$

Finally, the uniformly valid, leading-order solutions are obtained by adding the inner and outer solutions and subtracting their common values in the overlap region. In the present case, the overlap values coincide with the outer solutions so that the composite solutions are identical with the inner ones. Thus, we obtain the leading-order, uniformly valid temperature field

$$\theta_l(\zeta, t) \sim -\operatorname{erf}(\zeta/2) + \theta_h(t)\,\mathrm{e}^{-\zeta^2/4}\,R[\theta_h(t)\zeta], \tag{4.45}$$

with the function R defined in (4.35) and the leading-order interface temperature and position, respectively,

$$h(t) \sim \frac{k_{sl}}{\mathscr{S}}\left[\left(\frac{2\mathscr{S}t}{k_{sl}} + 1\right)^{1/2} - 1\right], \tag{4.46a}$$

$$\theta_h(t) \sim -\left(\frac{2\mathscr{S}t}{k_{sl}} + 1\right)^{-1/2}, \tag{4.46b}$$

as $\mathscr{S} \to \infty$.

Large-time analysis of the governing equations confirms that the outer solutions are identical with the leading-order, large-time solutions when $\mathscr{S} > 1$, similarly as in the one-sided Stefan problem (Davis [5]). We shall not provide further details here and note only that the large-time analysis can be provided by introduction of a small, artificial parameter ε and by rescaling $t = \tau/\varepsilon$ with $\tau = O(1)$ as $\varepsilon \to 0$ (Lagerstrom & Casten [18]).

4.3. *Asymptotic solutions for $\mathscr{S} < 1$*

The latent-heat release is weak when the system is initially hypercooled. For $\mathscr{S} = \mathscr{S}_{\min}$, there is no latent heat that would cause temperature rise from the initial value. Hence, $\theta_s \sim -1$, $\theta_l \sim -1$, $\theta_h \sim -1$ and $h \sim t$ as $\mathscr{S} \to \mathscr{S}_{\min}$; see also the discussion after (4.23). The next terms in the expansions are $O(\mathscr{S} - \mathscr{S}_{\min})$ and can be sought for only numerically. However, useful information can be taken from the large-time solutions for finite values of $\mathscr{S} - \mathscr{S}_{\min}$. For the one-sided, kinetically supercooled Stefan problem on a semi-infinite domain, there exists a traveling-wave temperature profile in the liquid as $t \to \infty$ when $\mathscr{S} < 1$ (Davis [5]). The same is true for the two-sided problem with thermally insulated solid, studied by Charach & Zaltzman [10], where the solid was isothermal for large times. We shall show that the travelling-wave profile develops also in the present case. However, there is a new feature concerning the temperature in the solid, which is almost constant, equal to θ_h, except to a boundary layer of thickness $(4\kappa_{sl}t)^{1/2}$ at the bottom of the solid.

To leading order, we assume

$$h \sim Vt \quad \text{and} \quad \theta_h \sim -V, \tag{4.47a, b}$$

as $t \to \infty$, where V is a constant to be determined. On introducing the large-time scaling $t = \tau/\varepsilon$, with $\tau = O(1)$ as $\varepsilon \to 0$ in (4.3), we obtain, for $\xi = O(1)$ and $\theta_h = O(1)$, constant leading-order temperature $\theta_s \equiv \theta_h$ as $\varepsilon \to 0$. Therefore, there must be a boundary layer at $\xi = 0$, in which the temperature changes from -1 to θ_h. The heat diffusion enters the dominant balance in (4.3) when $\xi = O(\varepsilon^{1/2})$. Therefore, we seek for a similarity solution $\theta_s = \theta_s(\bar{\xi})$ with $\xi = \bar{\xi}/t^{1/2}$ and $\bar{\xi} = O(1)$ as $t \to \infty$. From (4.3), we obtain the ordinary differential equation

$$\theta_s'' + (V^2/2\kappa_{sl})\bar{\xi}\theta_s' = 0, \tag{4.48}$$

where the primes denote the derivatives with respect to $\bar{\xi}$, which is subject to

$$\theta_s(0) = -1 \quad \text{and} \quad \theta_s(\infty) = \theta_h. \tag{4.49a, b}$$

The boundary condition as $\bar{\xi} \to \infty$ ensures matching with the constant outer solution, valid for $\xi = O(1)$ as $t \to \infty$. The temperature in the liquid, given by (4.6), has the travelling-wave profile similar to that in the one-sided, kinetically supercooled Stefan problem (Davis [5]). Thus we obtain

$$\theta_s(z,t) \sim -1 + \frac{\mathscr{S} - \mathscr{S}_{\min}}{1 - \mathscr{S}_{\min}} \operatorname{erf}[z/(4\kappa_{sl}t)^{1/2}], \tag{4.50a}$$

$$\theta_l(z,t) \sim -1 + \frac{\mathscr{S} - \mathscr{S}_{\min}}{1 - \mathscr{S}_{\min}}\, \mathrm{e}^{-V(z-h)}, \tag{4.50b}$$

as $t \to \infty$, where we have expressed the solutions using the variable z in order to highlight the spatial and temporal dependence of solutions. The solidification rate,

$$V = 1 - \frac{\mathscr{S} - \mathscr{S}_{\min}}{1 - \mathscr{S}_{\min}}, \tag{4.51}$$

follows from the Stefan condition and is the same as that in the one-sided supercooled Stefan problem (see Charach & Zaltzman [10]). The dominant balance in the Stefan condition, to leading order in t, is between the latent-heat release and the conduction through the liquid; the conduction through the solid is $O(t^{-1/2})$ as $t \to \infty$. This contrasts with the case when $\mathscr{S} > 1$. Note that (4.50a) satisfies the interface boundary condition with an exponentially small error as $t \to \infty$.

5. Asymptotics: finite domain

At times when the finite extent becomes relevant, we use thermal scaling. All the solutions of section 4, derived in the kinetic scaling can be expressed in the thermal one, in accordance with (2.12a, b), by the change of variables $z \mapsto \mathcal{G}z$, $h \mapsto \mathcal{G}h$ and $t \mapsto \mathcal{G}^2 t$. The variables ξ and ζ, defined in (3.1) and (4.10), respectively, are invariant with respect to the above change of variables.

When the liquid is finite, the asymptotic solutions of section 4, derived originally for the semi-infinite region, apply as long as $t < t_\infty$. In order to estimate t_∞, we consider the liquid as effectively semi-infinite as long as the temperature increase at the upper liquid boundary, given by $\theta_l[(1-h)/t^{1/2}, t]+1$, is less than some small factor, say δ, times the total temperature variation across the liquid, $\theta_h + 1$. When $\mathscr{S} \to \infty$, we obtain, using (4.45),

$$t_\infty \sim \tfrac{1}{4}[\mathrm{erfc}^{-1}(\delta)]^{-2} \approx 0.08 \tag{5.1}$$

to leading order, where we set $\delta = 10^{-2}$. In the kinetic scaling, the above relation implies $t_\infty = O(\mathcal{G}^2) \gg 1$ as $\mathcal{G} \to \infty$. When $\mathscr{S} \in (\mathscr{S}_{\min}, 1)$, (4.50$b$) implies

$$t_\infty = 1/\mathcal{G}V - \ln(1/\delta)/\mathcal{G}^2V^2 \approx 1/\mathcal{G}V - 4.6/\mathcal{G}^2V^2, \tag{5.2}$$

with $\delta = O(10^{-2})$. In the kinetic scaling, $t_\infty = O(\mathcal{G}/V) \gg 1$ as $\mathcal{G} \to \infty$. Hence, when $\mathcal{G}$ is large enough, the solutions have enough time to evolve close to their large-time asymptotics, derived in section 4.3, before the finite extent of the liquid comes into effect. This is confirmed also by the numerical solutions, shown in figure 3.1(b). The rest of this section is devoted to the asymptotic results explaining some of the features of the numerical results of section 3.

5.1. *Asymptotics as* $\mathscr{S} \to \infty$

The asymptotic solutions in the semi-infinite domain, given in (4.46*a, b*), expressed in the thermal scaling, become

$$h \sim \frac{k_{sl}}{\mathcal{G}\mathscr{S}}\left[\left(\frac{2\mathcal{G}^2\mathscr{S}t}{k_{sl}}+1\right)^{1/2}-1\right], \tag{5.3a}$$

$$\theta_h \sim -\left(\frac{2\mathcal{G}^2\mathscr{S}t}{k_{sl}}+1\right)^{-1/2} \tag{5.3b}$$

as $\mathscr{S} \to \infty$. The typical recalescence time, t_{rec}, is $O(\mathcal{G}^{-2}\mathscr{S}^{-1})$ as $\mathscr{S} \to \infty$.

5.1.1. *Relaxation towards the quasi-steady stage for* $t \ll \mathscr{S}$

In order to obtain consistent scalings as $\mathscr{S} \to \infty$, we assume that the heat conduction towards the liquid in the Stefan condition (3.3) is $O(1)$. For $t \ll \mathscr{S}$, the dominant balance is $\mathscr{S}\dot{h} = k_{sl}/h$. Hence, the solutions (4.44*a, b*), derived originally in the effectively semi-infinite liquid, still apply, even though the finite extent of the liquid has come into effect. Expressed in the thermal scaling, these solutions read

$$h \sim (2k_{sl}t/\mathscr{S})^{1/2} \quad \text{and} \quad \theta_h \sim -(2\mathcal{G}^2\mathscr{S}t/k_{sl})^{-1/2} \tag{5.4a, b}$$

as $\mathscr{S} \to \infty$ with $t \ll \mathscr{S}$.

In the liquid, times $t = O(1)$ correspond to the diffusion-driven relaxation towards the quasi-steady state, as follows from (3.2*b*) and (5.4*a, b*). For $1 \ll t \ll \mathscr{S}$, the temperature in the liquid becomes quasi-steady, so that $\theta_l \sim \xi - 1$ to leading order. At $t = O(\mathscr{S})$, the conduction towards the liquid enters the dominant balance in the Stefan condition (3.3), in which case all terms therein are $O(1)$ and quasi-steady, with $h = O(1)$ and $\theta_h = O(\mathscr{S}^{-1})$. This quasi-steady stage deserves further investigation.

5.1.2. *Quasi-steady stage for* $t = O(\mathscr{S})$

The quasi-steady stage can be analysed by introducing the scaling $t = \mathscr{S}\bar{t}$, with $\bar{t} = O(1)$. The Stefan condition yields, to leading order,

$$\dot{h} = \frac{k_{sl}}{h} + \frac{1}{1-h} \equiv \psi(h) \quad \text{as} \quad \mathscr{S} \to \infty. \tag{5.5}$$

Note that (5.5) is valid until times such that $t_f - t \gg \delta_{\mathrm{term}}$, with $\delta_{\mathrm{term}} \ll \mathscr{S}$, where δ_{term} denotes the length of the terminal stage of solidification. Though (5.5) has been derived for $t = O(\mathscr{S})$ as $\mathscr{S} \to \infty$, it matches with the solution (5.4*a*) for $t \ll \mathscr{S}$, thus implying consistent initial condition $h(0) = 0$. Hence, the solution of (5.5) is given by the implicit relation

$$\frac{k_{sl}}{(k_{sl}-1)^3}\ln\left|\left(1-\frac{1}{k_{sl}}\right)h-1\right| + \frac{1}{2}\frac{h^2}{k_{sl}-1} + \frac{h}{(k_{sl}-1)^2} = \frac{t}{\mathscr{S}} \tag{5.6}$$

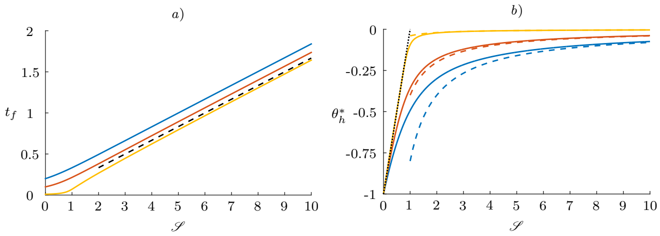

Figure 5.1: *a*) The values of the complete-freezing time, t_f, obtained from the numerical solutions of the full problem, as functions of $\mathscr{S}$, for different values of $\mathcal{G}$: $\mathcal{G} = 5$ (blue), $\mathcal{G} = 10$ (red) and $\mathcal{G} = 100$ (yellow). The black dashed line represents the leading-order value of t_f as $\mathscr{S} \to \infty$, given in (5.8). *b*) The minimum interfacial supercooling, θ_h^*, as a function of Stefan number, $\mathscr{S}$, for the values of $\mathcal{G}$ as in *a*), with the same colours: the solid curves correspond to the numerical results from the full problem and the dashed ones to the asymptotic results for θ_h^* as $\mathscr{S} \to \infty$, given in (5.11). For $\mathscr{S} < 1$ we plot the limiting value of θ_h^* as $\mathcal{G} \to \infty$ (black dotted line), given in (5.16). In all the calculations we have set $k_{sl} = 1$ and $\mathscr{S}_{\min} = 0$.

for $k_{sl} \neq 1$. For $k_{sl} = 1$, the above equation becomes

$$h^2/2 - h^3/3 = t/\mathscr{S}. \tag{5.7}$$

Note that h is continuous at $k_{sl} = 1$. In figure 3.2(a) we compare the numerical solution of (5.6) with the numerical solution of the full problem from section 3. Note a very good agreement of the solutions except at early and terminal stages, where the quasi-steady formulation has $h = O(t^{1/2})$ and the full problem has $h = O(t)$ as $t \to 0$ or t_f.

1

Though (5.6) does not have an explicit solution, it can be used to derive an explicit formula for the time of complete freezing by setting $h(t_f) = 1$. In this way, we obtain

$$t_f = \mathscr{S}\bar{t}_f + O(1) \quad \text{as} \quad \mathscr{S} \to \infty, \tag{5.8}$$

where

$$\bar{t}_f = \begin{cases} \dfrac{k_{sl}^2 - 2k_{sl}\ln k_{sl} - 1}{2(k_{sl}-1)^3}, & \text{for } k_{sl} \neq 1 \\ 1/6, & \text{for } k_{sl} = 1. \end{cases} \tag{5.9}$$

Note that $\bar{t}_f$ decreases monotonically with k_{sl}, and that $\bar{t}_f \to 1/2$ as $k_{sl} \to 0$ and $\bar{t}_f \to 0$ as $k_{sl} \to \infty$. Also note that t_f is independent of $\mathcal{G}$ to leading order in $\mathscr{S}$. In figure 5.1(a) we plot t_f, given in (5.8), together with t_f obtained from the numerical solutions of the full problem, as functions of $\mathscr{S}$, for different values of $\mathcal{G}$. Note that the leading-order value of t_f is accurate even for finite values of $\mathscr{S} > 1$.

As suggested by the numerical solutions in figure 3.2(b), there is a maximum of θ_h, corresponding to the minimum dynamical interfacial supercooling.

From (2.21b) and (5.5) we obtain the interface temperature as a function of the interface position, i.e. $\theta_h = -\psi(h)/\mathcal{G}\mathscr{S}$ to leading order as $\mathscr{S} \to \infty$, with the function ψ defined in (5.5). Hence, θ_h attains maximum at $h = h^*$, where

$$h^* = k_{sl}^{1/2}/(1 + k_{sl}^{1/2}), \tag{5.10}$$

and the value of the maximum is

$$\theta_h^* \sim -(1 + k_{sl}^{1/2})^2/\mathcal{G}\mathscr{S} \quad \text{as} \quad \mathscr{S} \to \infty. \tag{5.11}$$

We denote t^* the time at which $\theta_h(t^*) = \theta_h^*$. Moreover, since $\dot{\theta}_h(t^*) = 0$, the kinetic law (2.21b) implies that $\ddot{h}(t^*) = 0$. Hence the Taylor approximation at $t = t^*$ of the leading-order interface position is

$$h(t) \approx h^* + (1 + k_{sl}^{1/2})^2(t - t^*)/\mathscr{S}, \tag{5.12}$$

with the next term being $O[(t - t^*)/\mathscr{S}]^3$. The Taylor expansion of θ_h at $t = t^*$, obtained by inserting (5.12) into (5.5), is

$$\theta_h(t) \approx -\frac{(1 + k_{sl}^{1/2})^2}{\mathcal{G}\mathscr{S}}\left[1 + \frac{(1 + k_{sl}^{1/2})^6}{3k_{sl}^{1/2}}\left(\frac{t - t^*}{\mathscr{S}}\right)^2\right]. \tag{5.13}$$

Thus we see that for times such that $|t - t^*| \ll \mathscr{S}$ there is a stage of slow solidification with

$$\dot{h} \approx (1 + k_{sl}^{1/2})^2/\mathscr{S} \tag{5.14}$$

and $h \approx h^* = O(1)$, with h^* given in (5.10). During this stage, the interface is close to equilibrium so that $\theta_h \approx \theta_h^*$, with θ_h^* given in (5.11), the interface temperature forming the plateau visible in figure 3.2(b). The values of θ_h^*, obtained numerically, are plotted in figure 5.1(b) for various values of $\mathcal{G}$, together with the asymptotic solution (5.11).

5.2. *Asymptotics for* $\mathscr{S}_{min} < \mathscr{S} < 1$

Though the asymptotic solutions as $\mathscr{S} \to \mathscr{S}_{\min}$ cannot be sought explicitly, as was the case for large $\mathscr{S}$, we obtain useful information from the leading order solution $h \sim \mathcal{G}t$ as $\mathscr{S} \to \mathscr{S}_{\min}$. In particular, we get

$$t_f = 1/\mathcal{G} + O(\mathscr{S} - \mathscr{S}_{\min}) \quad \text{as} \quad \mathscr{S} \to \mathscr{S}_{\min}. \tag{5.15}$$

For $\mathscr{S}_{\min} < \mathscr{S} < 1$, the numerical results shown in figure 5.1(b) suggest that θ_h^* tends to a finite limit as $\mathcal{G} \to \infty$, with $\mathscr{S}$ fixed. This limit is given by the large-time, travelling-wave asymptotics, derived in section 4.3 in a semi-infinite liquid:

$$\theta_h^* \sim -1 + \frac{\mathscr{S} - \mathscr{S}_{\min}}{1 - \mathscr{S}_{\min}} \quad \text{as} \quad \mathcal{G} \to \infty. \tag{5.16}$$

To explain (5.16), we remind the reader of the discussion after (5.2): as $\mathcal{G} \to \infty$, the solution has enough time to converge towards its large-time asymptotics before the finite extent of the liquid becomes important. This is clearly illustrated in figure 3.1(*b*): the temperature profiles, describing the intermediate stage of solidification, obtained as the numerical solutions of the full problem, are in agreement with the travelling-wave asymptotics, given in (4.50*a, b*), with V replaced by $\mathcal{G}V$ due to the thermal scaling. The solidification rate in this stage is $\dot{h} \sim \mathcal{G}V$, with V defined in (4.51), as demonstrated in figure 3.3(*a*).

6. Discussion and concluding remarks

We have addressed the problem of solidification of a kinetically-supercooled liquid on a finite domain with fixed temperature at the boundaries. One consequence of such a configuration is a finite complete-freezing time. Another one is the quasi-steady, hence linear, temperature profile during the early stages of solidification. The persistence of the quasi-steady temperature in the solid at later times was found to be strongly influenced by the strength of the latent-heat release. For large Stefan numbers, the temperature in the solid is quasi-steady all the time until the rapid, terminal stage of solidification. On the other hand, in a hypercooled system in which the Stefan number is less than unity, the temperature in the solid develops a constant profile equal to the interface temperature through the whole solid except to a thermal boundary layer of thickness $(4\kappa_{sl}t)^{1/2}$ at the solid bottom, where t is the dimensionless time scaled on the attachment kinetics timescale.

The novel results of section 4 are related to the incorporation of the solid phase in the two-sided model. In particular, the presence of the solid phase, coupled with the fixed-temperature boundary conditions, allows for the derivation of the solutions at large Stefan numbers, as given in (4.45) and (4.46*a, b*). The analytical progress hinged on decoupling of the equations governing the evolution of h, θ_h and θ_l as the liquid interfacial thermal gradient did not enter the Stefan condition.

The second term on the right-hand side of (4.45) represents the effect of recalescence on the temperature distribution. In thermal scaling, which is a natural scaling from the experimental point of view, the effect of recalescence is of order unity for $t \sim \mathcal{G}^{-2}\mathscr{S}^{-1}$ while it vanishes for $t \gg \mathcal{G}^{-2}\mathscr{S}^{-1}$ as $\mathscr{S} \to \infty$, where t is scaled on the thermal diffusion timescale. At these later times, the leading-order solutions are identical to the classical Neumann solutions that would be obtained for $\mathscr{S} \to \infty$ if the latent-heat release was effectively instantaneous and the linear kinetic law was replaced by a jump condition

$$\theta_h = \begin{cases} -1, & \text{for} \quad t = 0, \\ 0, & \text{for} \quad t > 0. \end{cases} \tag{6.1}$$

An unbounded temperature gradient in the solid at $t \to 0$, implied by (6.1), is consistent with the result of the short-time analysis of section 4.1 that the temperature gradient in the solid at $t = 0$ is equal to $\mathscr{S}/k_{sl}$ as $\mathscr{S} \to \infty$. The

	Water	Copper	Salol
$\dot{h}(0)/\mathrm{m\ s}^{-1}$	4.66×10^{-3}	1.31	3.32×10^{-5}
$\dot{h}(t^*)/\mathrm{m\ s}^{-1}$	7.57×10^{-7}	3.16×10^{-4}	4.78×10^{-7}
h^*/m	6.7×10^{-2}	6.1×10^{-2}	5.8×10^{-2}
$t_{\mathrm{rec}}/\mathrm{s}$	3.86×10^{-4}	2.72×10^{-6}	7.67
t_f/s	8.61×10^{4}	2.09×10^{2}	1.39×10^{5}

Table 2: Values of various dimensional quantities for the material systems listed in table 1: $\dot{h}(0)$ is the initial solidification rate; $\dot{h}(t^*)$ and h^* is the solidification rate and the interface position during the quasi-steady stage; t_{rec} is the typical recalescence time and t_f is the complete-freezing time.

condition (6.1) is also consistent with the small-time behaviour of the quasi-steady interface position given by (5.5). In this view, (5.5) could be interpreted as an intermediate asymptotics for the full problem as it describes the behaviour at times when the precise details of the initial behaviour, given by the inner solutions (4.45) and (4.46*a, b*), cease to affect the evolution of the system (see Barenblatt [19]).

In the quasi-steady regime, when the latent heat dominates the sensible heat, the interface temperature is close to the equilibrium solidification temperature and the solidification rate is constant to leading order. In dimensional terms, (5.11) implies

$$T_m - T_h^* \sim \frac{(k_s^{1/2} + k_l^{1/2})^2 \Delta T}{\rho L_m G H}, \tag{6.2}$$

where T_h^* is the maximum interfacial temperature attained during the course of solidification. The dimensional solidification rate is

$$\dot{h} \approx \dot{h}(t^*) = \frac{(k_s^{1/2} + k_l^{1/2})^2 \Delta T}{\rho L_m H}, \tag{6.3}$$

These results indicate that during the quasi-stationary stage the deviation from the thermodynamic equilibrium and the solidification rate both decrease with the size of the system. This is because the large values of H reduce the diffusive flux of latent heat away from the interface, promoting the temperature rise there. The values of various dimensional quantities for water, copper and salol are presented in table 2. The data show that the typical recalescence time is very short for water and copper, while it is considerably longer for salol, making it a suitable candidate for potential experimental validation of our results.

In the hypercooled case, we have shown that the large-time solutions derived originally in the semi-infinite domain apply also in the finite domain during the intermediate stage of solidification provided $\mathcal{G}$ is large, i.e. when there is a separation of kinetic and thermal scales. The interface temperature during this stage can be approximated by the maximum interface temperature, which in dimensional terms reads

$$T_h \approx T_h^* \equiv T_i + \frac{L_m}{C_{ps}} - \left(\frac{C_{pl}}{C_{ps}} - 1\right)\Delta T, \tag{6.4}$$

as derived from (5.16). It is worth noting that the same value is obtained during equilibration to a steady state in the finite-size thermally-insulated system, a result that is readily derived via energy conservation (see Alexiades & Solomon [20], section 2.4.E).

Acknowledgements

This research was supported by the Slovak Research and Development Agency under the contract No. APVV-18-0308, and by the VEGA grant 1/0347/18.

Appendix A. Derivation of the leading-order temperature profile in the recalescence stage for $t = O(1/\mathscr{S})$ as $\mathscr{S} \to \infty$

In order to solve the leading-order system (4.30) and (4.31a–c), we transform (4.30), using the variable $\eta = t^{1/2}\zeta$, into a simple heat equation of the form

$$\frac{\partial g}{\partial \tau} = \frac{\partial^2 g}{\partial \eta^2}, \tag{A.1}$$

which is subject to

$$\eta = 0: \quad g = 1 + \vartheta_h^0, \tag{A.2a}$$

$$\eta \to \infty: \quad g \to 0, \tag{A.2b}$$

$$t = 0: \quad g = 0, \tag{A.2c}$$

with $g \equiv 1 + \vartheta_0$ and the function ϑ_h^0 is given by (4.33b). The above system can be solved using the Duhamel's theorem (see Carslaw & Jaeger [21], section 2.5), to yield

$$g(\eta,\tau) = \operatorname{erfc}(\eta/2\tau^{1/2}) + \frac{2}{\pi^{1/2}}\int_{\frac{\eta}{2\tau^{1/2}}}^{\infty} \vartheta_h^0\left(\tau - \frac{\eta^2}{4y^2}\right) \mathrm{e}^{-y^2}\,\mathrm{d}y. \tag{A.3}$$

The second term on the right-hand side of the above equation is expressed with the help of the identity

$$\vartheta_h^0\left(\tau - \frac{\eta^2}{4y^2}\right) = \vartheta_h^0(\tau)\left(y^2 - \frac{\zeta^2[\vartheta_h^0(\tau)]^2}{2k_{sl}}\right)^{-1/2} y, \tag{A.4}$$

and then by the application of the substitution from y to u

$$u \equiv \left(y^2 - \frac{\zeta^2[\vartheta_h^0(\tau)]^2}{2k_{sl}}\right)^{1/2}. \tag{A.5}$$

Thus we obtain, using the definition of the function g, the relationship (4.34).

Bibliography

[1] P. V. Hobbs, Ice Physics, Oxford University Press, 2010.

[2] M. Schremb, I. V. Roisman, C. Tropea, Normal impact of supercooled water drops onto a smooth ice surface: experiments and modelling, J. Fluid Mech. 835 (2018) 1087–1107.

[3] M. F. Ashby, D. R. H. Jones, Engineering Materials 2: An Introduction to Microstructures, Processing and Design, Butterworth-Heinemann, 2006.

[4] A. Kostinski, W. Cantrell, Entropic aspects of supercooled droplet freezing, J. Atmos. Sci. 65 (2008) 2961–2971.

[5] S. H. Davis, Theory of Solidification, Cambridge University Press, 2001.

[6] J. D. Evans, J. R. King, Asymptotic results for the Stefan problem with kinetic undercooling, Q. J. Mech. Appl. Math. 53 (2000) 449–473.

[7] T. G. Myers, S. L. Mitchell, F. Font, Energy conservation in the one-phase supercooled Stefan problem, Int. Commun. Heat Mass Transfer 39 (2012) 1522–1525.

[8] F. Feuillebois, A. Lasek, P. Creismeas, F. Pigeonneau, A. Szaniawski, Freezing of a subcooled liquid droplet, J. Colloid Interface Sci. 169 (1995) 90–102.

[9] M. E. Glicksman, R. J. Schaefer, Investigation of solid/liquid interface temperatures via isenthalpic solidification, J. Cryst. Growth 1 (1967) 297–310.

[10] Z. Charach, B. Zaltzman, Planar solidification from an undercooled melt: Asymptotic solutions to a continuum model with interfacial kinetics, Phys. Rev. E 47 (1993) 1230–1234.

[11] M. Tembely, A. Dolatabadi, A comprehensive model for predicting droplet freezing features on a cold substrate, J. Fluid Mech. 859 (2019) 566–585.

[12] N. R. Gewecke, T. P. Schulze, The rapid advance and slow retreat of a mushy zone, J. Fluid Mech. 674 (2011) 227–243.

[13] A. R. Umantsev, Motion of a plane front during crystallization, Sov. Phys. Crystallogr. 30 (1985) 87–91.

[14] F. Font, S. L. Mitchell, T. G. Myers, One-dimensional solidification of supercooled melts, Int. J. Heat Mass Transfer 62 (2013) 411–421.

[15] Z. Charach, A. Zemel, Irreversible thermodynamics of phase change heat transfer: basic principles and applications to latent heat storage, Open Syst. Inf. Dyn. 1 (1992) 423–458.

[16] D. Barahona, Thermodynamic derivation of the activation energy for ice nucleation, Atmos. Chem. Phys. 15 (2015) 13819–13831.

[17] R. F. Boisvert, C. W. Clark, D. W. Lozier, F. W. J. Olver, NIST Handbook of Mathematical Functions, Cambridge University Press, 2010.

[18] P. A. Lagerstrom, R. G. Casten, Basic concepts underlying singular perturbation techniques, SIAM Review 14 (1972) 63–120.

[19] G. I. Barenblatt, Scaling, Self-similarity, and Intermediate Asymptotics, Cambridge University Press, 1996.

[20] A. Alexiades, A. D. Solomon, Mathematical Modeling of Melting and Freezing Processes, Hemisphere Publishing Corporation, 1993.

[21] H. S. Carslaw, J. C. Jaeger, Conduction of Heat in Solids, Oxford University Press, 1959.